

國立交通大學

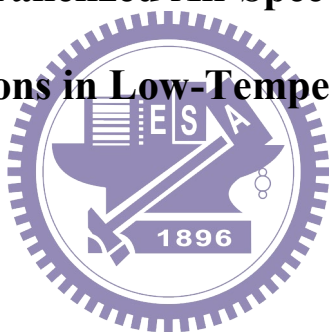
機械工程研究所

博士論文

全速域平行化氣體流動程式之發展及其在低溫電漿之應用

Development of a Parallelized All-Speed Gas Flow Model and Its

Applications in Low-Temperature Plasma



研究生：胡孟樺

指導教授：吳宗信 博士

西元 2012 年 7 月

全速域平行化氣體流動程式之發展及其在低溫電漿之應用

**Development of a Parallelized All-Speed Gas Flow Model and Its**

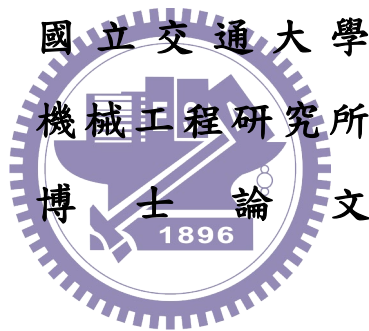
**Application in Low-Temperature Plasma**

研究生：胡孟樺

Student : Meng-Hua Hu

指導教授：吳宗信博士

Advisor : Dr. Jong-Shinn Wu



**A Thesis**

**Submitted to Institute of Mechanical Engineering Collage of**

**National Chiao Tung University**

**In Partial Fulfillment of the Requirements**

**for the Degree of**

**Doctor of Philosophy**

**in**

**Mechanical Engineering**

**July 2012**

**Hsinchu, Taiwan**

西元 2012 年 7 月

# 全速域平行化氣體流動程式之發展

## 及其在低溫電漿之應用

學生：胡孟樺

指導教授：吳宗信

國立交通大學機械工程學系

### 摘要

本論文研究目的主為發展與驗證一個平行化二維/二維軸對稱氣體流動模型程式，應用於全速域可壓縮、黏滯性流體，及具有處理流體與固體間之共軛熱傳遞與適用於稀薄氣體問題之研究。數值方法主要是使用有限體積法(FVM, Finite Volume Method)之結構性同位網格(collocated grid)來離散統御方程式求解。Extended SIMPLE 演算法運用 1972 年 Patankar 與 Spalding 所發展之 SIMPLE (Semi-Implicit Method for Pressure-Linked Equation)演算法為基礎，透過猜測-修正的方法得到壓力場，求解流體之壓力、速度、溫度與氣體組成成份之分布等流體性質。此程式可以廣泛的應用於模擬各種不同的氣壓、不同的氣體流速與不同氣體組成成份之全速域流場。模擬結果並與研究文獻相互驗證比對。

研究主體主要分為三個部份。在論文第一部份，主要為建立並且驗證一個平行化二維/二維軸對稱氣體流動模型程式。程式中所使用的統御方程式包含流體的質量，動量，能量與組成成份之守恆方程式，運用有限體積法之結構性同位網格加以離散求解。模擬結果已與研究文獻結果互相驗證比較。程式平行化方面使用 ASM (Additive Schwarz Method)作為矩陣預處理法(preconditioner)，搭配

GMRES或BiCGS方法解析線性方程式矩陣。程式平行化效率的測試則是使用國立中央大學的V'ger cluster system (Xeon 3GHz dual-core dual-CPU)作為測試平台。針對微尺度超音速流體問題使用800,000個結構性網格操作在64個處理器的狀況下，測試結果顯示平行化效率仍能維持在70%。

論文的第二部份：主要利用所發展之全速域平行化二維/二維軸對稱氣體流動模型程式結合實驗室成員洪捷祭博士[2010]與林昆模博士[2012]所發展之平行化二維/二維軸對稱低溫非熱平衡電漿流體模型程式研究 (1) 混合氫氣與矽烷的電漿輔助化學氣相沈積電漿源在600 mTorr操作氣壓下的流體特性。(2) 常壓微尺度氫氣電漿之流場與熱傳分析，(3) 氫氣介電質放電電漿 (DBD, Dielectric Barrier Discharge) 在頻率25 kHz，760 Torr操作氣壓下之研究。

論文的第三部分，由於電漿相關參數不易量測，故透過氣體流動模型針對氫氣介電質放電電漿在不同電極長度( 5 mm及25 mm)，不同氣體流量(10 ~ 30 slm)，以及改變基材至電漿噴流出口的距離加以模擬，以探討電漿對流場與熱傳特性之影響。

論文最後除了總結研究的成果，並針對未來的研究方向提出建議。

# **Development of a Parallelized All-Speed Gas Flow Model and Its Application in Low-Temperature Plasma**

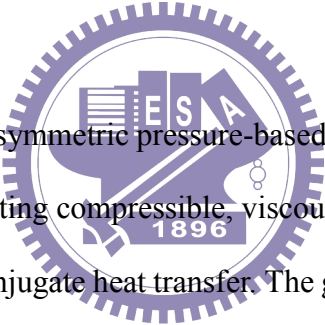
Student : Meng-Hua Hu

Advisor : Dr. Jong-Shinn Wu

Submitted to Department of Mechanical Engineering

National Chiao Tung University

## **Abstract**

The logo of National Chiao Tung University is a circular emblem with a gear-like outer border. Inside the circle, there is a stylized representation of a building or industrial structure, with the letters 'ES' and 'A' prominently displayed. Below the main structure, the year '1896' is inscribed.

A parallelized 2D/2D-axisymmetric pressure-based, finite-volume gas flow model has been developed for simulating compressible, viscous, heat conductive and rarefied gas flows at all speeds with conjugate heat transfer. The governing equations are solved on the structured, collocated grid using a finite volume method. An extended SIMPLE algorithm for compressible flow simulation is proposed which is based on the SIMPLE scheme developed by Patankar and Spalidinf [1972]. The flow properties are solved by a prediction/correction algorithm. Applications with wide range of pressures, flow speeds, and various species concentrations are demonstrated by comparing with previous simulations wherever possible. Research in this thesis is divided into three major phases, which are briefly described in the following in turn.

In the first phase, a parallelized 2D/2D-axisymmetric gas flow model was developed and verified. The discretized equations, including continuity equation, momentum equation, energy equation and species equation are solved by the parallel

ASM (Additive Schwarz Method) and GMRES or BCGS schemes, which are used as the preconditioner and linear matrix equation solver, respectively. The developed code was validated by comparing with previous published simulations wherever available for both low- and high-speed gas flows. Parallel performance for a micro-scale supersonic flow problem (800,000 computational cells) is tested on the V'ger cluster system (Xeon 3GHz dual-core dual-CPU) at National Central University up to 64 processors. Parallel efficiency of the developed gas flow model using 64 processors is about 70%.

In the second phase, (1) A chamber-scale gas discharge of plasma enhanced chemical vapor deposition (PECVD) with silane/hydrogen as the precursors, which was used for depositing hydrogenated amorphous silicon thin film, (2) A helium micro-cell plasma and (3) A two-dimensional helium DBD (Dielectric-barrier discharge) driven by 25 kHz distorted sinusoidal voltages were simulated using the developed gas flow model coupling with parallelized 2D fluid modeling codes developed by Hung [2010] and Lin [2012]. The simulation results show that there are significant differences between the cases with and without considering neutral flow and thermal field.

In the third part, a parametric study was performed to determine the influences of the system configurations, and the flow conditions on the flow and heat transfer characteristics of a helium dielectric-barrier discharge atmospheric-pressure plasma jet.

Recommendations of future research are also outlined at the end of this thesis.

## 致 謝

感謝論文指導教授吳宗信老師的關心與教導，讓我無論是研究或做人處世上都成長許多，思想也更加獨立自主。

感謝國家太空中心陳彥升博士在數值方法的指導，同時也感謝口試委員陳慶耀教授、王啟川教授、呂明璋助理教授、徐振哲副教授和魏大欽副教授在口試時提供的寶貴意見，在此一併致謝。

在交大多年的研究生活，感謝學長洪捷祭、李允民、鄭凱文、李富利、江明鴻、林昆模和學姊周欣芸在研究上的教導及協助，從不吝於幫助我解決難題，使得論文能順利完成，感謝同學邱沅明在求學中的相互鼓勵，以及學妹雅茹，學弟正勤、必任、子豪、宜偉、志東、冠融、垂青、芳安、明忠、世昕、育安、康旻、志華、易軒、哲緯、國淳、駿平，在生活上的幫助。

我親愛的家人，父親胡信坤先生與母親李素珠女士，謝謝你們對我辛苦的栽培，支持著我繼續學習。親愛的姐姐、妹妹、老弟，以及弟媳與妹夫，你們的關懷與包容，也是支持我前進的動力。同時也感謝親愛的楓龍，因為你的呵護與支持，讓我在求學過程無後顧之憂。

再一次獻上我最誠摯的謝意，謝謝你們。

# Table of Contents

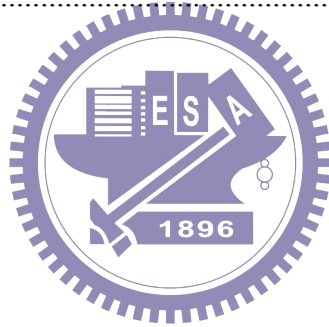
摘要 .....	I
Abstract .....	III
致 謝 .....	V
Table of Contents .....	VI
List of Tables .....	VIII
List of Figures .....	IX
Nomenclature .....	XVI
Chapter 1 Introduction .....	1
1.1 Background and Motivation .....	1
1.2 Literature Survey .....	2
1.2.1. Density-based Schemes .....	2
1.2.2. Pressure-based Schemes .....	3
1.3 Objectives and Organization of this Thesis .....	4
Chapter 2 Numerical Methods .....	6
2.1 Governing Equations .....	6
2.1.1. Continuity Equation .....	6
2.1.2. Momentum Conservation Equation .....	7
2.1.3. Energy Equation .....	8
2.1.4. Species Equation .....	10
2.2. Numerical Schemes .....	12
2.2.1. Nondimensionalization .....	12
2.2.1.3. Continuity Equation .....	12
2.2.1.4. Momentum Equation .....	13
2.2.1.5. Energy Equation .....	14
2.2.1.6. Species Equation .....	14
2.2.2. Spatial Discretization .....	15
2.2.3. Upwind Scheme .....	16
2.2.4. Pressure Smoothing .....	17
2.2.5. Velocity-Slip and Temperature-Jump Boundary Conditions .....	17
2.3. Solution Procedure .....	18
Chapter 3 Verifications and Parallel Performance of the Gas Flow Model .....	21
3.1. Lid-driven Cavity Flow .....	21
3.1.1. Simulation Conditions .....	21
3.1.2. Validation with Previous Simulations .....	22
3.2. Low-Speed Gas Flow with Conjugate Heat Transfer .....	22
3.2.1. Simulation Conditions .....	22
3.2.2. Validation with Previous Simulations .....	23
3.3. Micro-scale High-Speed Gas Flow with Slip Boundary Conditions .....	24
3.3.1. Simulation Conditions .....	24
3.3.2. Validation with Previous Simulations .....	25
3.4. Parallel Performance Study .....	26
3.4.1. Test Conditions .....	26



3.4.2. Results and Discussion .....	26
3.5. Summary .....	26
Chapter 4 Applications in Low-Temperature Plasma Discharge .....	28
4.1. Simulation of Silane/Hydrogen Gas Discharge in a Plasma Enhanced Chemical Vapor Deposition (PECVD) Chamber .....	28
4.1.1. Simulation Conditions .....	28
4.1.2. Results and Discussion .....	29
4.2. Simulation of a Helium Micro-Cell Plasma.....	30
4.2.1. Simulation Conditions .....	30
4.2.2. Results and Discussion .....	31
4.3. Simulation of a Helium Dielectric Barrier Discharge Atmospheric-Pressure Plasma Jet.....	31
4.3.1. Simulation Conditions .....	32
4.3.2. Results and Discussion .....	33
Chapter 5 Parametric Study of a Helium Dielectric Barrier Discharge Atmospheric-Pressure Plasma Jet.....	37
5.1 The Effect of Electrode Length.....	37
5.1.1 Simulation Conditions .....	37
5.1.2 Results and Discussion .....	38
5.2 The Effect of Jet-to-Substrate Spacing Rate.....	38
5.2.1 Simulation Conditions .....	38
5.2.2 Results and Discussion .....	39
5.3 The Effect of Gas Flow Rate.....	40
5.3.1 Simulation Conditions .....	40
5.3.2 Results and Discussion .....	40
5.4 Summary .....	41
Chapter 6 Conclusion and Recommendations for Future Study .....	42
6.1 Summaries of This Thesis.....	42
6.2 Recommendations for Future Work.....	43
References.....	44

## List of Tables

Table 1. Lennard-Jones potential parameters. [Bird et al., 2002] .....	48
Table 2. Constant-pressure specific heats and heat of formation of various ideal gases. [Borgnakke & Sonntag, 2008] .....	48
Table 3. Scaling parameters used in gas flow model. ....	49
Table 4. Substance parameters in helium micro-cell plasma. ....	49
Table 5. Test cases and results of a helium dielectric barrier discharge atmospheric-pressure plasma jet for various $H/d$ for $d = 1$ mm , and gas flow rate of 20slm. ....	50
Table 6. The approximated Reynolds numbers and bulk temperatures for various gas flow rates.....	50



## List of Figures

Figure 2-1: Two-dimensional control volume. ....	51
Figure 2-2: Flowchart of the extended SIMPLE algorithm. ....	52
Figure 3-1: Schematic of the computational grid a in two-dimensional lid-driven cavity. .....	53
Figure 3-2: Streamlines for driven cavity flow with Reynolds numbers of 100, 400 and 1,000 (top to bottom). Note: Ghia et al. [1982] (left); present (right). ....	54
Figure 3-3: Streamlines for driven cavity flow with Reynolds numbers of 3200, 5000, and 10000 (top to bottom). Note: Ghia et al. [1982] (left); present (right)..	55
Figure 3-4: Schematic of the flow in a square cavity with a square block. ....	56
Figure 3-5: Streamlines for Different Locations of Cylinder at $Ri = 0$ . Note: Rahman et al. [2008] (left); present (right). ....	57
Figure 3-6: Isotherms for Different Locations of Cylinder at $Ri = 0$ . Note: Rahman et al. [2008] (left); present (right). ....	58
Figure 3-7: Streamlines for Different Locations of Cylinder at $Ri = 1$ . Note: Rahman et al. [2008] (left); present (right). ....	59
Figure 3-8: Isotherms for Different Locations of Cylinder at $Ri = 1$ . Note: Rahman et al. [2008] (left); present (right). ....	60
Figure 3-9: Streamlines for Different Locations of Cylinder at $Ri = 5$ . Note: Rahman et al. [2008] (left); present (right). ....	61
Figure 3-10: Isotherms for Different Locations of Cylinder at $Ri = 5$ . Note: Rahman et al. [2008] (left); present (right). ....	62
Figure 3-11: Distributions of (a) streamlines and (b) isotherms at $Ri = 5$ , $L_x=0.25$ and $L_y=0.5$ . Note: $\Delta T=50$ K (top), 100 K (middle), and 200 K (bottom). ....	63
Figure 3-12: Distributions of (a) streamlines and (b) isotherms at $Ri = 5$ , $L_x=0.75$ and	

Ly=0.5. Note: $\Delta T=50$ K (top), 100 K (middle), and 200 K (bottom). .....	64
Figure 3-13: Schematic of the two-dimensional micro-scale channel flow .....	65
Figure 3-14: Normalization Distributions of Pressure, Density, Temperature, Velocity in x- and y-direction in the channel at $Ma=2.4261$ and $Kn=0.05$ . .....	66
Figure 3-15: Normalization Distribution of horizontal velocity. Note: Shterev and Stefanov [2010] (upper); present (lower). .....	67
Figure 3-16: Normalization Distribution of temperature. Note: Shterev and Stefanov [2010] (upper); present (lower). .....	67
Figure 3-17: Profiles of the horizontal velocity along the center line of the channel ( $y=H_{ch}/2$ ) for different spatial steps in front of the square. ....	68
Figure 3-18: Profiles of the horizontal velocity along the center line of the channel ( $y=H_{ch}/2$ ) for different spatial steps behind of the square. ....	68
Figure 3-19: Temperature profiles along the center line of the channel ( $y=H_{ch}/2$ ) for different spatial steps in front of the square. ....	69
Figure 3-20: Temperature profiles along the center line of the channel ( $y=H_{ch}/2$ ) for different spatial steps behind of the square. ....	69
Figure 3-21: Parallel Performance and runtime per time step of a 2D micro-scale supersonic flow with $2000 \times 400$ computational cells. ....	70
Figure 4-1: Simulated cycle average of electron number density (a) with and (b) without heating flow field. ....	71
Figure 4-2: Simulated cycle averaged distributions of electron temperature (a) with and (b) without heating flow field. ....	72
Figure 4-3: Simulated cycle averaged distributions of $N_4^+$ (a) with and (b) without considering neutral flow field. ....	73
Figure 4-4: Simulated cycle averaged distributions of electron $He_{meta}$ (a) with and (b)	

without heating flow field.....	74
Figure 4-5: Sketch of a H <sub>2</sub> /SiF <sub>4</sub> PECVD chamber.....	75
Figure 4-6: Schematic of the computational grid in the H <sub>2</sub> /SiF <sub>4</sub> PECVD chamber.....	76
Figure 4-7: Distribution of (a) pressure, (b) density (c) and gas temperature in a PECVD chamber.....	77
Figure 4-8: Distribution of (a) total enthalpy, (b) density of H <sub>2</sub> and (c) SiH <sub>4</sub> in a PECVD chamber.....	78
Figure 4-9: Distribution of (a) velocity in x-direction, (b) Velocity in y-direction, (c) Mean velocity and (d) streamline in a PECVD chamber.....	79
Figure 4-10: Sketch of helium micro-cell plasma.....	80
Figure 4-11: Distribution of plasma u-momentum source in the He micro-cell plasma.....	81
Figure 4-12: Distribution of plasma v-momentum source in the He micro-cell plasma.....	81
Figure 4-13: Distribution of plasma energy source in the He micro-cell plasma.....	82
Figure 4-14: Temperature distribution of a He micro-cell plasma without considering plasma momentum source.....	82
Figure 4-15: Mean speed distribution of a He micro-cell plasma without considering plasma momentum source.....	83
Figure 4-16: Mean speed distribution of a He micro-cell plasma with considering plasma momentum source.....	83
Figure 4-17: Force field distribution of a He micro-cell plasma.....	84
Figure 4-18: Temperature distribution of a He micro-cell plasma with considering plasma momentum source.....	84
Figure 4-19: Schematic sketch of a planar dielectric barrier discharge	

atmospheric-pressure plasma jet.....	85
Figure 4-20. Sketch of two-dimensional dielectric barrier discharge	
atmospheric-pressure plasma jet.....	86
Figure 4-21. Schematic of the computational grid in the two-dimensional dielectric	
barrier discharge atmospheric-pressure plasma jet.....	87
Figure 4-22. Time history of velocity and temperature profiles at the export of helium	
DBD APPJ for $d = 1 \text{ mm}$ , $H/d = 10$ , $Re = 60$ and gas flow rate of	
20 slm .....	88
Figure 4-23: Steady-steady distribution of (a) pressure and (b) density of helium DBD	
APPJ for $d = 1 \text{ mm}$ , $H/d = 10$ , $Re = 60$ and gas flow rate of 20 slm ...	89
Figure 4-24: Spatial distribution of temperature with (a) a adiabatic substrate surface; (b)	
an isothermal substrate surface of a helium DBD APPJ for $d = 1 \text{ mm}$ ,	
$H/d = 10$ , $Re = 60$ and gas flow rate of 20 slm .....	90
Figure 4-25: Spatial distribution of velocity (a) in x-direction and (b) in y-direction of	
helium DBD APPJ for $d = 1 \text{ mm}$ , $H/d = 10$ , $Re = 60$ and gas flow rate of	
20 slm .....	91
Figure 4-26: Steady-steady distributions of (a) mean speed, (b) streamlines and velocity	
vector of helium DBD APPJ for $d = 1 \text{ mm}$ , $H/d = 10$ , $Re = 60$ and gas	
flow rate of 20 slm .....	92
Figure 4-27: streamlines and velocity vector patterns of helium DBD APPJ for	
$d = 1 \text{ mm}$ , $H/d = 10$ , $Re = 60$ and gas flow rate of 20 slm .....	93
Figure 4-28: Time history of streamlines and velocity vector patterns of helium DBD	
APPJ for $d = 1 \text{ mm}$ , $H/d = 10$ , $Re = 60$ and gas flow rate of 20 slm ...	94
Figure 4-29. Horizontal velocity profiles in the helium DBD APPJ channel at different	

x positions for $d = 1$ mm, $H/d = 10$ , $Re = 60$ and gas flow rate of 20 slm .	95
Figure 4-30. Temperature profiles in the helium DBD APPJ channel at different x positions for $d = 1$ mm, $H/d = 10$ , $Re = 60$ and gas flow rate of 20 slm .	96
Figure 4-31. Horizontal velocity and temperature profiles along the center line of the helium DBD APPJ channel for $d = 1$ mm, $H/d = 10$ , $Re = 60$ and gas flow rate of 20 slm .	97
Figure 4-32. Vertical velocity profiles between helium DBD APPJ and substrate at different y positions for $d = 1$ mm, $H/d = 10$ , $Re = 60$ and gas flow rate of 20 slm .	98
Figure 4-33. Temperature profiles between helium DBD APPJ and substrate at different y positions for $d = 1$ mm, $H/d = 10$ , $Re = 60$ and gas flow rate of 20 slm .	99
Figure 4-34. Local Nusselt number along a isothermal substrate surface for $d = 1$ mm, $H/d = 10$ , $Re = 60$ and gas flow rate of 20 slm .	100
Figure 5-1. Comparison of the distributions of (a, e) pressure, (b, f) over-all density, (c, g) temperature for an adiabatic wall, and (d, h) temperature for an adiabatic wall for electrode lengths of 5 mm and 25 mm, respectively. ....	101
Figure 5-2. Comparison of the distributions of velocity components for electrode lengths of (a-d) 5 mm and of (e-h) 25 mm , respectively. ....	102
Figure 5-3. Comparison of the distributions of species mole fraction for electrode lengths of (a-d) 5 mm and of (e-h) 25 mm , respectively. ....	103
Figure 5-4. Comparison of the temperature distributions for an adiabatic substrate for	

$H/d =$ (a) 5, (b) 7.5, (c) 10, (d) 12.5, (e) and 15, respectively. ....	104
Figure 5-5. Comparison of the temperature distributions of an isothermal substrate for $H/d =$ (a) 5, (b) 7.5, (c) 10, (d) 12.5, (e) and 15, respectively. ....	105
Figure 5-6. Comparison of the mean speed distributions for $H/d =$ (a) 5, (b) 7.5, (c) 10, (d) 12.5, (e) and 15, respectively.....	106
Figure 5-7. Comparison of the streamline profiles for $H/d =$ (a) 5, (b) 7.5, (c) 10, (d) 12.5, (e) and 15, respectively. ....	107
Figure 5-8. Comparison of the distributions of $X_{He}$ for various $H/d =$ (a) 5, (b) 7.5, (c) 10, (d) 12.5, (e) and 15, respectively.....	108
Figure 5-9. Comparison of the distributions of $X_{N_2}$ for various $H/d =$ (a) 5, (b) 7.5, (c) 10, (d) 12.5, (e) and 15, respectively.....	109
Figure 5-10. Comparison of the distributions of $X_{O_2}$ for various $H/d =$ (a) 5, (b) 7.5, (c) 10, (d) 12.5, (e) and 15, respectively. ....	110
Figure 5-11. Local Nusselt number along a isothermal substrate surface for various $H/d$ .....	111
Figure 5-12. Comparison of the temperature distributions for an adiabatic substrate for various gas flow rates of (a) 10 <i>slm</i> , (b) 15 <i>slm</i> , (c) 20 <i>slm</i> , (d) 25 <i>slm</i> , (e) and 30 <i>slm</i> , respectively. ....	112
Figure 5-13. Comparison of the temperature distributions for an isothermal wall for various gas flow rates of (a) 10 <i>slm</i> , (b) 15 <i>slm</i> , (c) 20 <i>slm</i> , (d) 25 <i>slm</i> , (e) and 30 <i>slm</i> , respectively. ....	113
Figure 5-14. Comparison of the mean speed distributions for gas flow rates of (a) 10 <i>slm</i> , (b) 15 <i>slm</i> , (c) 20 <i>slm</i> , (d) 25 <i>slm</i> , (e) and 30 <i>slm</i> , respectively. .....	114

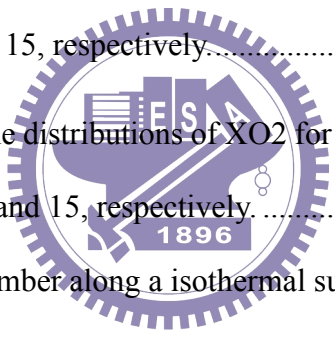




Figure 5-15. Comparison of the streamline profiles for various gas flow rates of (a) 10 *slm*, (b) 15 *slm*, (c) 20 *slm*, (d) 25 *slm*, (e) and 30 *slm*, respectively. .... 115

Figure 5-16. Comparison of the distributions of  $X_{He}$  for various gas flow rates of (a) 10 *slm*, (b) 15 *slm*, (c) 20 *slm*, (d) 25 *slm*, (e) and 30 *slm*, respectively. .... 116

Figure 5-17. Comparison of the distributions of  $X_{N_2}$  for various gas flow rates of (a) 10 *slm*, (b) 15 *slm*, (c) 20 *slm*, (d) 25 *slm*, (e) and 30 *slm*, respectively. .... 117

Figure 5-18. Comparison of the distributions of  $X_{O_2}$  for various gas flow rates of (a) 10 *slm*, (b) 15 *slm*, (c) 20 *slm*, (d) 25 *slm*, (e) and 30 *slm*, respectively. .... 118

Figure 5-19. Horizontal velocity profiles at export of helium DBD APPJ as a function of times for various gas flow rates. .... 119

Figure 5-20. Temperature profiles at export of helium DBD APPJ as a function of times for various gas flow rates. .... 120

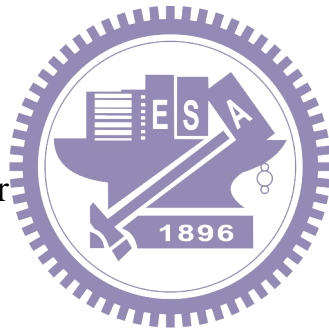
Figure 5-21. Horizontal velocity profiles along the center line of the helium DBD APPJ for various gas flow rates. .... 121

Figure 5-22. Temperature profiles along the center line of the helium DBD APPJ for various gas flow rates. .... 122

Figure 5-23. Local Nusselt number profiles along the substrate surface for various gas flow rates. .... 123

## Nomenclature

$a$	Combined convection and diffusion coefficient
$A$	Control volume interface area
$b$	Partial source term
$C_p$	Constant-pressure specific heat,
$C_v$	Constant-volume specific heat
$d$	Velocity-correction coefficient of SIMPLE
$dt$	Time step size
$Ma$	Mach number
$p$	Pressure
$Pr$	Prandtl number
$R$	Gas constant
$Re$	Reynolds number
$S$	Full source term
$t$	Time
$T$	Temperature
$u$	X-direction velocity
$v$	Y-direction velocity
$\phi$	General dependent variable
$\Gamma$	General exchange coefficient
$\mu$	Viscosity
$\rho$	Density
$\square$	Summation



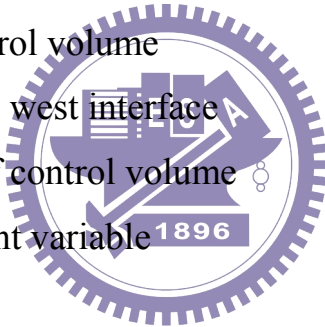
### Superscripts

$n$	Time step number
-----	------------------

- \* Latest current estimate of field variable
- ' Correction value to \*

### **Subscripts**

- $e$  Control volume's east interface
- $E$  Main cell east of control volume
- $j$  Summation index
- $n$  Control volume's north interface
- $nb$  Neighboring main cell
- $N$  Main cell north of control volume
- $s$  Control volume's south interface
- $S$  Main cell south of control volume
- $P$  Main cell of control volume
- $w$  Control volume's west interface
- $W$  Main cell west of control volume
- $\phi$  General dependent variable



# Chapter 1

## Introduction

### 1.1 Background and Motivation

In order to investigate the flow physics under realistic conditions, a numerical method for compressible, viscous flows with conjugate heat transfer for all-speed regimes is necessary. There are many numerical methods that used density as one of the primary variables and extract the static pressure from the equation of state. Such methods failed in incompressible or low Mach number compressible flows without special treatment, since in low compressibility limit, the density changes are very small and the pressure-density coupling becomes very weak. Other methods, such as pressure correction methods, use pressure as the primary variable for solving the continuity equation, are mostly suitable for incompressible flow.

In addition, heat transfer problems involving buoyancy effect were usually simulated treating the fluid as an incompressible flow by employing Boussinesq approximation, which assumes small density difference between hot fluid (or surface) and cold surface (or fluid). However, this assumption is obviously invalid as the temperature difference becomes large, or equivalently when the buoyancy effect is strong, especially if gases, rather than liquids, are involved. Nevertheless, most of the studies published in the literature in the past still applied this assumption even with very large buoyancy effect present in the flow. That can induce large errors in predicted heat transfer by adhering to this assumption without considering the compressibility effect of the gas.

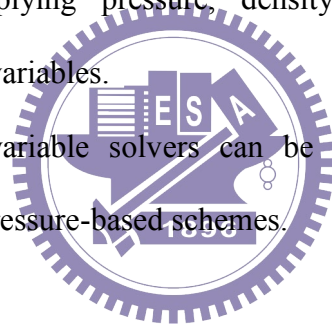
This study represents a parallel compressible pressure-based, cell-centered finite

volume method applicable for all-speed of flows, in which the primary variables are the Cartesian velocity components, pressure, total enthalpy, and mole fraction of the species.

## 1.2 Literature Survey

Numerical methods, which are applicable to flows for all-speed regimes are of special interest in the present research. Gosman et al. [1969] calculated vorticity and stream function to substitute for pressure form governing equation. However, this method is difficult in specifying the vorticity boundary conditions at the wall. Harlow et al. [1965] presented semi-implicit Marker-and-Cell method (MAC) and Simplified MAC (SMAC) [1970] applying pressure, density, velocity components, and temperature as the primitive variables.

In General, primitive variable solvers can be classified into two schemes: density-based schemes and pressure-based schemes.



### 1.2.1. Density-based Schemes

The original mass conservation equation is utilized in the density-based scheme. Briley and McDonald [1980], Jameson et al. [1981], and Sahu et al. [1985] treat density as a main dependent variable, and the pressure is calculated by the equation of state. However, this method is limited in low-speed flow due to weakly linkage between pressure and density.

Chorin [1967] developed the artificial compressibility method for the incompressible Euler equations. A scaled pressure time derivative in the continuity equation is presented. Turkel [1987] extended Chorin's method to compressible governing equation. A preconditioning scheme is devised for the Euler equations for

all Mach number.

An improved preconditioning method derived by Merkel and Choi [1988] can solve problems with Mach number as small as  $10^{-6}$ . Hosangadi et al. [1990] presented a time-accurate density-based method, which used the second-order three-point backwards method for the physical-time derivative and the first-order implicit Euler method for the pseudo-time derivative. Choi and Merkel [1991, 1993] derived a preconditioning method for inviscid and viscous steady flows at all speeds. Shuen et al. [1992, 1993] extended this preconditioning method to include non-equilibrium chemistry and applied a dual time-stepping technique to obtain time-accurate solutions.

### 1.2.2. Pressure-based Schemes

The pressure-based schemes, or the pressure-velocity coupling schemes specify pressure as a primary dependent variable, which are valid for incompressible/compressible flow.

Chorin [1968] developed the pressure-correction method for the incompressible Navier-Stokes equations. The velocity correction is based on pressure gradients alone. Parankar and Spalding [1972] developed the SIMPLE (Semi-Implicit Method for Pressure-Linked Equations) method. The velocity correction equation came from the full governing equation. In 1971, Harlow and Amsden extend the pressure-correction method to an all-speed compressible pressure-based scheme. Density was calculated by the equation of state. A staggered grid is utilized in this method. Issa et al. [1986] developed the PISO (Pressure-Implicit with Splitting of Operators) method. The applied an implicit flux-splitting semi-iterative discretization to solve time-ecoling compressible and incompressible flows. In 1989, Karki and Patankar developed a

fully iterative discretization SIMPLEC method. Rhie [1989] extended this approach to general fluid flow. The pressure in this scheme depended on the internal energy. Multigrid techniques were utilized to accelerated the iteration procedure. Shyy and Chen [1992] also employed the multigrid techniques. They used the second-order upwind method for the convective terms and the first-order upwind method for the density gradients at high Mach numbers. Karki and Patankar [1989] and Demirdzic et al [1993] presented an extended SIMPLE method. A collocated grid and second-order central-difference/first-order upwind scheme were utilized for the numerical simulations.

Issa and Javareshkian [1998] implemented total variation diminishing (TVD) upwind schemes into all-speed pressure-based method. They utilized the PISO scheme for the time-dependent problems and SIMPLE scheme for the steady-state problems.

Rossow [2003] presented a blended pressure/density-based method with a collocated grid. The pressure and density time-derivatives were added to the pressure equation for high Mach numbers. Hou and Mahesh [2005] presented a scheme for all-speed compressible flows.

### **1.3 Objectives and Organization of this Thesis**

The specific objectives of this study are

1. To develop a parallelized 2D/2D axisymmetric gas flow model for all-speed gas flow using finite volume method.
2. To validate the developed gas flow model under low- and high-speed gas flow by comparing with previous simulations wherever possible;
3. To investigate the flow and thermal characteristics in a silane/hydrogen

discharge inside a typical PECVD chamber by coupling with plasma fluid modeling.

4. To simulate the flow and heat transfer characteristics in helium dielectric barrier discharge atmospheric-pressure jet

The thesis is organized as follows:

Chapter 2 describes the governing equations including the continuity, momentum, energy equation and species equations, and the numerical methods developed by using the finite volume method.

Chapter 3 presents the validation of the developed gas flow model by several benchmark problems. The parallel performance is tested by applying GMRES or BiCGS as the KSP solver and ILU as the sub-domain solver on the V'ger cluster system (Xeon 3GHz dual-core dual-CPU) at National Central University.

Chapter 4 presents several applications of gas flow model in low-temperature plasma by couple with plasma fluid modeling.

Chapter 5 discusses some parameters influence on helium dielectric barrier discharge atmospheric-pressure plasma jet.

Chapter 6 is the summary of this thesis and some recommendations for the future work.



# Chapter 2

## Numerical Methods

### 2.1 Governing Equations

The governing equations for mass, momentum, energy and species conservation equations in two-dimensional Cartesian coordinates can be written in a differential equation of general form:

$$\frac{\partial(\rho\phi)}{\partial t} + \frac{\partial}{\partial x_j}(\rho V_j \phi) = \frac{\partial}{\partial x_j} \left( \Gamma_\phi \frac{\partial \phi}{\partial x_j} \right) + S_\phi \quad (2-1)$$

where  $\rho$  is the fluid density and  $\phi = (1, u, v, h_t, Y_\alpha)$  is the dependent variable for the mass, momentum, total enthalpy and mass fraction of  $\alpha_{th}$  species, respectively.  $t$  is the time,  $x$  is the coordinate,  $V$  is the velocity, and the subscript  $j$  can take the value 1 and 2, denoting the two space coordinates. The effective diffusion coefficient  $\Gamma_\phi$  and the source term  $S_\phi$  will be described below. The total Enthalpy  $h_t$  is a function of the static enthalpy  $h_s$  and the flow kinetic energy.

#### 2.1.1. Continuity Equation

The continuity equation is based on the law of conservation of mass, which can be written in a differential form

$$\frac{\partial \rho}{\partial t} + \frac{\partial(\rho u)}{\partial x} + \frac{\partial(\rho v)}{\partial y} = 0 \quad (2-2)$$

For any control volume, the conservation of mass means that the net mass flow out of the control volume must be equal to the time rate of decrease of mass inside the control

volume.

### 2.1.2. Momentum Conservation Equation

The momentum equation in the direction of x-axis is as follows:

$$\frac{\partial(\rho u)}{\partial t} + \frac{\partial(\rho uu)}{\partial x} + \frac{\partial(\rho vu)}{\partial y} = -\frac{\partial P}{\partial x} + \frac{\partial \tau_{xx}}{\partial x} + \frac{\partial \tau_{yx}}{\partial y} + \rho g_x \quad (2-3)$$

where  $g_x$  is the gravitational acceleration in x-direction, and  $P$  is the pressure, respectively. The relationship between the pressure, density and temperature of a fluid is linked through an equation of state. The ideal gas law, an example of an equation of state, is applied in this study

$$P = \rho RT \quad (2-4)$$

where  $R$  is the gas constant.

Stokes in 1845 obtained the stress acting on the surface for Newtonian fluids

$$\tau_{xx} = \lambda(\nabla \cdot \mathbf{V}) + 2\mu \frac{\partial u}{\partial x} \quad (2-5.a)$$

$$\tau_{yy} = \lambda(\nabla \cdot \mathbf{V}) + 2\mu \frac{\partial v}{\partial y} \quad (2-5.b)$$

$$\tau_{xy} = \tau_{yx} = \mu \left[ \frac{\partial v}{\partial x} + \frac{\partial u}{\partial y} \right] \quad (2-5.c)$$

where  $\mu$  is the molecular viscosity coefficient. The viscosity of a pure monatomic gas can be written in terms of the Lennard-Jones parameters as

$$\mu = \frac{5}{16} \frac{\sqrt{\pi m k_B T}}{\pi \sigma^2 \Omega_\mu} = 2.6693 \times 10^{-6} \frac{\sqrt{MT}}{\sigma^2 \Omega_\mu} \quad (2-6)$$

in which  $m$  is mass,  $k_B$  is the Boltzmann constant,  $T$  is the absolute temperature, and  $M$  is molecular weight [Bird et al., 2002]. The characteristic diameter of the molecular  $\sigma$  used in this study is given in Table 1. The collision integral for viscosity  $\Omega_\mu$  is curve-fitted as follows [Neufeld et al., 1972]:

$$\Omega_\mu = \frac{1.16145}{T^{*0.14874}} + \frac{0.52487}{\exp(0.77320T^*)} + \frac{2.16178}{\exp(2.43787T^*)} \quad (2-7)$$

where  $T^* = k_B T / \varepsilon$  is a dimensionless temperature, and  $\varepsilon$  is the characteristic energy listed in Table 1.

$\nabla = \left( \frac{\partial}{\partial x} \mathbf{i} + \frac{\partial}{\partial y} \mathbf{j} \right)$  is the differential-operator, where  $\mathbf{i} = (1, 0)$  and  $\mathbf{j} = (0, 1)$  are unit vectors in the direction of the x-axis and y-axis respectively.  $\lambda$ , the second viscosity coefficient, is frequently assumed to be equal to  $-\frac{2}{3}\mu$ .

By organizing Eq.(2) to a general form, the momentum equation in the direction of the x-axis is adapted as

$$\frac{\partial(\rho u)}{\partial t} + \frac{\partial(\rho u u)}{\partial x} + \frac{\partial(\rho v u)}{\partial y} = \frac{\partial}{\partial x} \left( \mu \frac{\partial u}{\partial x} \right) + \frac{\partial}{\partial y} \left( \mu \frac{\partial u}{\partial y} \right) + S_u \quad (2-8)$$

where the source term  $S_u$  is expressed as

$$S_u = -\frac{\partial p}{\partial x} + \frac{\partial}{\partial x} \left[ \frac{1}{3} \mu \left( \frac{\partial u}{\partial x} - 2 \frac{\partial v}{\partial y} \right) \right] + \frac{\partial}{\partial y} \left( \mu \frac{\partial v}{\partial x} \right) + \rho g_x \quad (2-9)$$

The momentum equation in the direction of y-axis has the same form as that in x-direction.

### 2.1.3. Energy Equation

The energy equation is as follows:

$$\begin{aligned} & \frac{\partial}{\partial t} \left[ \rho \left( e + \frac{V^2}{2} \right) \right] + \frac{\partial}{\partial x} \left[ \rho u \left( e + \frac{V^2}{2} \right) \right] + \frac{\partial}{\partial y} \left[ \rho v \left( e + \frac{V^2}{2} \right) \right] \\ & = \frac{\partial}{\partial x} \left( k \frac{\partial T}{\partial x} \right) + \frac{\partial}{\partial y} \left( k \frac{\partial T}{\partial y} \right) - \frac{\partial}{\partial x} (u p) \\ & \quad - \frac{\partial}{\partial y} (v p) + \frac{\partial}{\partial x} (u \tau_{xx} + v \tau_{xy}) + \frac{\partial}{\partial y} (u \tau_{yx} + v \tau_{yy}) \\ & \quad + \rho u g_x + \rho v g_y \end{aligned} \quad (2-10)$$

in which  $e$  is the internal energy due to random molecular motion,  $\frac{V^2}{2}$  is the kinetic energy, and  $k$  is the thermal conductivity. The thermal conductivity of a monatomic gas is

$$k = \frac{25}{32} \frac{\sqrt{\pi m k_B T}}{\pi \sigma^2 \Omega_k} C_v = 8.3144 \times 10^{-2} \frac{\sqrt{MT}}{\sigma^2 \Omega_k} \quad (2-11)$$

where  $C_v$  is the heat capacity at constant volume, and the collision integral for thermal conductivity,  $\Omega_k$ , is identical to that for viscosity,  $\Omega_\mu$ .

The total enthalpy  $h_t$  is the sum of the static enthalpy  $h_s$  and the kinetic energy,

$$h_t = h_s + \frac{V^2}{2} \quad (2-12)$$

in which the static enthalpy is

$$h_s = \Delta h_f^0 + \int_{T^0}^T C_p(T) dT \quad (2-13)$$

Here  $\Delta h_f^0$  is the standard enthalpy of formation at the standard state (298.15 K and 1 atmosphere), and  $C_p(T)$  is the specific heat capacity at constant pressure listed in Table 2.

In this study, the energy equation is rewritten in terms of the total enthalpy as follows:

$$\frac{\partial}{\partial t}(\rho h_t) + \frac{\partial}{\partial x}(\rho u h_t) + \frac{\partial}{\partial y}(\rho v h_t) = \frac{\partial}{\partial x} \left( k \frac{\partial T}{\partial x} \right) + \frac{\partial}{\partial y} \left( k \frac{\partial T}{\partial y} \right) + S_{h_t} \quad (2-14)$$

For the  $k \frac{\partial T}{\partial x}$  terms in the energy equation, since  $C_p(T) = \frac{dh_s}{dT}$  is still true even if polynomials are used to describe  $h_s$ . Therefore, the following derivation can still be applied.

$$\begin{aligned}
& \frac{\partial}{\partial x} \left( k \frac{\partial T}{\partial x} \right) \\
&= \frac{\partial}{\partial x} \left( \frac{k}{C_p} \frac{\partial h_s}{\partial x} \right) \\
&= \frac{\partial}{\partial x} \left[ \frac{k}{C_p} \frac{\partial}{\partial x} \left( h_s + \frac{V^2}{2} \right) \right] - \frac{\partial}{\partial x} \left[ \frac{k}{C_p} \frac{\partial}{\partial x} \left( \frac{V^2}{2} \right) \right] \\
&= \frac{\partial}{\partial x} \left[ \frac{k}{C_p} \frac{\partial h_t}{\partial x} \right] - \frac{\partial}{\partial x} \left[ \frac{k}{C_p} \frac{\partial}{\partial x} \left( \frac{V^2}{2} \right) \right]
\end{aligned} \tag{2-15}$$

Hence, the Eq.(2) can be written as

$$\frac{\partial}{\partial t} (\rho h_t) + \frac{\partial}{\partial x} (\rho u h_t) + \frac{\partial}{\partial y} (\rho v h_t) = \frac{\partial}{\partial x} \left( \frac{k}{C_p} \frac{\partial h_t}{\partial x} \right) + \frac{\partial}{\partial y} \left( \frac{k}{C_p} \frac{\partial h_t}{\partial y} \right) + S_{h_t} \tag{2-16}$$

and the energy source term  $S_{h_t}$  is expressed as

$$\begin{aligned}
S_{h_t} &= - \frac{\partial}{\partial x} \left[ \frac{k}{C_p} \frac{\partial}{\partial x} \left( \frac{V^2}{2} \right) \right] - \frac{\partial}{\partial y} \left[ \frac{k}{C_p} \frac{\partial}{\partial y} \left( \frac{V^2}{2} \right) \right] \\
&\quad + \frac{\partial}{\partial x} (u \tau_{xx} + v \tau_{xy}) + \frac{\partial}{\partial y} (u \tau_{yx} + v \tau_{yy}) + \rho u g_x + \rho v g_y + \frac{\partial p}{\partial t}
\end{aligned} \tag{2-17}$$

#### 2.1.4. Species Equation

The conservation of mass species equation is

$$\frac{\partial (\rho Y_\alpha)}{\partial t} + \frac{\partial (\rho u Y_\alpha)}{\partial x} + \frac{\partial (\rho v Y_\alpha)}{\partial y} = \frac{\partial}{\partial x} \left( \rho D_{\alpha,eff} \frac{\partial Y_\alpha}{\partial x} \right) + \frac{\partial}{\partial y} \left( \rho D_{\alpha,eff} \frac{\partial Y_\alpha}{\partial y} \right) + R_\alpha \tag{2-18}$$

Where the mass fraction of  $\alpha_{th}$  species ( $Y_\alpha$ ) is defined as the ratio of the mass of the  $\alpha_{th}$  species to the total mass of the mixture [Patankar, 1980].  $R_\alpha$ , the rate of formation of  $Y_\alpha$  through chemical reactions, is neglected in this modeling. The effective diffusion coefficient of  $\alpha_{th}$  species in multicomponent gas mixtures [Fairbanks and Wilke, 1950] is estimated

$$D_{\alpha,eff} = \frac{1 - X_{\alpha}}{\frac{X_{\beta}}{D_{\alpha\beta}} + \frac{X_{\gamma}}{D_{\alpha\gamma}} + \dots} \quad (2-19)$$

where  $X_{\alpha} = Y_{\alpha} \frac{M_{mix}}{M_{\alpha}}$  is the mole fraction of  $\alpha_{th}$  species.  $D_{\alpha\beta}$ ,  $D_{\alpha\gamma}$ , etc., are the respective binary diffusion coefficients, which is defined by

$$D_{\alpha\beta} = \frac{1.86 \times 10^{-7} \times T^{3/2} \sqrt{\frac{1}{M_{\alpha}} + \frac{1}{M_{\beta}}}}{P \sigma_{\alpha\beta}^2 \Omega_{D,\alpha\beta}} \quad (2-20)$$

Here  $\sigma_{\alpha\beta} = \frac{1}{2}(\sigma_{\alpha} + \sigma_{\beta})$  is the average collision diameter,  $\Omega_{D,\alpha\beta}$  is a temperature-dependent collision integral

$$\Omega_{D,\alpha\beta} = \frac{1.06306}{T^{*0.15610}} + \frac{0.19300}{\exp(0.47635T^*)} + \frac{1.03587}{\exp(1.52996T^*)} + \frac{1.76474}{\exp(3.89411T^*)} \quad (2-21)$$

For multicomponent gas, the viscosity is estimated by the following formula:

$$\mu_{mix} = \frac{\sum_{\alpha=1}^N X_{\alpha} \mu_{\alpha}}{\sum_{\beta} X_{\beta} \Phi_{\alpha\beta}} \quad (2-22)$$

Here the dimensionless quantity  $\Phi_{\alpha\beta}$  is

$$\Phi_{\alpha\beta} = \frac{1}{\sqrt{8}} \left( 1 + \frac{M_{\alpha}}{M_{\beta}} \right)^{-1/2} \left[ 1 + \left( \frac{\mu_{\alpha}}{\mu_{\beta}} \right)^{1/2} \left( \frac{M_{\beta}}{M_{\alpha}} \right)^{1/4} \right]^2 \quad (2-23)$$

,  $N$  is the number of species in the mixture,  $x_{\alpha}$  is the mole fraction of species  $\alpha$ ,  $\mu_{\alpha}$  is the viscosity of pure species  $\alpha$ , and  $M_{\alpha}$  is the molecular weight of species  $\alpha$ .

The thermal conductivity of gas mixture is analogous to the viscosity, which is estimated by

$$k_{mix} = \frac{\sum_{\alpha=1}^N X_{\alpha} k_{\alpha}}{\sum_{\beta} X_{\beta} \Phi_{\alpha\beta}} \quad (2-24)$$

The  $k_\alpha$  is the thermal conductivity of pure species, and  $\Phi_{\alpha\beta}$  is identical to that using in the viscosity equation.

## 2.2. Numerical Schemes

### 2.2.1. Nondimensionalization

Before solving the above equations, a dimensionless process is applied to simplify and parameterize problems where measured units are involved. The scaling parameters, utilized in nondimensionalizing the governing equations, are listed in Table 3. The relevant nondimensional quantities denoted by a symbol (\*) are defined as follows:

$$\begin{aligned}
 x^* &= \frac{x}{L_\infty} ; y^* = \frac{y}{L_\infty} ; u^* = \frac{u}{U_\infty} ; v^* = \frac{v}{U_\infty} ; t^* = \frac{tU_\infty}{L_\infty} ; \rho^* = \frac{\rho}{\rho_\infty} ; \\
 p^* &= \frac{p}{\rho_\infty U_\infty^2} ; T^* = \frac{T}{T_\infty} ; \mu^* = \frac{\mu}{\mu_\infty} ; k^* = \frac{k}{k_\infty} ; \tau_{i,j}^* = \frac{\tau_{i,j}}{\rho_\infty U_\infty^2} ; \\
 D^* &= \frac{D}{D_\infty} ; R^* = \frac{R}{R_\infty} ; C_p^* = \frac{C_p}{C_{p,\infty}} ; h^* = \frac{h}{h_\infty} = \frac{h_s + \frac{V^2}{2}}{U_\infty^2} ;
 \end{aligned} \tag{2-25}$$

Then, the transport equations given above are nondimensionalized using the above dimensionless quantities.

#### 2.2.1.3. Continuity Equation

Substitute the above dimensionless variables into the continuity equation

$$\frac{\rho_\infty U_\infty}{L_\infty} \frac{\partial \rho^*}{\partial t^*} + \frac{\rho_\infty U_\infty}{L_\infty} \frac{\partial (\rho^* u^*)}{\partial x^*} + \frac{\rho_\infty U_\infty}{L_\infty} \frac{\partial (\rho^* v^*)}{\partial y^*} = 0 \tag{2-26}$$

Multiplying both sides by  $\frac{\rho_\infty U_\infty}{L_\infty}$  gives

$$\frac{\partial \rho^*}{\partial t^*} + \frac{\partial (\rho^* u^*)}{\partial x^*} + \frac{\partial (\rho^* v^*)}{\partial y^*} = 0 \tag{2-27}$$

### 2.2.1.4. Momentum Equation

The momentum equation in the direction of x-axis is used the similar analysis,

$$\begin{aligned}
 & \frac{\rho_\infty U_\infty^2}{L_\infty} \frac{\partial(\rho^* u^*)}{\partial t^*} + \frac{\rho_\infty U_\infty^2}{L_\infty} \frac{\partial(\rho^* u^* u^*)}{\partial x^*} + \frac{\rho_\infty U_\infty^2}{L_\infty} \frac{\partial(\rho^* v^* u^*)}{\partial y^*} \\
 & = \frac{\mu_\infty U_\infty}{L_\infty^2} \frac{\partial}{\partial x^*} \left( \mu^* \frac{\partial u^*}{\partial x^*} \right) + \frac{\mu_\infty U_\infty}{L_\infty^2} \frac{\partial}{\partial y^*} \left( \mu^* \frac{\partial u^*}{\partial y^*} \right) \\
 & - \frac{\rho_\infty U_\infty^2}{L_\infty} \frac{\partial p^*}{\partial x^*} + \frac{\mu_\infty U_\infty}{L_\infty^2} \frac{\partial}{\partial x^*} \left[ \frac{1}{3} \mu^* \left( \frac{\partial u^*}{\partial x^*} - 2 \frac{\partial v^*}{\partial y^*} \right) \right] \\
 & + \frac{\mu_\infty U_\infty}{L_\infty^2} \frac{\partial}{\partial y^*} \left( \mu^* \frac{\partial v^*}{\partial x^*} \right) + \rho_\infty g_\infty \rho^* g_x^*
 \end{aligned} \tag{2-28}$$

After some rearrangement,

$$\frac{\partial(\rho^* u^*)}{\partial t^*} + \frac{\partial(\rho^* u^* u^*)}{\partial x^*} + \frac{\partial(\rho^* v^* u^*)}{\partial y^*} = \frac{\partial}{\partial x^*} \left( \Gamma_u^* \frac{\partial u^*}{\partial x^*} \right) + \frac{\partial}{\partial y^*} \left( \Gamma_u^* \frac{\partial u^*}{\partial y^*} \right) + b_u^* \tag{2-29}$$

where the dimensionless diffusion coefficient  $\Gamma_u^*$  is expressed as  $\frac{\mu^*}{\text{Re}}$ . The Reynolds number, the ratio of inertial forces to viscous forces, is defined as

$$\text{Re} = \frac{\rho_\infty U_\infty L_\infty}{\mu_\infty} \tag{2-30}$$

The dimensionless source term is expressed as

$$b_u^* = -\frac{\partial p^*}{\partial x^*} + \frac{\partial}{\partial x^*} \left[ \frac{1}{3} \Gamma_u^* \left( \frac{\partial u^*}{\partial x^*} - 2 \frac{\partial v^*}{\partial y^*} \right) \right] + \frac{\partial}{\partial y^*} \left( \Gamma_u^* \frac{\partial v^*}{\partial x^*} \right) + \frac{1}{Fr} \rho^* g_x^* \tag{2-31}$$

where a dimensionless parameter known as the Froude number

$$Fr = \frac{U_\infty}{L_\infty g_\infty} \tag{2-32}$$

is interpreted as the ratio of the inertial to gravity forces in the flow.



### 2.2.1.5. Energy Equation

The energy equation nondimensionalized by the dimensionless variables

$$\begin{aligned} & \frac{\rho_\infty U_\infty^3}{L_\infty} \frac{\partial}{\partial t^*} (\rho^* h_t^*) + \frac{\rho_\infty U_\infty^3}{L_\infty} \frac{\partial}{\partial x^*} (\rho^* u^* h_t^*) + \frac{\rho_\infty U_\infty^3}{L_\infty} \frac{\partial}{\partial y^*} (\rho^* v^* h_t^*) \\ &= \frac{k_\infty U_\infty^2}{L_\infty^2 C_{p,\infty}} \frac{\partial}{\partial x^*} \left( \frac{k^*}{C_p^*} \frac{\partial h_t^*}{\partial x^*} \right) + \frac{k_\infty U_\infty^2}{L_\infty^2 C_{p,\infty}} \frac{\partial}{\partial y^*} \left( \frac{k^*}{C_p^*} \frac{\partial h_t^*}{\partial y^*} \right) + S_{h_t} \end{aligned} \quad (2-33)$$

can be put into the dimensionless form.

$$\frac{\partial}{\partial t^*} (\rho^* h_t^*) + \frac{\partial}{\partial x^*} (\rho^* u^* h_t^*) + \frac{\partial}{\partial y^*} (\rho^* v^* h_t^*) = \frac{\partial}{\partial x^*} \left( \Gamma_{h_t}^* \frac{\partial h_t^*}{\partial x^*} \right) + \frac{\partial}{\partial y^*} \left( \Gamma_{h_t}^* \frac{\partial h_t^*}{\partial y^*} \right) + b_{h_t}^* \quad (2-34)$$

Here the dimensionless diffusion coefficient of energy equation is defined as

$$\Gamma_{h_t}^* = \frac{1}{\text{Re Pr}} \frac{k^*}{C_p^*} \quad (2-35)$$

in which the Prandtl number  $\text{Pr} = \frac{\mu_\infty C_{p,\infty}}{k_\infty}$  is a dimensionless number interpreted as the ratio of momentum diffusivity to thermal diffusivity. The dimensionless source term of energy equation  $S_{h_t}^*$  is

$$\begin{aligned} S_{h_t}^* = & -\frac{1}{\text{Re}_\infty \text{Pr}_\infty} \frac{\partial}{\partial x^*} \left[ \frac{k^*}{C_p^*} \frac{\partial}{\partial x^*} \left( \frac{V^{*2}}{2} \right) \right] - \frac{1}{\text{Re}_\infty \text{Pr}_\infty} \frac{\partial}{\partial y^*} \left[ \frac{k^*}{C_p^*} \frac{\partial}{\partial y^*} \left( \frac{V^{*2}}{2} \right) \right] \\ & + \frac{1}{\text{Re}_\infty} \frac{\partial}{\partial x^*} (u^* \tau_{xx}^* + v^* \tau_{xy}^*) + \frac{1}{\text{Re}_\infty} \frac{\partial}{\partial y^*} (u^* \tau_{yx}^* + v^* \tau_{yy}^*) \\ & + \frac{1}{Fr} \rho^* u^* g_x^* + \frac{1}{Fr} \rho^* v^* g_y^* + \frac{\partial p^*}{\partial t^*} \end{aligned} \quad (2-36)$$

### 2.2.1.6. Species Equation

The dimensionless variables are substituted into the species equation,

$$\begin{aligned} \frac{\rho_\infty U_\infty}{L_\infty} \frac{\partial(\rho^* Y_\alpha)}{\partial t^*} + \frac{\rho_\infty U_\infty}{L_\infty} \frac{\partial(\rho u Y_\alpha)}{\partial x} + \frac{\rho_\infty U_\infty}{L_\infty} \frac{\partial(\rho v Y_\alpha)}{\partial y} \\ = \frac{\rho_\infty D_\infty}{L_\infty^2} \frac{\partial}{\partial x^*} \left( \rho^* D_{\alpha,eff}^* \frac{\partial Y_\alpha}{\partial x^*} \right) + \frac{\rho_\infty D_\infty}{L_\infty^2} \frac{\partial}{\partial y^*} \left( \rho^* D_{\alpha,eff}^* \frac{\partial Y_\alpha}{\partial y^*} \right) \end{aligned} \quad (2-37)$$

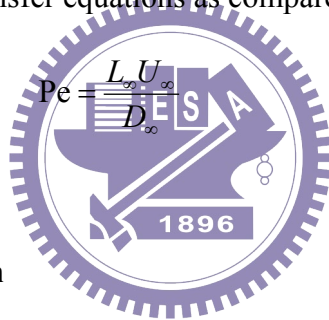
then the dimensionless species equation can be obtained.

$$\frac{\partial(\rho^* Y_\alpha)}{\partial t^*} + \frac{\partial(\rho^* u^* Y_\alpha)}{\partial x^*} + \frac{\partial(\rho^* v^* Y_\alpha)}{\partial y^*} = \frac{\partial}{\partial x^*} \left( \Gamma_{Y_\alpha}^* \frac{\partial Y_\alpha}{\partial x^*} \right) + \frac{\partial}{\partial y^*} \left( \Gamma_{Y_\alpha}^* \frac{\partial Y_\alpha}{\partial y^*} \right) \quad (2-38)$$

The dimensionless diffusion coefficient for species equation is defined as

$$\Gamma_{Y_\alpha}^* = \frac{\rho^* D_{\alpha,eff}^*}{Pe} \quad (2-39)$$

where the dimensionless parameter  $Pe$  is a measure of the relative magnitude of the diffusion term in the mass transfer equations as compared to the convection term.

$$Pe = \frac{L_\infty U_\infty}{D_\infty} \quad (2-40)$$


### 2.2.2. Spatial Discretization

The transport equations using the cell-centered finite-volume scheme can be written generally in integral form as

$$\frac{\partial}{\partial t} \int_{\Omega} \rho \phi d\Omega + \int_{\Gamma} \vec{F} \cdot \vec{n} d\Omega = \int_{\Omega} \rho \dot{\phi} d\Omega \quad (2-41)$$

where  $\Omega$  is the domain of interest,  $\Gamma$  is the surrounding surface, and  $\vec{n}$  is the unit normal in outward direction. The time derivative is calculated using the first-order forward difference scheme, and the source term is treated using last time step value.

The flux function  $\vec{F}$  consists of the inviscid and the viscous parts:

$$\vec{F} = \rho \vec{v} \phi - \mu \nabla \phi \quad (2-42)$$

The finite volume formulation of flux integral can be evaluated by the summation of the

flux vectors over each face,

$$\int_{\Gamma} \vec{F} \cdot \vec{n} d\Gamma = \sum_{j=k(i)} F_{i,j} \Delta\Gamma_j \quad (2-43)$$

where  $k(i)$  is a list of faces of cell  $i$ ,  $F_{i,j}$  represents convection and diffusion fluxes through the interface between cell  $i$  and  $j$ ,  $\Delta\Gamma_j$  is the cell-face area. The viscous flux for the face  $e$  between control volumes  $P$  and  $E$  as shown in Figure 1 can be approximated as:

$$\nabla\phi_e = \frac{\phi_P - \phi_E}{\Delta} \quad (2-44)$$

### 2.2.3. Upwind Scheme

The inviscid flux is evaluated through the values at the upwind cell and a linear reconstruction procedure to achieve second order accuracy as

$$\phi_e = \phi_u + \Psi_e \nabla\phi_u \cdot (\vec{r}_e - \vec{r}_u) \quad (2-45)$$

where the subscript  $e$  and  $u$  represents interface and the upwind cell, respectively, and  $\Psi_e$  is a flux limiter used to prevent from local extrema introduced by the data reconstruction. Defining  $\phi_{\max} = \max(\phi_u, \phi_j)$  and  $\phi_{\min} = \min(\phi_u, \phi_j)$ , where  $\phi_j$  is the neighbor cell of upwind cell, the  $\Psi_e$  associated with the gradient at cell  $u$  due to edge  $e$

is

$$\Psi_e = \begin{cases} \min\left(1, \frac{\phi_{\max} - \phi_u}{\phi_e^0 - \phi_u}\right), & \text{if } \phi_e^0 - \phi_u > 0 \\ \min\left(1, \frac{\phi_{\min} - \phi_u}{\phi_e^0 - \phi_u}\right), & \text{if } \phi_e^0 - \phi_u < 0 \\ 1, & \text{if } \phi_e^0 - \phi_u = 0 \end{cases} \quad (2-46)$$

where  $\phi_e^0$  is computed without the limiting condition (i.e.  $\Psi_e = 1$ )

### 2.2.4. Pressure Smoothing

The cell face velocity  $u_e$  is usually obtained by linear interpolation as

$$u_e = \frac{1}{2}(u_E + u_P) \quad (2-47)$$

In order to avoid the pressure oscillations due to simulation on a collocated grid, the face velocity can be modified as

$$u_e = \frac{1}{2}(u_E + u_P) + \left( \frac{\partial P}{\partial x} \frac{\delta \Omega}{A} \right)_{e1} - \left( \frac{\partial P}{\partial x} \frac{\delta \Omega}{A} \right)_{e2} \quad (2-48)$$

where  $A$  is the coefficient in the discretized momentum equation.

The first pressure gradient term is calculated as the mean value of cell  $P$  and  $E$ ,

$$\begin{aligned} \left( \frac{\partial P}{\partial x} \frac{\delta \Omega}{A} \right)_{e1} &= \frac{1}{2} \left( \left( \frac{\partial P}{\partial x} \right)_E + \left( \frac{\partial P}{\partial x} \right)_P \right) \left( \frac{\delta \Omega}{A} \right)_e \\ &= \frac{1}{2} \left( \frac{P_{EE} - P_P}{\delta x_{P,EE}} + \frac{P_E - P_W}{\delta x_{W,E}} \right) \left( \frac{\delta \Omega}{A} \right)_e \end{aligned} \quad (2-49)$$

The second one is calculated on the edge,

$$-\left( \frac{\partial P}{\partial x} \frac{\delta \Omega}{A} \right)_{e2} = -\left( \frac{P_E - P_P}{\delta x_{P,E}} \right) \left( \frac{\delta \Omega}{A} \right)_e \quad (2-50)$$

Set  $\delta x_{P,EE} = \delta x_{W,E} = 2\delta x_{P,E}$  and

$$u_e = \frac{1}{2}(u_E + u_P) + \frac{1}{4\delta x_{P,E}} \left( \frac{\delta \Omega}{A} \right)_e [P_{EE} - 3P_E + 3P_P - P_W] \quad (2-51)$$

which is used to calculate the convection flux through the control volume faces. The first term is treated as a weighted average, and the second one is kept as it is to deal with non-equidistant grids.

### 2.2.5. Velocity-Slip and Temperature-Jump Boundary Conditions

The velocity-slip boundary condition [Cercignani, 1988] is given as:

$$v_s - v_w = \zeta \left. \frac{\partial v}{\partial n} \right|_s \quad (2-52)$$

where  $v_s$  is the velocity of gas at the solid wall surface,  $v_w$  is the velocity of wall,

$\zeta = \frac{1 - \sigma_v}{\sigma_v} Kn$ ,  $\sigma_v$  is the tangential momentum accommodation coefficient,  $Kn$  is

the Knudsen number, and  $\left. \frac{\partial v}{\partial n} \right|_s$  is the derivative of velocity normal to the wall surface.

The temperature-jump is treated in a similar way:

$$T_s - T_w = \tau \left. \frac{\partial T}{\partial n} \right|_s \quad (2-53)$$

where  $T_s$  is the temperature of gas at the solid wall surface,  $T_w$  is the temperature of

wall,  $\tau = \frac{2 - \sigma_T}{\sigma_T} Kn$ ,  $\sigma_T$  is the thermal accommodation coefficient, and  $\left. \frac{\partial T}{\partial n} \right|_s$  is the

derivative of temperature normal to the wall surface.



### 2.3. Solution Procedure

A general implicit discretized time-marching scheme for the transport equations is employed to solve the discretized equations. It can be written as:

$$\left( \frac{\rho^n}{\Delta t} + A_p \right) \phi_p^{n+1} = \sum A_{NB} \phi_{NB}^{n+1} + \frac{(\rho \phi_p)^n}{\Delta t} + S_\phi^n \quad (2-54)$$

where the superscripts  $n$  and  $n+1$  mean old value (at time  $t$ ) and new value (at time  $t+dt$ ) of the variables, respectively. The high order differencing terms and cross diffusion terms are treated using known quantities and retained in the source term and updated explicitly.

In an extended SIMPLE [Chen (1989), Shang et al. (1995), Shang and Chen (1997), and Zhang et al. (2001)] family pressure-correction algorithm, the pressure correction

equation for all-speed flows is formulated using the perturbed equation of state, momentum and continuity equations. The simplified formulations can be written as

$$\rho' = \frac{p'}{RT} \quad (2-55.a)$$

$$u'_m = -D_u \nabla p' \quad (2-55.b)$$

$$u^{k+1} = u^k + u' \quad (2-55.c)$$

$$p^{k+1} = p^k + p' \quad (2-55d)$$

$$\frac{\partial \rho}{\partial t} + \nabla(u'_m \rho') + \nabla(\rho u'_m) = -\nabla(\rho u_m)^k \quad (2-55.e)$$

where  $R$  is the ideal gas constant,  $u_m$  is the  $m^{th}$  Cartesian component of the velocity, and  $D_u$  is the pressure-velocity coupling coefficient. Considering

$\Delta \rho = \rho^{k+1} - \rho^n = (\rho^{k+1} - \rho^k) + (\rho^k - \rho^n) = \rho' + (\rho^k - \rho^n)$ , the following all-speed pressure correction equation is obtained,

$$\frac{1}{RT} \frac{p'}{\Delta t} + \nabla \left( \frac{u_m}{RT} p' \right) - \nabla (\rho D_u \nabla p') = - \left( \frac{\rho^k - \rho^n}{\Delta t} \right) - \nabla (\rho u_m)^k \quad (2-56)$$

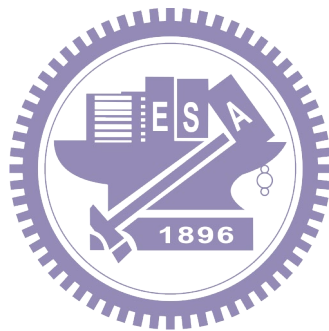
where the superscript  $k$  represents the last iterative value.

The numerical algorithm for solving unsteady, compressible, viscous and heat-conducting gas flows consists the following steps:

1. Initialize the  $u$ ,  $v$ ,  $P$ ,  $T$  and other parameters. Set time step  $\Delta t$ .
2. Set the initial conditions for the calculated time step.
3. Extended SIMPLE algorithm
  - 3.1 Solve the momentum equations at the predictor step.
  - 3.2 Solve the pressure-correction equation.
  - 3.3 Update the velocity, and pressure.
  - 3.4 Solve the secondary pressure-correction equation.

- 3.5 Update the velocity, and pressure again.
  - 3.6 Solve the energy and species conservation equations.
  - 3.7 Check for convergence of the iteration process. Repeat step 3 until a converged solution is obtained.
4. March to next time step and return to step 2 until a steady-state solution is obtain.

A basic description of the simulation processes is available in Figure 2-2. In addition, parallel computing is implemented and tested on distributed-memory machines using spatial domain decomposition.



## Chapter 3

# Verifications and Parallel Performance of the Gas Flow Model

In order to validate the feasibility of the developed gas flow model, several simulations from incompressible, low-speed to compressible, high-speed flow and problems with considering conjugate heat transfer were compared with previous simulations wherever possible. The weakly compressible lid-driven cavity flow has been frequently used as the benchmark problem for validation. It was chosen to test the capability of gas flow model in solving the incompressible flow problems. A two-dimensional square cavity with a heat conducting square cylinder at different locations is considered for validating that the gas flow model is suitable for flow problems considering the conjugate heat transfer. The validation of the gas flow model applied in a supersonic gas flow past a confined square in a micro-channel is to demonstrate the ability of the gas flow model in solving high-speed flow problems.

### 3.1. Lid-driven Cavity Flow

#### 3.1.1. Simulation Conditions

The problem considers the fluid in a two-dimensional square cavity with an upper wall moving in the x-direction at a velocity  $u$  as shown in Figure 3-1. The other walls are stationary with the no-slip boundary condition. The pressure and temperature at the boundary are given a Neumann boundary condition, meaning that the normal gradients of pressure and temperature are zero. A wide range of Reynolds numbers has been



studied. Solutions are obtained for configurations with non-uniform meshes consisting of 128 by 128 cells.

### 3.1.2. Validation with Previous Simulations

The streamlines for the driven cavity flow with increasing Reynolds number from 100 to 10,000 along with those by Ghia et al. [1982] are shown in Figure 3-2 and 3-3. As is well known, the center of primary vortex is offset near the top right corner at  $Re = 100$ . It moves towards the geometric center of the cavity with increasing  $Re$ . The simulation results are in good agreement with those published in the literature. It is clearly that the current gas flow model is capable of reproducing the flow fields as Ghia et al. [1982] at near-incompressible flow limit in the wide range of Reynolds numbers.

## 3.2. Low-Speed Gas Flow with Conjugate Heat Transfer

### 3.2.1. Simulation Conditions

To demonstrate the capability of the solver to simulate gas flow with considering the conjugate heat transfer, we have chosen the conjugate heat transfer problem simulated by Rahman et al. [2008], as shown in Figure 3-4.

The Richardson number ( $Ri = g\beta(T_h - T_i)L/u_i^2$ ), a dimensionless parameter represents the importance of natural convection relative to the forced convection, for this investigation is set as 0 to 5, where  $g$  is the gravitational acceleration,  $\beta$  is the thermal expansion coefficient,  $L$  is the length of the square cavity,  $u_i$  is the inlet velocity, and  $T_h$  and  $T_i$  are the temperature of heated wall and inlet, respectively.  $L$  and  $u_i$  are assumed as the characteristic length, and velocity, and the corresponding Reynolds number is keeping equal to 100. The inlet width and the square block width are equal to  $0.1L$  and  $0.2L$ , respectively. The solid fluid thermal conductivity ratio

$\frac{k_s}{k_f}$  is equal to 5, where  $k_s$  and  $k_f$  are the heat conductivities of the solid and gas, respectively.

The boundary conditions are given as follows:

At the inlet ( $\overline{BC}$ ):

$$u = u_i, v = 0, T = T_i, P = \text{extrapolation} \quad (3-1)$$

At the outlet ( $\overline{FE}$ ):

$$\frac{\partial[\phi(=u, v, T)]}{\partial n} = 0, P = \text{fixed} \quad (3-2)$$

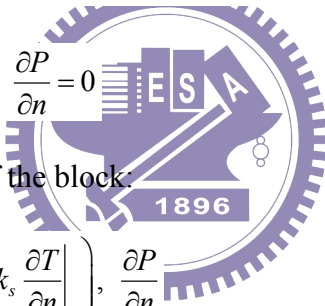
At the wall boundaries:

$$\overline{AB}, \overline{CD}, \text{ and } \overline{FA}: u = 0, v = 0, \frac{\partial[\phi(=P, T)]}{\partial n} \quad (3-3)$$

$$\overline{DE}: u = 0, v = 0, T = T_h, \frac{\partial P}{\partial n} = 0 \quad (3-4)$$

At the solid-fluid interfaces of the block:

$$u = 0, v = 0, \left( k_f \frac{\partial T}{\partial n} \Big|_f = k_s \frac{\partial T}{\partial n} \Big|_s \right), \frac{\partial P}{\partial n} \quad (3-5)$$



### 3.2.2. Validation with Previous Simulations

Flow over a solid cylinder in a square cavity is considered. Air is used as the working fluid in the cavity.  $100 \times 100$  uniform computational cells are used for simulations throughout the study. Conjugate heat transfer is considered by solving a steady-state heat conduction equation within the square block and by enforcing the heat flux continuity at the interfaces between gas and solid.

Figure 3-5 to 3-10 show the stream lines and isotherms at  $Ri = 0$ ,  $Ri = 1$ , and  $Ri = 5$  for four configurations of the blocks in the cavity along with the data of Rahman et al. [2008]. The comparisons show good agreement between the two

simulations while the temperature difference ( $T_h - T_i$ ) is small.

At smaller temperature gradient, the stream lines and isotherms are almost the same as those obtained by Rahman et al.; however, as the temperature difference becomes large, the flow and thermal patterns shown in Figure 3-11 and 3-12 deviate greatly from those by Rahman et al. [2008]. The results indicate that the Boussinesq approximation as often assumed by most of the simulations for mixed convection problems; especially at high Richardson number is highly questionable. For this type of flow, a compressible viscous gas flow model is necessary.

### 3.3. Micro-scale High-Speed Gas Flow with Slip Boundary Conditions

#### 3.3.1. Simulation Conditions

A 2D compressible laminar flow around a square cylinder with size  $a$  ( $a=1.4 \mu\text{m}$ ) confined in a micro-channel (height  $H_{ch}=10a$ , length  $L_{ch}=50a$ ) is simulated to demonstrate the capability of handling supersonic flow with slip boundary conditions as shown in Figure 3-13.

The reference parameters based on the inlet state for this problem are:  $P_0 = P_{in}$ ,  $T_0 = T_{in}$ ,  $\rho_0 = \frac{P_0}{RT_0}$ , and  $V_0 = \sqrt{2RT_0}$ , where the subscript *in* represents the inlet state.

The square size  $a$  is chosen as the characteristic length, the corresponding Mach number and Knudsen number in the study are  $2.4261$  and  $0.05$ , respectively. Velocity-slip and temperature-jump boundary conditions are implemented in the study. The blockage ratio  $a/H_{ch}$  is equal to  $0.1$  and the distance between square and the channel inlet ( $L_a$ ) is equal to  $5.5a$ .

The boundary conditions applied in this problem are as follows:

At the inlet:

$$u = u_i, v = 0, T = T_i, P = P_i \quad (3-6)$$

At the outlet:

$$\frac{\partial [\phi(=u, v, T, P)]}{\partial n} = 0 \quad (3-7)$$

At the wall boundaries:

$$u = u_i, v = 0, \frac{\partial [\phi(=P, T)]}{\partial n} \quad (3-8)$$

At the solid-fluid interfaces of the square:

$$u = 0, v = 0, \left( k_f \frac{\partial T}{\partial n} \Big|_f = k_s \frac{\partial T}{\partial n} \Big|_s \right), \frac{\partial P}{\partial n} \quad (3-9)$$

### 3.3.2. Validation with Previous Simulations

The distribution of flow properties in the channel is shown in Figure 3-14. The results show that there is a strong bow shock, also called a detached shock, forming in front of the square. Downstream of the bow shock, the pressure, density, and temperature of the flow rise rapidly; the velocity of the fluid drops from "supersonic" to "subsonic".

The comparison of the normalization distribution of horizontal velocity and temperature obtained by Shterev and Stefanov [2010] (steps  $\Delta = 0.00625$ ,  $8000 \times 1600$  cells), and the present ( $2000 \times 400$  cells) are shown in Figure 3-15 and 3-16. The results obtained that the agreement between gas flow model and SIMPLE-TS data is very good.

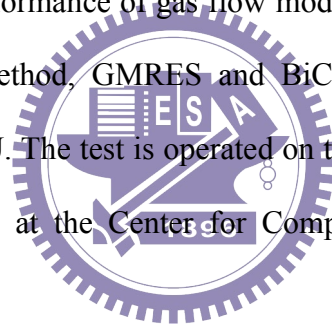
Figures 3-17 to 3-20 show the comparisons of horizontal velocity and temperature along the center line of the channel ( $y = H_{ch}/2$ ) with the simulation data [Shterev and Stefanov, 2010] for different spatial steps. The obtained by the gas flow model with

much lower resolution ( $500 \times 100 - 2000 \times 400$  cells) is in a good agreement with those calculated by the SIMPLE-TS method using much higher resolution ( $2000 \times 400 - 8000 \times 1600$  cells). It clearly shows that to obtain a receivable result by SIMPLE-TS method needs to carry out very long calculations compared to those of gas flow model.

### **3.4. Parallel Performance Study**

#### **3.4.1. Test Conditions**

The two-dimensional micro-scale supersonic gas flow as shown earlier is used for parallel performance study. 2,000 by 400 uniform computation cells are considered in the study. The parallel performance of gas flow model is investigated by using two type of Krylov subspace method, GMRES and BiCGStab, where the subdomain problems were solved by ILU. The test is operated on the V'ger cluster system (Xeon 3GHz dual-core, dual-CPU) at the Center for Computation Geophysics, National Central University, Taiwan.



#### **3.4.2. Results and Discussion**

Figure 3-21 shows the variation of the parallel performance and computation times per time step as a function of the number of processors. The parallel performance is tested by applying GMRES or BiCGStab as the KSP solver and ILU as the sub-domain solver. Result shows speedup is about 46 times as 64 processors are used for the test case with GMRES as the KSP solver. The parallel speedup using GMRES-ILU is slightly better than using BiCGStab-ILU, and the absolute runtime of case using GMRES-ILU is relatively short.

### **3.5. Summary**

In this chapter, the validations of the gas flow model and parallel performance were presented. The validation is found to be very good agreement with previous simulations. Parallel efficiency is reasonably good up to 64 processors with parallel efficiency of ~70%.



## Chapter 4

### Applications in Low-Temperature Plasma Discharge

This chapter presents the gas flow model coupling with the plasma fluid modeling applied in low-temperature plasma discharge. Figure 4-1 to 4-4 exhibit the plasma properties include electron number density, electron temperature, and ion number densities in an atmospheric-pressure plasma jet w/ and w/o considering the neutral gas flow model. These results demonstrate that influence of gas flow model in the low-temperature plasma discharge should not be underestimated.

#### 4.1. Simulation of Silane/Hydrogen Gas Discharge in a Plasma Enhanced Chemical Vapor Deposition (PECVD) Chamber

This phase demonstrates a large-scale realistic PECVD using the mixture Silane/Hydrogen gas. In order to get a uniform thickness of coating, optimization of the flow streamlines with respect to the influence of deposition parameters by using numerical simulation is necessary. Figure 4-5 show the schematic diagram of the PECVD chamber. Due to the symmetry of the plasma chamber, only half domain is considered in this simulation.

##### 4.1.1. Simulation Conditions

Simulation conditions in this study include: (1) chamber pressure (600 *mtorr*); (2) a square glass plate (20  $\text{\AA}$ ~ 20 *cm*); (3) substrate temperature (250  $^{\circ}\text{C}$ ); (4) gap distance between shower-head and substrate (14 *mm*) and (5) inflow rate ratio of silane to hydrogen (50 : 80 *sccm*).

The boundary conditions used in the gas flow model are defined as

At the gas inlet:

$$u = 0, v = v_i, T = T_i, P = \text{extrapolation}, Y = Y_i \quad (4-1)$$

where  $v_i$  is calculated depending on the gas flow rate, the cross section of the shower head, and background pressure using a temperature of 300 K.

At the outlet:

$$\frac{\partial[\phi(=u, v, T, Y)]}{\partial n} = 0, P = P_{\text{fixed}} \quad (4-2)$$

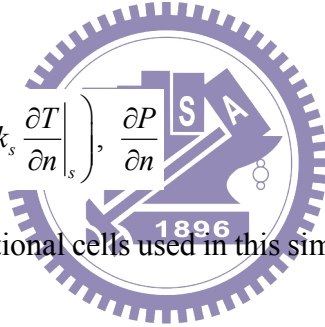
At the substrate surface:

$$u = 0, v = 0, T = T_s, \frac{\partial[\phi(=P, Y)]}{\partial n} \quad (4-3)$$

At the solid-fluid interfaces:

$$u = 0, v = 0, \left( k_f \frac{\partial T}{\partial n} \Big|_f = k_s \frac{\partial T}{\partial n} \Big|_s \right), \frac{\partial P}{\partial n} \quad (4-4)$$

The schematic of the computational cells used in this simulation is shown in Figure 4-6.



#### 4.1.2. Results and Discussion

The steady-state neutral flow field including the distributions of species number density, temperature and mass-averaged velocities are simulated by using the developed gas flow model. The applied frequency was 25 kHz and the total gas pressure was 600 mTorr. These properties were then used in the plasma fluid modeling as the background gas properties. Figure 4-7 to 4-8 show the distributions of  $H_2$  and  $SiH_4$ , and gas temperature. In this case, the Reynolds number is small with inflow velocity of silane/hydrogen and gap distance as the characteristic velocity and length, respectively. A small Reynolds number leads to a small Peclet number ( $Pe = Re \cdot Pr$ ), which means that the conduction is dominated. This phenomenon is clearly seen in



Figure 4-7, where the temperature distribution between the electrode and substrate is almost linear. In addition, the density near the substrate surface decreases greatly because of the heated substrate at elevated temperature (250 °C). Non-uniform background density is important in determining the ionization rate during the simulation. The detailed flow structure is given by the streamlines in Figure 4-9.

## 4.2. Simulation of a Helium Micro-Cell Plasma

### 4.2.1. Simulation Conditions

Figure 4-10 shows the schematic diagram of a micro-cell plasma investigated in this study. The micro-cell consists of two ring-shaped electrodes made of aluminum separated by an insulator. The powered electrode is connected to an RF power source ( $f=13.56$  MHz) with amplitude of 300 Volt, and the other one is grounded. Helium gas is applied as the working gas under the atmospheric-pressure condition. This study is numerically solved in a cylindrical coordinate in the right region in Figure 4-10.  $40 \times 60$  uniform computational cells is used in x- and y-direction, respectively. Table 4 lists the substance properties used in this study. A gravitational field  $\vec{g}$  is considered in the negative y-direction.

The boundary conditions for helium micro-cell plasma include:

At domain boundaries:

$$T=T_{\infty} \quad (4-5)$$

At the solid-fluid interfaces:

$$u = 0, v = 0, \left( k_f \frac{\partial T}{\partial n} \Big|_f = k_s \frac{\partial T}{\partial n} \Big|_s \right), \frac{\partial P}{\partial n} \quad (4-6)$$

#### 4.2.2. Results and Discussion

The present study numerically investigates the characteristics of flow field and heat transfer in a helium micro-cell plasma at atmospheric pressure. Figure 4-11 and 4-12 show the force due to ion-molecule collisions generated by the plasma fluid model for x- and y-momentum equations, respectively. And the energy source due to ion Joule heating and electron elastic collision is shown in Figure 4-13.

Figure 4-14 shows the temperature distribution without considering the plasma momentum sources. The helium gas is heated and the maximum temperature in the plasma region is about 307 K. The increasing temperature produces an increase in the flow field due to the buoyancy effect. As expected, the buoyancy effect leads a weak clockwise flow field shown in Figure 4-15. However, the situation is totally different when the plasma momentum sources are considered. The clockwise flow field is reversed into a counter-clockwise field shown in Figure 4-16. There is a large component of the force ( $F_{plasma} = [S_v^2 + S_r^2]^{1/2}$ ) directed toward the powered electrode shown in Figure 4-17. The intensity of the force per unit volume is extremely larger than the buoyancy force, which leads an opposite flow field. The flow is accelerated to a speed of 0.8 m/s. Figure 4-18 shows the distributions of temperature with considering the plasma momentum sources.

### 4.3. Simulation of a Helium Dielectric Barrier Discharge Atmospheric-Pressure Plasma Jet

In the present study, a helium planar dielectric barrier discharge atmospheric-pressure plasma jet (APPJ) designed by our group members shown in Figure 4-19 is simulated using the developed gas flow model coupling with a two-dimensional parallelized plasma fluid modeling code developed by another group

member [Lin, 2010]. The converged steady-state results of flow field, temperature, and other neutral gas properties are present.

#### 4.3.1. Simulation Conditions

The schematic of the helium dielectric barrier discharge atmospheric-pressure plasma jet used in this study is illustrated in Figure 4-20. This system consists of two parallel electrodes made of copper and each of the electrodes is cuboid of  $25 \times 50 \times 8 \text{ mm}^3$ . The lower electrode is connected to an AC power source ( $f=25 \text{ kHz}$ ) with amplitude of 250 Volt, and the upper one is grounded. Each electrode is covered with a  $35 \times 70 \times 1 \text{ mm}^3$  ceramic plate as the dielectric. The gap spacing between the two dielectric plates is kept at 1 mm throughout the study. Helium gas with nitrogen impurity (100ppm) is applied under the atmospheric-pressure condition. The total gas flow rate passing with a cross section of  $1 \times 50 \text{ mm}^2$  is fixed at 20 slm.

In addition, the initial background gas temperature is assumed to be 300 K, and the surroundings are filled with air (78%  $\text{N}_2$  and 22%  $\text{O}_2$ ). The substrate surface is specified under two kinds of boundary conditions: a) an adiabatic wall (Neumann boundary) and b) an isothermal wall (Dirichlet boundary).

The boundary conditions for the helium dielectric barrier atmospheric-pressure plasma jet include:

At the gas inlet:

$$u = u_i, v = 0, T = T_i, P = \text{extrapolation}, Y = Y_i \quad (4-7)$$

where  $u_i$  is calculated depending on the gas flow rate, the cross section of inlet, and background pressure using a temperature of 300 K.

At the outlet:

If the gas flows out of the domain,

$$\frac{\partial[\phi(=u, v, T, Y)]}{\partial n} = 0, P = P_{fixed} \quad (4-8)$$

Otherwise,

$$\frac{\partial[\phi(=u, v,)]}{\partial n} = 0, T = T_{amb}, P = f(P_i), Y = Y_{amb} \quad (4-9)$$

where the subscript “*amb*” means the state of the surrounding environment.

At the substrate surface:

Isothermal wall:

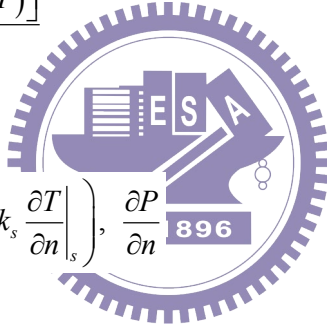
$$u = 0, v = 0, T = T_s, \frac{\partial[\phi(=P, Y)]}{\partial n} \quad (4-10)$$

Adiabatic wall:

$$u = 0, v = 0, \frac{\partial[\phi(=T, P, Y)]}{\partial n} \quad (4-11)$$

At the solid-fluid interfaces:

$$u = 0, v = 0, \left( k_f \frac{\partial T}{\partial n} \Big|_f = k_s \frac{\partial T}{\partial n} \Big|_s \right), \frac{\partial P}{\partial n} \quad (4-12)$$



### 4.3.2. Results and Discussion

A two-dimensional helium dielectric barrier discharge atmospheric-pressure plasma jet is investigated by solving the governing conservation equations with the boundary conditions. According to the gap between the two dielectric layers, the Reynolds number is estimated to be about 60. The gas flow is assumed to be laminar. The Knudsen number related to the Mach number and the Reynolds number is less than 0.001, and the gas is treated as continuum. For this reason, the no-slip condition is imposed at the boundary. The  $160 \times 160$  non-uniform computational cells shown in the Figure 4-21 are employed in the simulation. The parallelized neutral gas flow model uses 8 processors in x-direction and 5 processors in y-direction, respectively.

Figure 4-22 shows the time-history of the velocity and temperature profiles at the export of helium dielectric barrier discharge at atmospheric-pressure with gas flow rate of 20 slm under two kinds of boundary conditions of substrate surface. The computations are continued until it is obtained that the fluid properties have reached a statistically stationary state. It is seen the gas velocity at the exit of the plasma jet increase achieved a maximum velocity of about 14 m/s. The result in an adiabatic substrate surface is quite similar to that in an isothermal substrate surface. The steady-state solutions of the maximum temperatures at the exit of the plasma jet are 321 K and 322.5 K for the adiabatic and isothermal substrate surfaces, respectively.

The two-dimensional spatial distributions of pressure and over-all density are shown in Figure 4-23. The inlet pressure is approximately 760.5 torrs. In Figure 4-24, the spatial distributions of temperature for  $d=1$  mm,  $H/d=10$ ,  $Re=60$  and gas flow rate of 20 slm are shown for two different thermal boundaries. The gas is heating due to ion Joule heating and electron-neutral elastic collision. The maximum shown temperature in the plasma channel is about 323 K.

The velocity components in x- and y-direction are presented in Figure 4-25. Figure 4-26 shows the spatial distributions of the mean-speed, stream lines, and velocity vector. In the stagnation region, the fluid velocity is zero and the surrounding flow is turning into the wall direction. Results illustrate that there are several pairs of vortices formed in the region between the jet exit and substrate and shown almost symmetric pattern. Figure 1 shows the steady-state velocity vectors and streamlines at  $Re=60$ ,  $H/d=10$ , and gas flow rate of 20 slm. The locations of primary and secondary vortices are depicted in Figure 4-27. A counter-clockwise primary vortex is formed near to the jet exit owing to low-pressure formation near the jet exit. When the momentum of the jet is unable to overcome retarding effect of the primary vortex and

the opposing frictional force of the impingement plate, the clockwise secondary vortex is formed. Figure 4-28 show the numerical simulated stream lines at different time level for  $d = 1 \text{ mm}$ ,  $H/d = 10$ ,  $Re = 60$  and gas flow rate of 20 slm . The results denote that the primary and secondary vortices glow and move toward the outlet as time increases. Finally, the flow converges to its steady state.

Figure 4-29 shows the horizontal velocity profiles in the plasma channel at different x position. The entrance length, a length in the channel until the flow velocity profile is fully developed, correlation with the Reynolds Number for laminar flow can be expressed as  $0.06Re$  . It is clear that the flow is nearly fully developed with a parabolic velocity profile. The temperature profile in the plasma channel at various x positions is illustrated in Figure 4-30. The temperature difference between an adiabatic and an isothermal substrate surface is about 3 K.

Figure 4-31 shows the horizontal velocity and temperature profiles along the center line of the plasma jet. The gas flow velocity increases with increasing the distance from the inlet, and reaches a nearly constant value about 11.8 m/s in the plasma channel. A pronounced reduction in the velocity of the helium gas can be observed out of the plasma channel. The gas temperature in the plasma region is continuously increasing due to the electron-neutral elastic collision and ion Joule heating. The maximum values in the plasma channel, respectively, are about 324.5 K and 322.8 K for adiabatic and for isothermal boundaries. The gas temperature outside the plasma region decreases with the distance, as expected. Vertical velocity and temperature profiles between helium DBD APPJ and substrate at different y positions for  $d = 1 \text{ mm}$ ,  $H/d = 10$ ,  $Re = 60$  and gas flow rate of 20 slm are shown in Figure 4-32 and 4-33.

The local Nusselt number distribution along the isothermal substrate surface for

$d = 1 \text{ mm}$ ,  $H/d = 10$ ,  $Re = 60$  and gas flow rate of 20 slm is obtained in Figure. 4-34. The local Nusselt number, a ratio of convective to conductive heat transfer normal to the surface, is defined as:

$$Nu = \frac{hd}{k} = -\frac{d}{(T_{bulk} - T_i)} \left( \frac{dT}{dx} \right)_s \quad (4-13)$$

where  $h$  is local heat transfer coefficient, and  $T_{bulk}$  is the bulk temperature. The bulk temperature  $T_{bulk}$  in this study is defined as follows:

$$\dot{m} (T_{bulk} - T_i) = Q_{FM} \quad (4-14)$$

where  $\dot{m}$  is the helium mass flow rate, and  $Q_{FM}$  is the heat source generated from the plasma fluid modeling. The local Nusselt number would not change significantly if the substrate surface treated as an adiabatic wall. A typical bell-shaped profile is obtained near the stagnation point while the substrate surface is kept at 300 K. The local Nusselt number variation in the substrate surface presents a peak of 2.37 at the stationary point for  $d = 1 \text{ mm}$ ,  $H/d = 10$ ,  $Re = 60$  and gas flow rate of 20 slm. Thereafter, the Nu decreases monotonically.

## Chapter 5

# Parametric Study of a Helium Dielectric Barrier Discharge Atmospheric-Pressure Plasma Jet

The purpose of this parameter study is to determine the influences of the system configurations, and the flow conditions on the flow and heat transfer characteristics of a helium dielectric-barrier discharge atmospheric-pressure plasma jet. The parameters varied in this study are the electrode lengths ( 5 mm and 25 mm ), gas flow rates( 10 – 30 slm ), and dimensionless jet-to-substrate spacing rates,  $H/d$  (5, 7.5, 10, 12.5, and 15). The simulations are performed using helium with nitrogen impurity (100ppm) as the working gas. The neutral flow properties including velocity, pressure, total enthalpy, and species concentrations et al., are calculated by using the co-located cell finite volume method. The results are presented in the following sections.

### 5.1 The Effect of Electrode Length

#### 5.1.1 Simulation Conditions

The two systems consist of two parallel electrodes made of copper. The electrodes of two systems are cuboid of  $25 \times 50 \times 8 \text{ mm}^3$  and of  $5 \times 50 \times 8 \text{ mm}^3$ , respectively. The powered electrode is connected to an AC power source ( $f=25 \text{ kHz}$ ) with amplitude of 250 Volt. The electrodes of two systems are respectively covered with  $35 \times 70 \times 1 \text{ mm}^3$  and  $15 \times 70 \times 1 \text{ mm}^3$  ceramic plates. The gap spacing between the two dielectric plates is kept at 1 mm throughout the two systems. Helium gas with nitrogen impurity (100ppm) is applied under the atmospheric-pressure



condition. The total gas flow rate is fixed at 20 slm.

For studying the influence of electrode length on the heat transfer and flow characteristics, the electrode length varies from 5 mm to 25 mm and the other parameters remain the same as in Chapter 4.  $140 \times 160$  and  $160 \times 160$  non-uniform, computational cells are used for the electrode lengths of 5 mm and 25 mm, respectively.

### 5.1.2 Results and Discussion

In this study, the value of velocity, pressure, total enthalpy, and species concentration are calculated numerically for two different electrode lengths. Figure 5-1 to 5-3 show the steady-state solutions of flow properties including pressure, over-all density, temperature, and velocity components. The heating source generated by plasma will decrease due to reduce the electrode length. Short electrode length leads to small plasma region, which results in decreased power source generated by plasma. The temperature in short electrode length rises from 300 K to 305.5 K. However, the flow field and the distributions of species mole fraction are no significant different between two different electrode lengths.

## 5.2 The Effect of Jet-to-Substrate Spacing Rate

### 5.2.1 Simulation Conditions

In order to determinate the effect of the dimensionless jet-to-substrate spacing rats on the flow and temperature fields in a simulation of helium dielectric barrier discharge atmospheric-pressure plasma jet, the numerical simulations are performed for five different  $H/d = (5, 7.5, 10, 12.5, \text{ and } 15)$ .

The number of computational cells used in the present calculations for various

jet-to-substrate spacing rates is list Table 5. The simulations are advanced in time until the flow properties reach to the steady-state solutions.

### 5.2.2 Results and Discussion

The influence of the jet-to-substrate spacing rate on the flow and temperature is determined. Simulations of flow properties are done by setting the dimensionless jet-to-substrate spacing rates  $H/d$  from 5 to 15.

The temperature distributions, respectively, for an adiabatic boundary and for an isothermal boundary for the effect of various jet-to-substrate spacing rates are plotted in Figure 5-4 and 5-5. It can be seen that the jet-to-substrate spacing rate has an important effect on the heat transfer performances. The temperature distribution for an adiabatic boundary is relatively high to that for an isothermal boundary. Figure 5-6 shows the comparison of the mean speed distributions for various jet-to-substrate spacing rates. The predicted streamlines for the jet-to-substrate spacing rates of  $H/d = (5, 7.5, 10, 12.5, \text{ and } 15)$  at the plasma jet exit region are shown in Figure 5-7. It is observed that the size of the primary vortex increases with increasing the jet-to-substrate spacing ratio. With increasing jet-to-substrate spacing rate, the turning acceleration and the velocity in the flow transverse direction will decrease. Figure 5-8 to 5-10 show the distributions of species mole fraction.

Variation in the local Nusselt number distribution with dimensionless jet-to-substrate spacing ( $H/d$ ) can be seen in Figure 5-11. It is clear that the relative decrease in the local Nusselt number with increasing the dimensionless jet-to-substrate spacing. This is due to the convection effect. The local Nusselt number at the stationary point decreases from 3.7 to 1.8 with the dimensionless jet-to-substrate spacing increasing from 5 to 15. The smallest dimensionless jet-to-substrate spacing rate

( $H/d = 5$ ) yielded the largest Nusselt number at the stagnation point for gas flow rate of 20slm.

### 5.3 The Effect of Gas Flow Rate

#### 5.3.1 Simulation Conditions

The influence on the flow and heat transfer characteristics of a helium dielectric-barrier discharge atmospheric-pressure plasma jet is investigated for various gas flow rates. The parameters used in this study are the same as the Chapter 4, except the gas flow rate.

#### 5.3.2 Results and Discussion

The fluid flow and heat transfer for a helium dielectric barrier discharge atmospheric-pressure jet tested for different helium gas flow rates are presented. Figure 5-12 shows the comparisons of the temperature distributions for an adiabatic substrate for gas flow rates between 10 and 30 slm. It is observed that a higher gas flow rate brings a lower temperature distribution. This phenomenon can also be discovered at the temperature distributions for an isothermal substrate shown in Figure 5-13. A higher gas flow rate is corresponding to a higher gas velocity shown in Figure 5-14. A constant thermal source provided by the plasma fluid model resisting a higher gas velocity leads a lower temperature distribution. The predicted streamlines for various gas flow rates with  $H/d = 10$  are presented in Figure 5-15. It is observed that there is a slight change in position and size of the vortexes as the gas flow rate changes. Figure 5-16 to 5-18 show the comparison of the distributions of species mole fraction for various gas flow rates.

Figure 5-19 shows the time-histories of velocity at the export of the helium

dielectric barrier discharge atmospheric-pressure jet for various helium gas flow rates and for different thermal boundaries. The jet exit velocity increases from 6 to 17 m/s with increasing the helium gas flow rate from 10 slm to 30 slm for  $d = 1$  mm and  $H/d = 10$ . The jet exit temperature as a function of time for different helium gas flow rates for two different thermal boundaries is shown in Figure 5-20. At the plasma jet exit, the temperatures decrease, respectively, from 342 to 317 K for an adiabatic boundary and from 329 to 314 K for an isothermal boundary with increasing the gas flow rate from 10 to 30 slm. Figure 5-21 and 5-22 show the horizontal velocity and temperature profiles along the center line of the helium DBD APPJ for various gas flow rates.

The approximated Reynolds numbers based on plasma jet gap distance and inflow conditions increase from 30 to 90 with increasing the helium gas flow rate from 10 slm to 30slm. The bulk temperatures for various gas flow rates are list in Table 6. The bulk temperature decreases significantly with increasing the gas flow rate. A strong dependence of heat transfer on gas flow rate is shown. Figure 5-23 shows the local Nusselt number distributions along the substrate surface for various gas flow rates. The local Nusselt numbers at the stationary point show a maximum value of 38.4 for gas flow rate of 30 slm, and a minimum value of 10.2 for gas flow rate of 10slm. Higher gas flow rate generates strong convection effects, which results in higher Nu.

## 5.4 Summary

Numerical simulations to investigate the flow and heat transfer characteristics in a helium dielectric barrier discharge atmospheric-pressure jet are carried out for different electrode lengths, jet-to-substrate spacing rates, and helium gas flow rates.

## Chapter 6

### Conclusion and Recommendations for Future Study

#### 6.1 Summaries of This Thesis

In this thesis, a parallelized 2D/2D-axisymmetric pressure-based, finite-volume gas flow model has been reported. Implementation and validations against earlier simulations data are described in detail. Developed code is then applied to simulate two-dimensional silane/hydrogen gas discharge in a PECVD chamber, helium micro-cell plasma and helium dielectric barrier discharge atmospheric-pressure plasma jet.

The main conclusions of this study can be briefly summarized as follows:

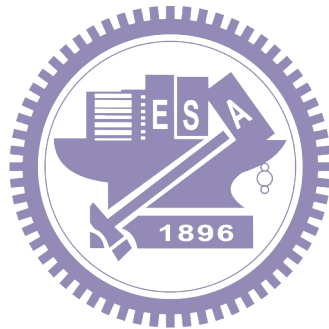
1. Parallelized 2D gas flow model using finite-volume method for simulating compressible, viscous, heat conductive and rarefied gas flows at all speeds with conjugate heat transfer was developed and validated against previous simulations.
2. Parallel efficiency of a micro-scale supersonic channel gas flow simulation with 800,000 computational cells using 64 processors maintained about 70%.
3. In the silane/hydrogen gas discharge in a low-pressure PECVD chamber driven by a RF power source (27.12 MHz), the conduction is dominated.
4. Helium micro-cell plasma is simulation coupling with a parallelized fluid modeling code, and a reverse flow field is found with considering the plasma momentum source.
5. A non-equilibrium atmospheric-pressure helium dielectric barrier discharge driven by a realistic distorted-sinusoidal voltage power source (25 kHz) is investigated by using the developed gas flow model coupling with a parallelized fluid modeling code. Electrode lengths, jet-to-substrate spacing rates, and gas flow

rates have a remarkable influence on the flow and heat transfer characteristics.

## 6.2 Recommendations for Future Work

There are several recommendations for further work:

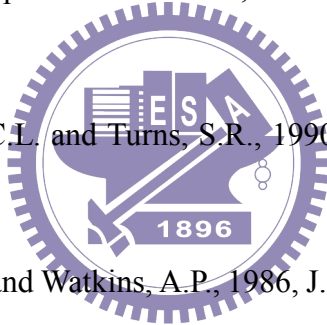
1. To further reduce the computational time in large-scale gas flow problem.
2. To solve the gas flow model in the curvilinear coordinate frame for complex geometry problem.
3. To involve the turbulent model for complex flows.
4. To add chemical reaction and electrochemistry module
5. To extend the gas flow model into three-dimensional version for realistic applications



## References

- [1] Bird, R. B., Stewart, E. E., Lightfoot, E. N., "Transport Phenomena", Wiley; 2nd edition, 2002.
- [2] Briley, W.R., and McDonald, H., "On the Structure and Use of Linearized Block Implicit Scheme." J. Comput. Phys. 34, pp.54, 1980.
- [3] Borgnakke, C. and Sonntag, R. E., "Fundamentals of Thermodynamics", Wiley; 7th edition, 2008.
- [4] Cercignani, C., The Boltzmann Equation and its Applications, Springer, New York, 1988.
- [5] Chen, Y.S., "An Unstructured Finite Volume Method for Viscous Flow Computations", 7th International Conference on Finite Element Methods in Flow Problems, Feb. 3-7,1989, University of Alabama in Huntsville, Huntsville, Alabama.
- [6] Choi, Y.H. and Merkle, C.L., 1991, AIAA Technical Paper 91-1652.
- [7] Choi, Y.H. and Merkle, C.L., 1993, Journal of Computational Physics, Vol. 105, pp. 207-223.
- [8] Chorin, A.J., 1967, Journal of Computational Physics, Vol. 2, pp. 12-26
- [9] Chorin, A.J., 1968, Mathematics of Computation, Vol. 22, No. 104, pp. 745-762.
- [10] Demirdzic, I., Lilek, Z. and Peric, M., 1993, Int. J. Num. Met. Fluids, Vol. 17, pp. 1029-1050
- [11] Ghia, U., Ghia, K.N. and Shin, T.C., "High Re Solutions for Incompressible Flow Using the Navier-Stokes Equations and a Multigrid Method", J. Comp. Phys. n.48, pp 387-411, 1982.
- [12] Gosman, A.D., Pan, W.M., Runchal, A.K., Spalding, D.B., and Wolfshein, M., "Heat and Mass Transfer in Recirculating Flow." Academic Press, 1980

- [13] Harlow, F.H. and Welch, J.E., “Numerical Calculation of Time-dependent Viscous Incompressible Flow of Fluid with Free Surface.” *Phys. Fluids* 8, 2182, 1965.
- [14] Harlow, F.H. and Amsden, A.A., “The SMAC Method: A Numerical Technique for Calculating Incompressible Fluid Flows.” Los Alamos Scientific Laboratory Rept, LA-4370, 1970.
- [15] Harlow, F.H. and Amsden, A.A., 1971, *J. Computational Physics*, Vol. 8, No. 2, pp. 197-213.
- [16] Hou, Y. and Mahesh, K., 2005, *Journal of Computational Physics*, Vol. 205, pp. 205-221.
- [17] Hung, C.T., “Development of a Parallelized Fluid Modeling Code and Its Applications in Low-temperature Plasmas”, Ph.D. thesis, National Chiao Tung University, Taiwan, 2010.
- [18] Hosangadi, A., Merkle, C.L. and Turns, S.R., 1990, *AIAA J.*, Vol. 28, No. 8, pp. 1473-1480.
- [19] Issa, R.I., Gosman, A.D. and Watkins, A.P., 1986, *J. Comp. Physics*, Vol. 62, No. 1, pp. 66-82.
- [20] Issa, R.I. and Javareshkian, M.H., 1998, *AIAA Journal*, Vol. 36, No. 9, pp. 1652-1657.
- [21] Jameson, A., Schmidt, W. and Turkel, E., “Numerical Solutions to the Euler Equations by Finite Volume Methods Using Runge\_Kutta Time Stepping,” *AIAA* pp.81, 1981.
- [22] Karki, K.C. and Patankar, S.V., “Pressure Based Calculation Procedure for Viscous Flows at all Speeds in Arbitrary Configurations,” *AIAA J.*, Vol. 27, pp. 1167-1174, 1989.





- [23] Lin, K.M., “Development of Parallel Hybrid Simulation of Gas Discharge and Gas Flow and Its Application in the Modeling of Atmospheric-Pressure Helium Dielectric Barrier Discharge Jet Considering Impurities”, Ph.D. thesis, National Chiao Tung University, Taiwan, 2012.
- [24] Merkle, C.L. and Athavale, M., 1987, AIAA Technical Paper, 87-1137.
- [25] Merkle, C.L. and Choi, Y.H., 1988, Int. J. Num. Met. Eng., Vol. 25, pp. 293-311.
- [26] Patankar, S.V. and Spalding, D.B., 1972, Int. J. Heat & Mass Transfer, Vol. 15, No. 1787-1806
- [27] Rahman, Md. M., Alim, M. A., Saha, S. and Chowdhury, M. K., “A Numerical study of mixed convection in a square cavity with q heat conducting square cylinder at different locations”, J. Mech. Eng, 39, pp.78, 2008.
- [28] Rhie, C.M., 1989, AIAA Journal, Vol. 27, No. 8, pp. 1017-1018.
- [29] Rossow, C.C., 2003, Journal of Computational Physics, Vol. 185, No. 2, pp. 375-398
- [30] Sahu, J., Nietubitz, C.J. and Steger, J.L., “Navier-Stokes Computations of Projectile Base Flow with and without Base injection,” AIAA J., Vol. 23, pp. 1348-1355, 1985.
- [31] Shang, H.M. and Chen, Y.S., “Unstructured Adaptive Grid Method for Reacting Flow Computation”, AIAA Paper 97-3183, July 1997.
- [32] Shang, H.M., Chen, Y.S., Liaw, P. and Chen, C.P., “A Hybrid Unstructured Grid Method for Fluid Flow Computation”, Numerical Developments in CFD Symposium of the Joint ASME/JSME Fluids Engineering Conference, August 13-18, 1995, Hilton Head Island, SC.

- [33] Shang, H.M., Chen, Y.S., Liaw, P., Shih, M.S. and Wang, T.S., “Numerical Modeling of Spray Combustion with an Unstructured Grid Method”, AIAA Paper 95-2781, 1995.
- [34] Shang, H.M., Shih, M.H., Chen, Y.S., and Liaw, P., “Flow Calculation on Unstructured Grids with a Pressure-Based Method”, Proceedings of 6th International Symposium on Computational Fluid Dynamics, Sep. 4-8, 1995, Lake Tahoe, NV.
- [35] Shterev, K.S., Stefanov, S.K., “Pressure based finite volume method for calculation of compressible viscous gas flows”, J. Comp. Phys. n.229, pp 461-480, 2010.
- [36] Shuen, J.S., Chen, K.H. and Choi, Y.H., 1992, AIAA Technical Paper, 92-3639
- [37] Shuen, J.S., Chen, K.H. and Choi, Y.H., 1993, J. Comp. Physics, Vol. 106, pp. 306-318.
- [38] Shyy, W. and Chen, M.H., 1992, AIAA Journal, Vol. 30, No. 11, pp. 2660-0000
- [39] Turkel, E., 1987, Journal of Computational Physics, Vol. 72, No. 2, pp. 277-298.
- [40] Zhang, S.J., Liu, J., Chen, Y.S. and Wang, T.S., “Adaptation for Hybrid Unstructured Grid with Hanging Node Method,” AIAA Paper 2001-2657, 2001

Table 1. Lennard-Jones potential parameters. [Bird et al., 2002]

Substance	Molecular weight ( $M$ )	$\sigma$ (Å)	$\varepsilon / k_B$ ( $K$ )
He	4.003	2.576	38
Ar	39.948	3.432	122.4
N <sub>2</sub>	28.013	3.667	99.8
O <sub>2</sub>	31.999	3.433	113
Air	28.964	3.617	97

Table 2. Constant-pressure specific heats and heat of formation of various ideal gases. [Borgnakke & Sonntag, 2008]

Gas	$\Delta h_f^0$ (kJ/mol) <sup>†</sup>	$C_{p0} = C_0 + C_1T + C_2T^2 + C_3T^3$ (J/kg·K)			
		$C_0$	$C_1$	$C_2$	$C_3$
He	0	5193	0	0	0
Ar	0	520	0	0	0
N <sub>2</sub>	0	1110	-4.8E-04	9.6E-07	-4.2E-10
O <sub>2</sub>	0	880	-1.0E-07	5.4E-07	-3.3E-10
Air	0	1050	-3.65E-04	8.5E-07	-3.9E-10
H <sub>2</sub>	0	13460	4.6E-03	-6.85E-06	3.79E-09
SiH <sub>4</sub>	34.3	1308	-	-	-

<sup>†</sup> Chase, M. W. et al., JANAF Thermochemical Tables, Third Edition, J. Phys. Chem. Ref. Data, Vol. 14, Suppl.1, 1985

Table 3. Scaling parameters used in gas flow model.

Scaling Parameter	Description	Unit
$L_\infty$	Characteristic length	$m$
$U_\infty$	Characteristic speed	$m/s$
$\rho_\infty$	Characteristic density	$kg/m^3$
$T_\infty$	Characteristic temperature	$K$
$\mu_\infty$	Characteristic viscosity	$kg/m \cdot s$
$k_\infty$	Characteristic conductivity	$W/m \cdot s$
$R_\infty$	Characteristic gas constant	$J/mol \cdot K$
$C_{p,\infty}$	Characteristic specific heat capacity	$J/kg \cdot K$

Table 4. Substance parameters in helium micro-cell plasma.

	Material	$\rho [kg/m^3]$	$C_p [J/kg \cdot K]$	$k [W/m \cdot K]$
Electrode	Al	2750	900	228
Insulator	SiO <sub>2</sub>	2200	703	1.4
Plasma	He	0.16	5194	0.15

Table 5. Test cases and results of a helium dielectric barrier discharge atmospheric-pressure plasma jet for various  $H/d$  for  $d=1$  mm, and gas flow rate of 20slm.

Case	$H/d$	$N_x$	$N_y$	$P_{stag}$ [Torr]	$Nu_{stag}$
a	5	140	160	760.033	3.5
b	7.5	150	160	760.027	2.8
c	10	160	160	750.023	2.4
d	12.5	170	160	760.02	2.1
e	15	180	160	760.018	1.8

Table 6. The approximated Reynolds numbers and bulk temperatures for various gas flow rates.

Gas flow rate [slm]	10	15	20	25	30
Re	30	45	60	75	90
$T_{bulk}$ (K)	346.3	330.9	323.2	318.5	315.4

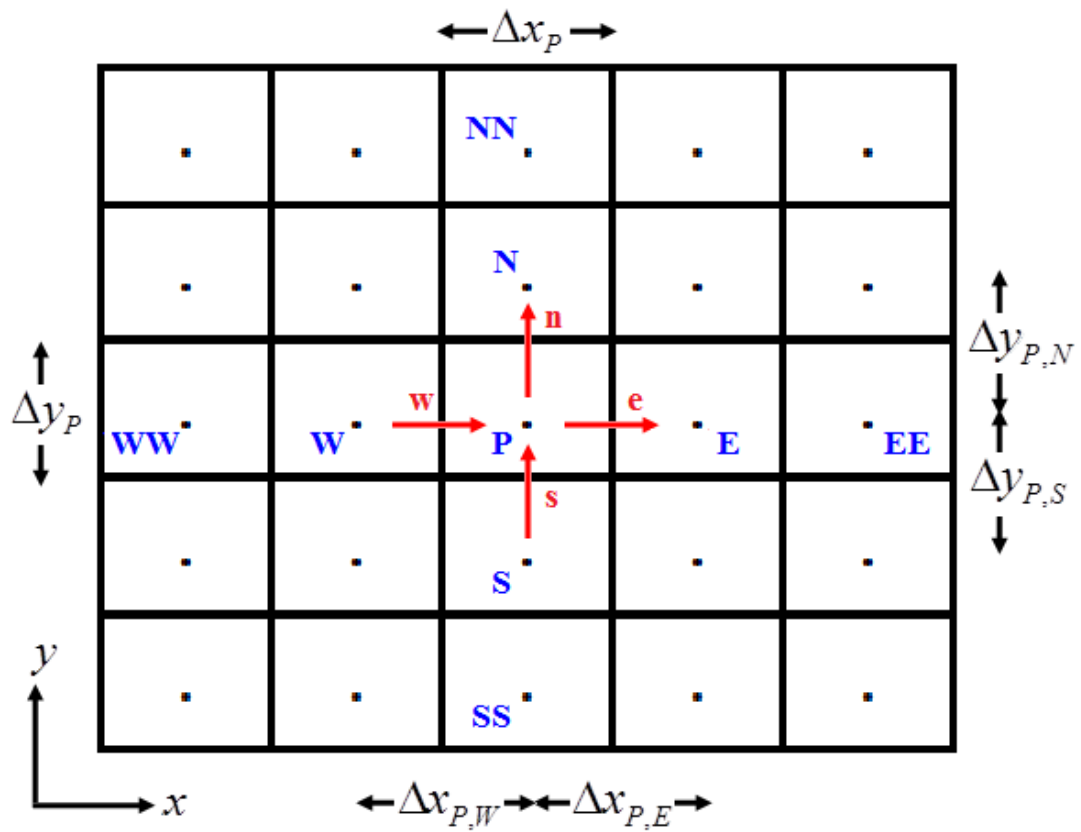


Figure 2-1: Two-dimensional control volume.

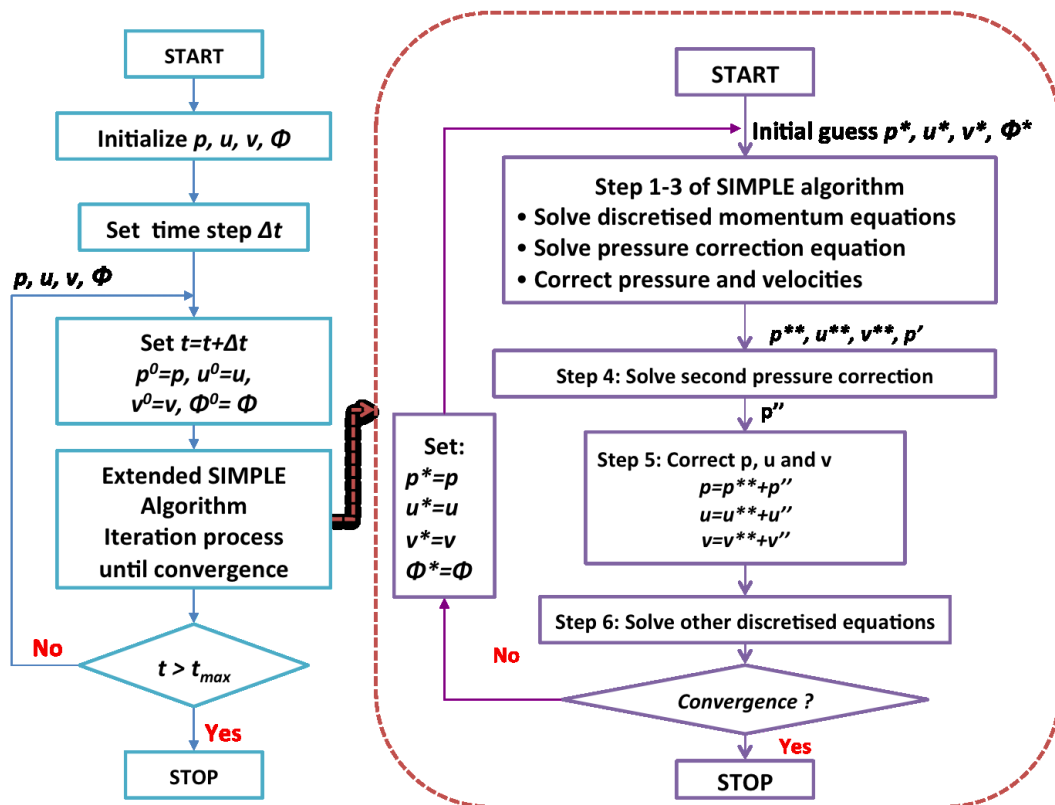


Figure 2-2: Flowchart of the extended SIMPLE algorithm.

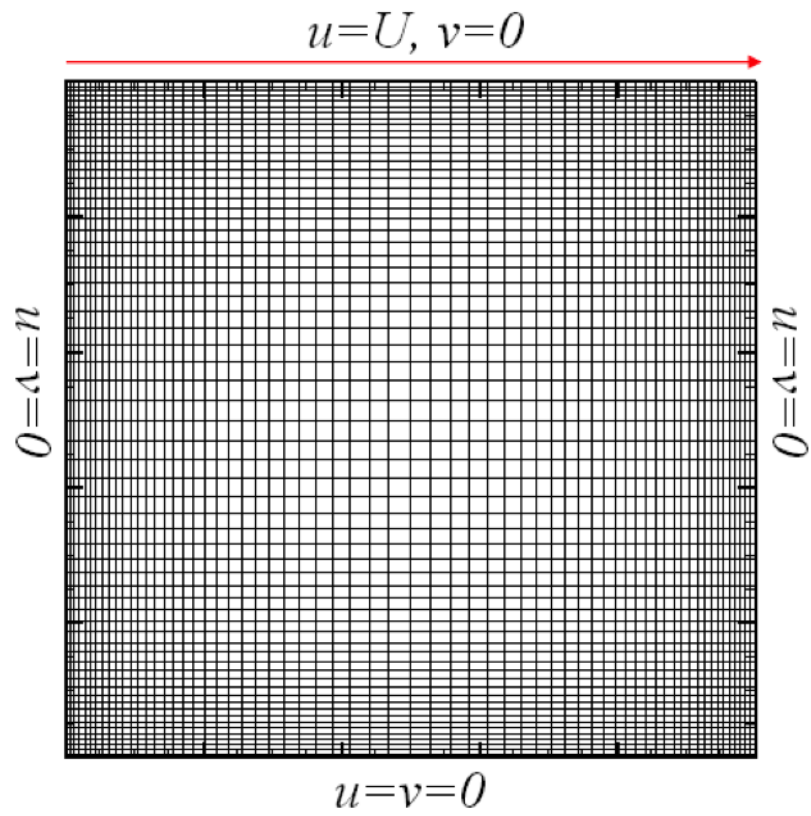


Figure 3-1: Schematic of the computational grid a in two-dimensional lid-driven cavity.



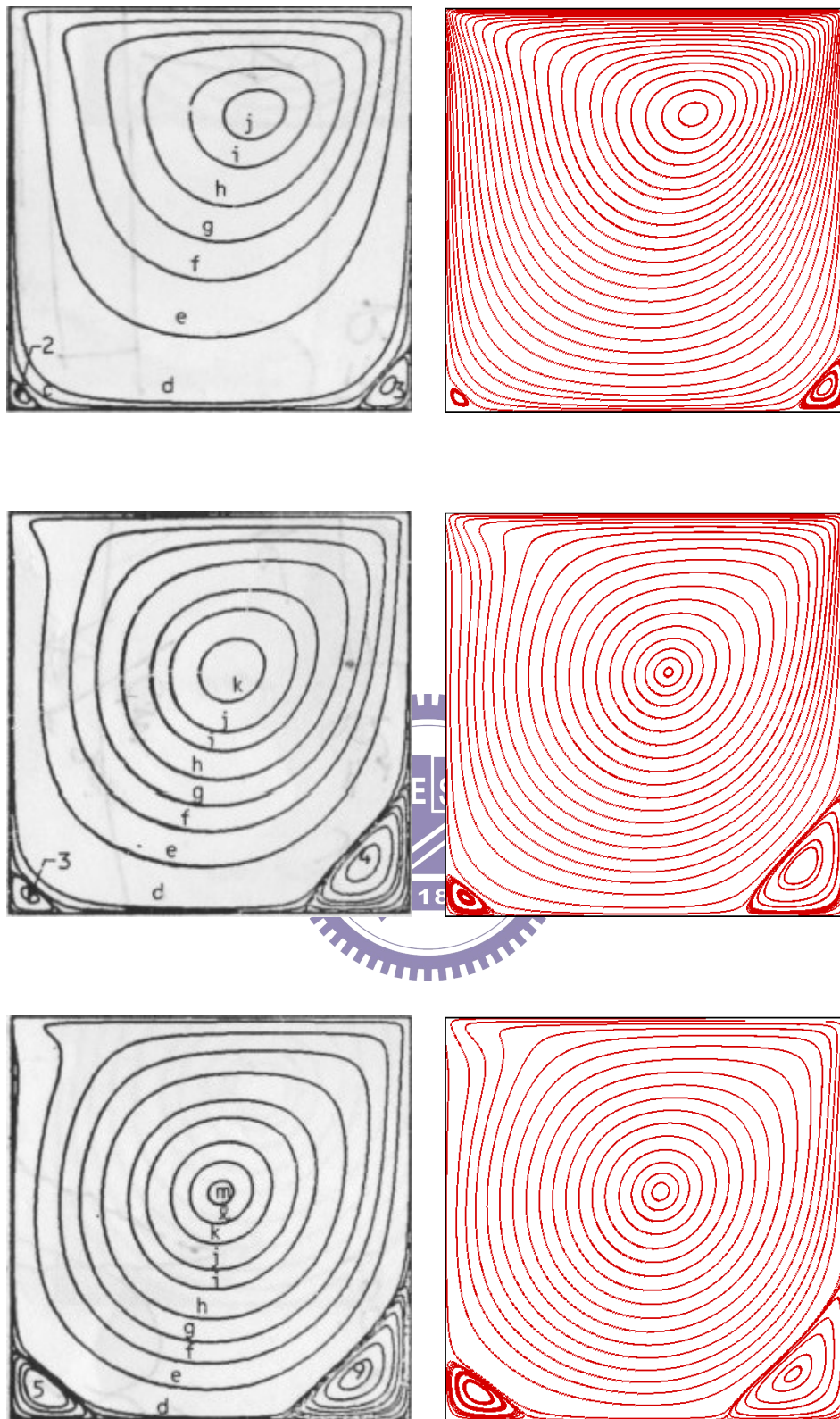


Figure 3-2: Streamlines for driven cavity flow with Reynolds numbers of 100, 400 and 1,000 (top to bottom). Note: Ghia et al. [1982] (left); present (right).

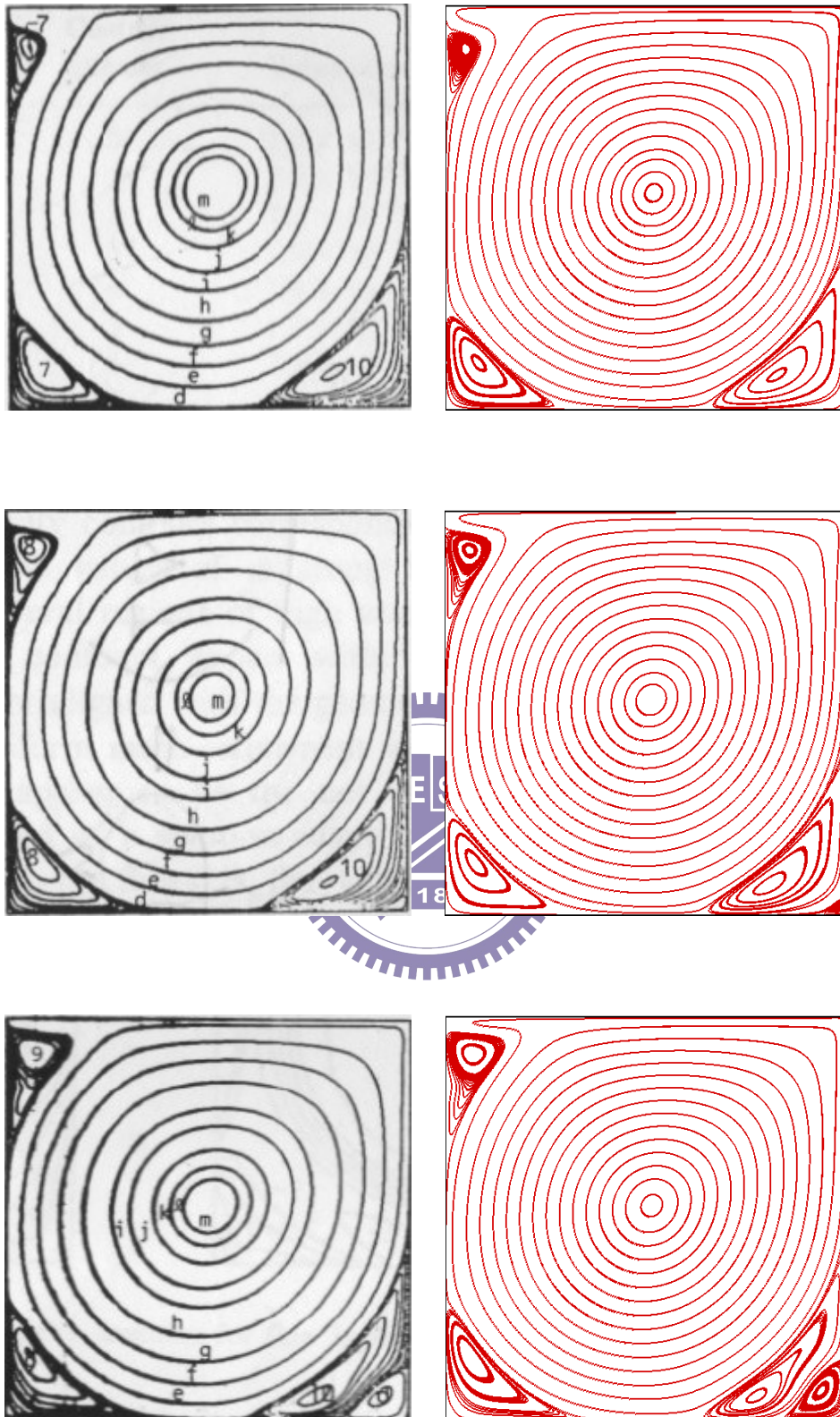


Figure 3-3: Streamlines for driven cavity flow with Reynolds numbers of 3200, 5000, and 10000 (top to bottom). Note: Ghia et al. [1982] (left); present (right).

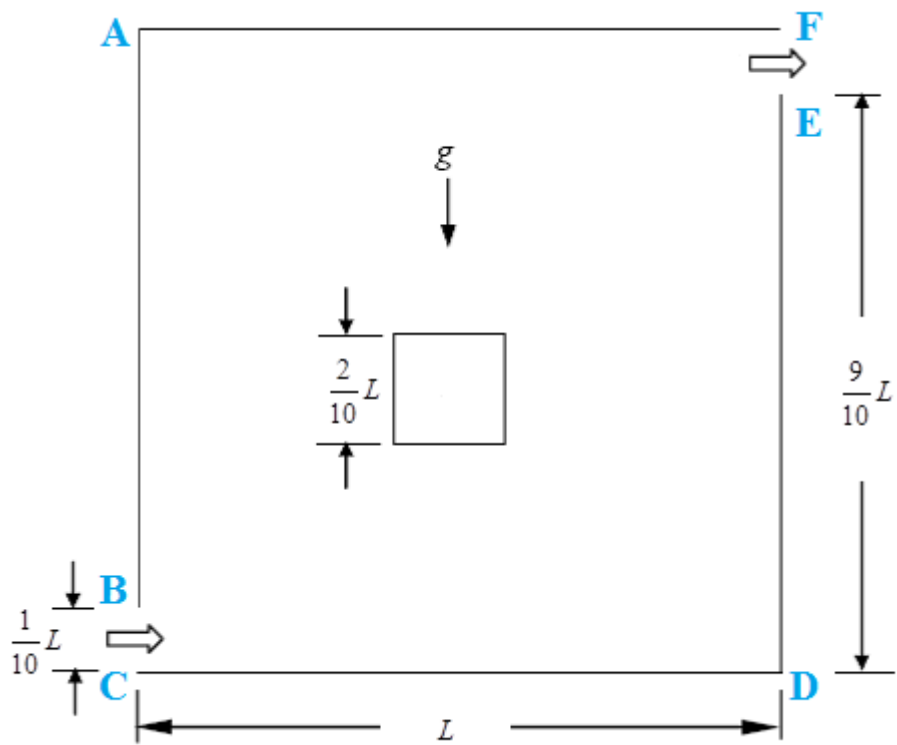


Figure 3-4: Schematic of the flow in a square cavity with a square block.

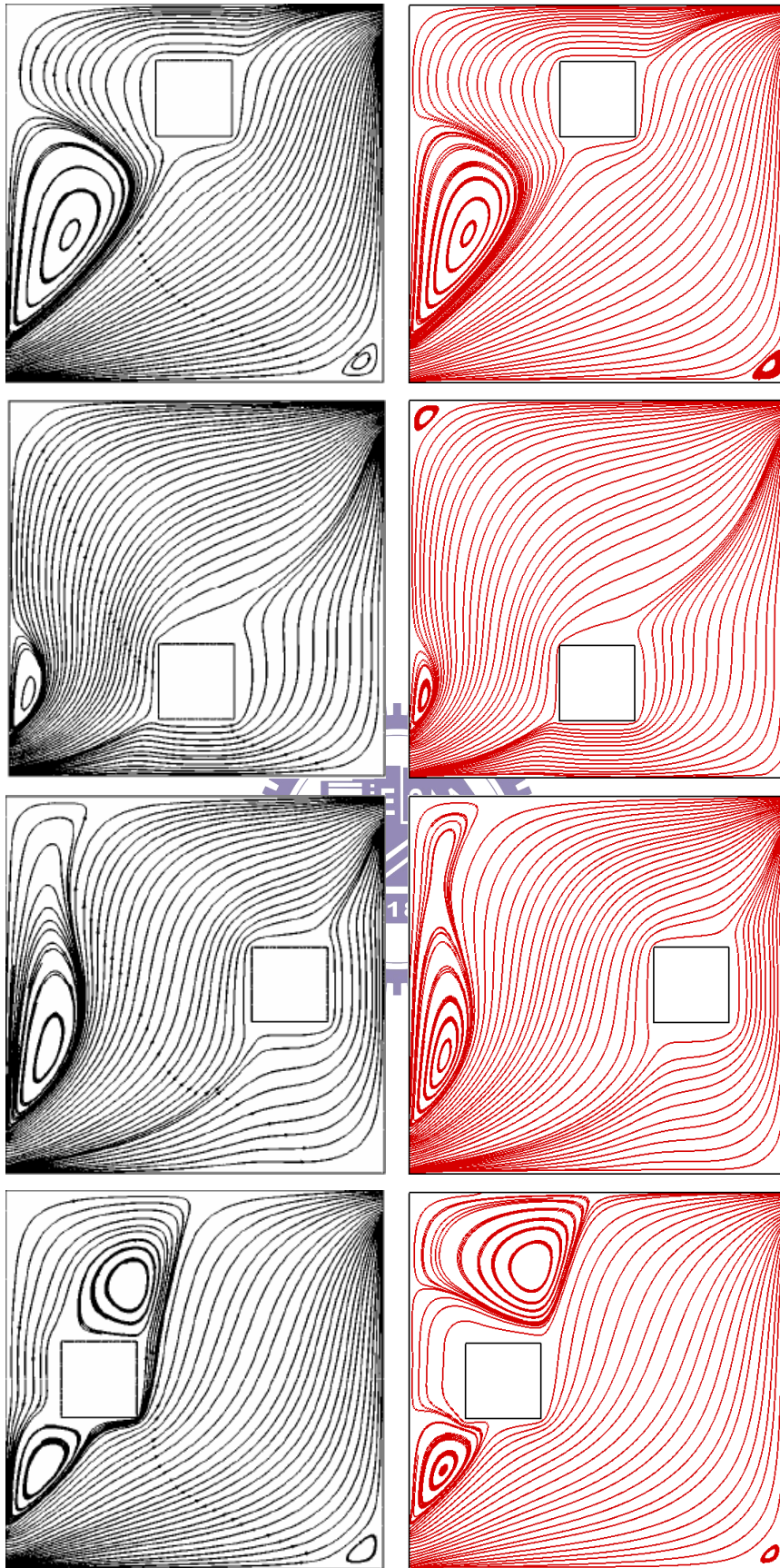


Figure 3-5: Streamlines for Different Locations of Cylinder at  $Ri = 0$ . Note: Rahman et al. [2008] (left); present (right).

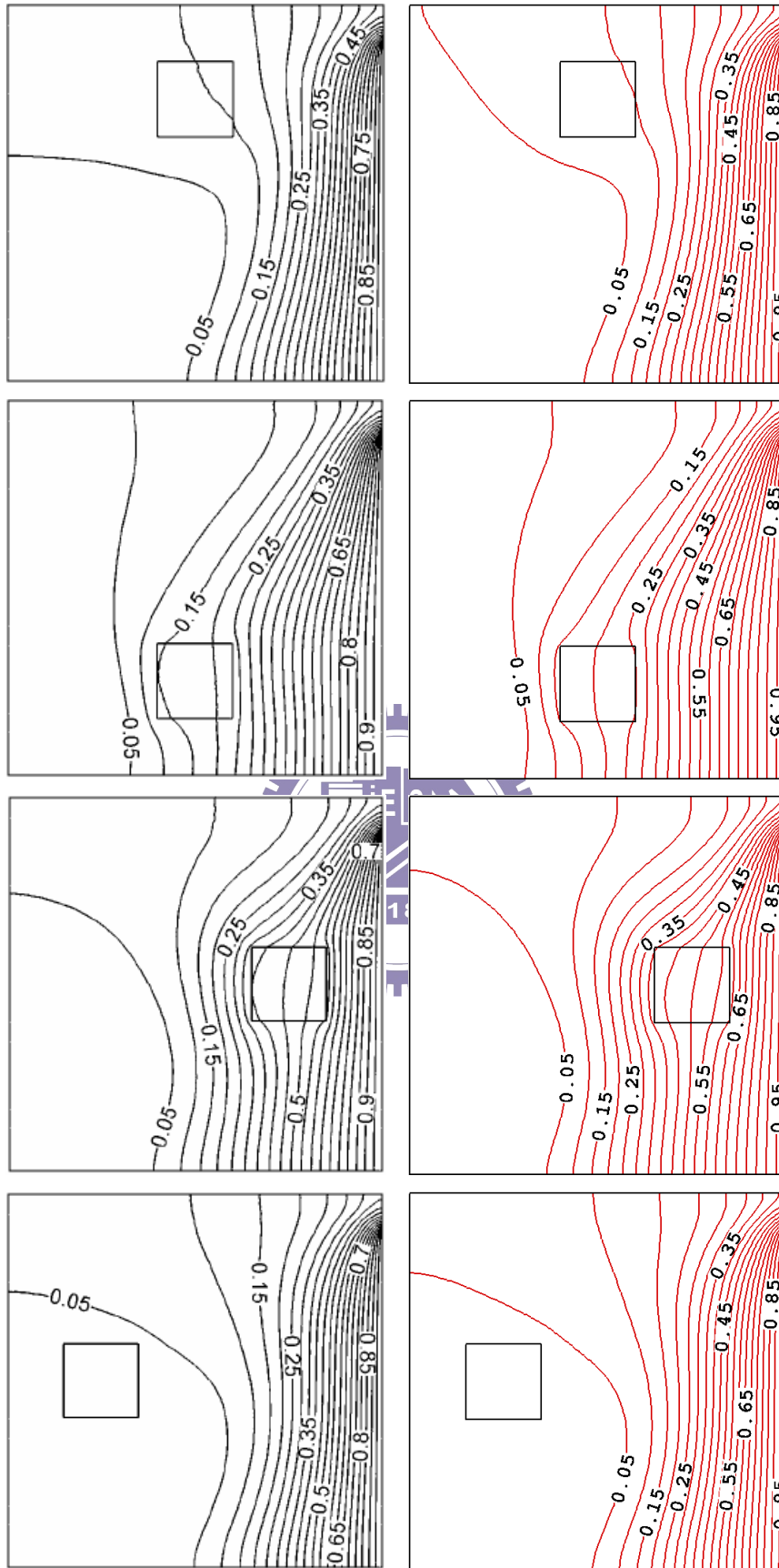


Figure 3-6: Isotherms for Different Locations of Cylinder at  $Ri = 0$ . Note: Rahman et al. [2008] (left); present (right).

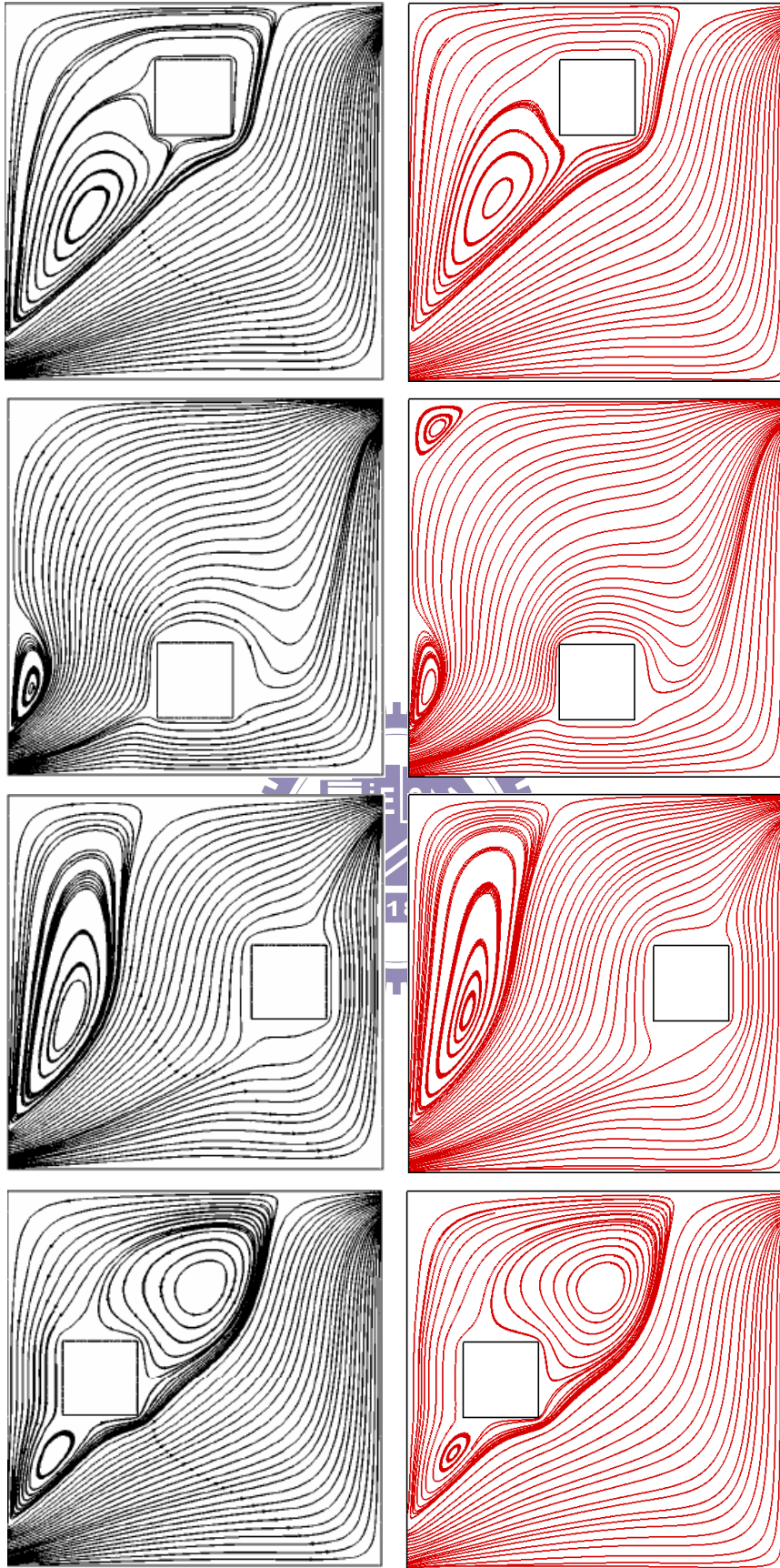


Figure 3-7: Streamlines for Different Locations of Cylinder at  $Ri = 1$ . Note: Rahman et al. [2008] (left); present (right).

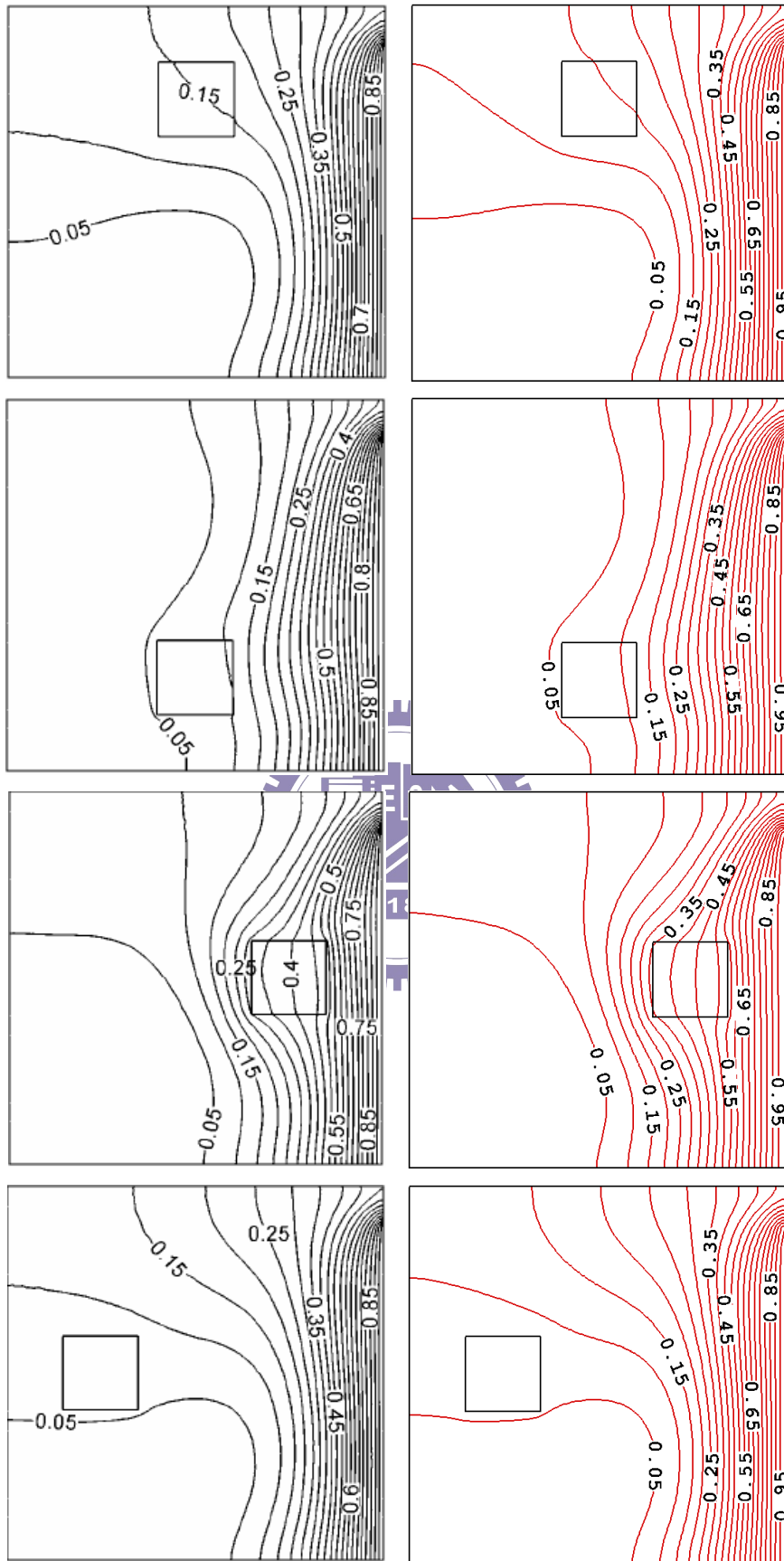


Figure 3-8: Isotherms for Different Locations of Cylinder at  $Ri = 1$ . Note: Rahman et al. [2008] (left); present (right).

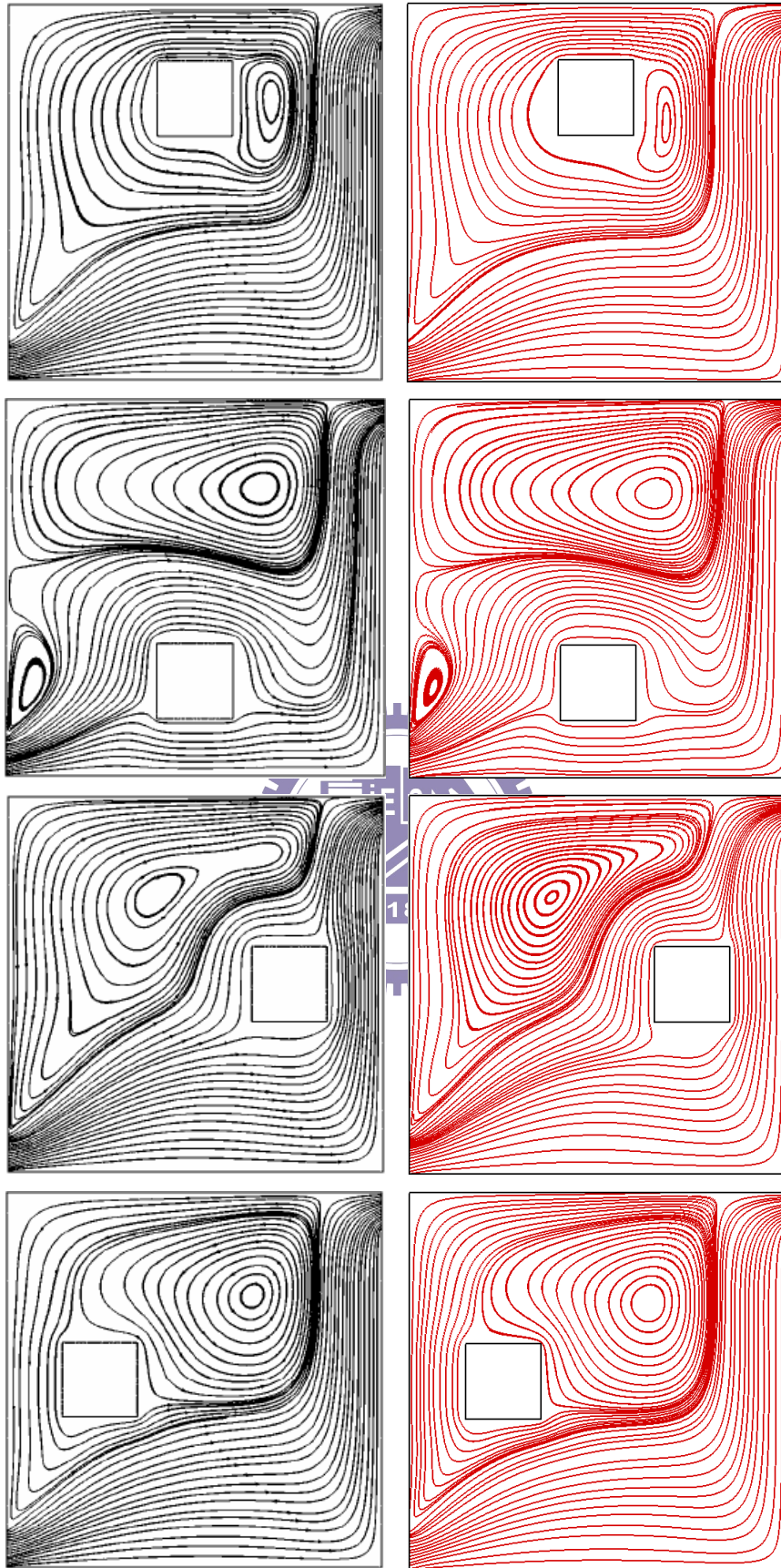


Figure 3-9: Streamlines for Different Locations of Cylinder at  $Ri = 5$ . Note: Rahman et al. [2008] (left); present (right).



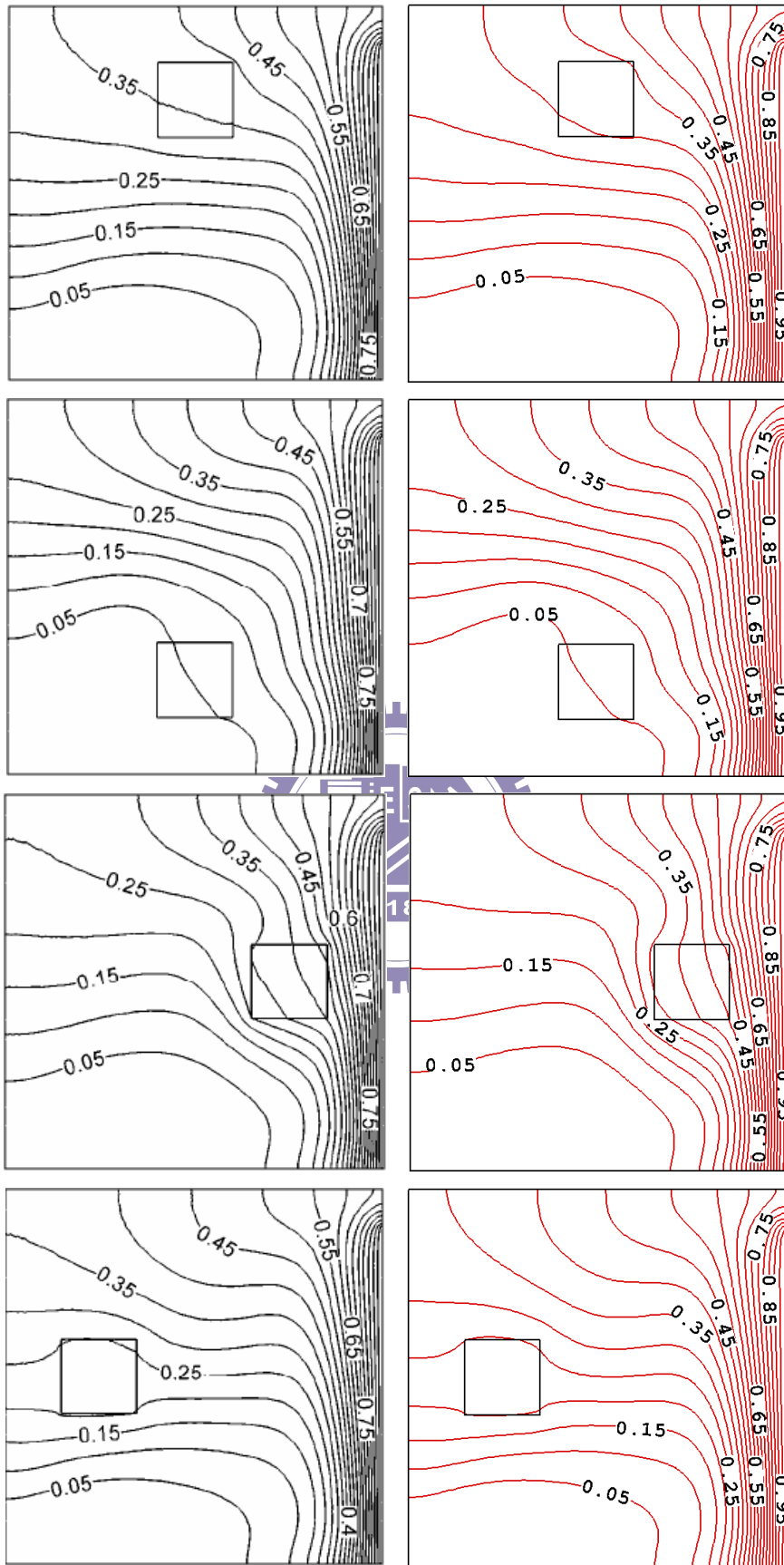


Figure 3-10: Isotherms for Different Locations of Cylinder at  $Ri = 5$ . Note: Rahman et al. [2008] (left); present (right).

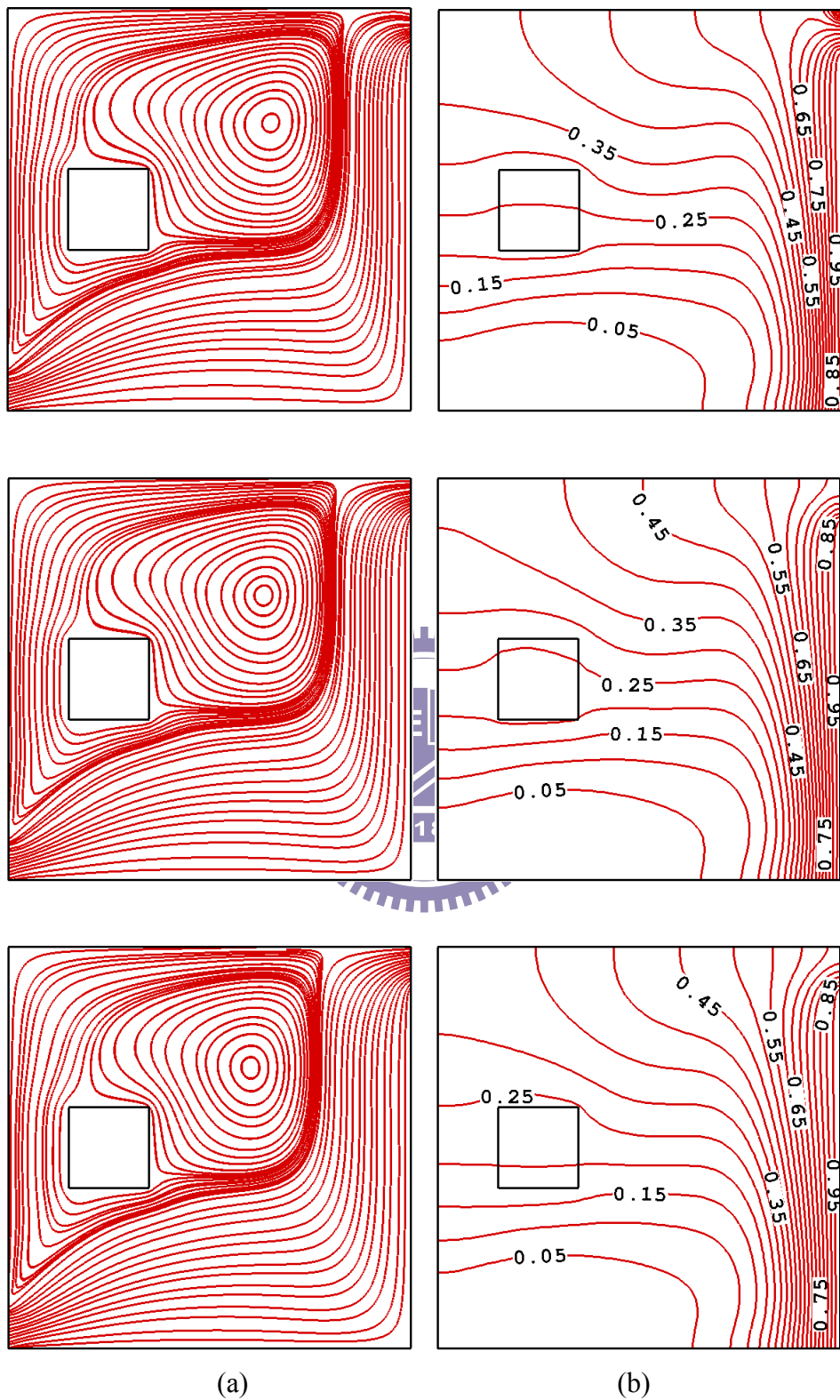


Figure 3-11: Distributions of (a) streamlines and (b) isotherms at  $Ri = 5$ ,  $Lx=0.25$  and  $Ly=0.5$ . Note:  $\Delta T=50$  K (top), 100 K (middle), and 200 K (bottom).

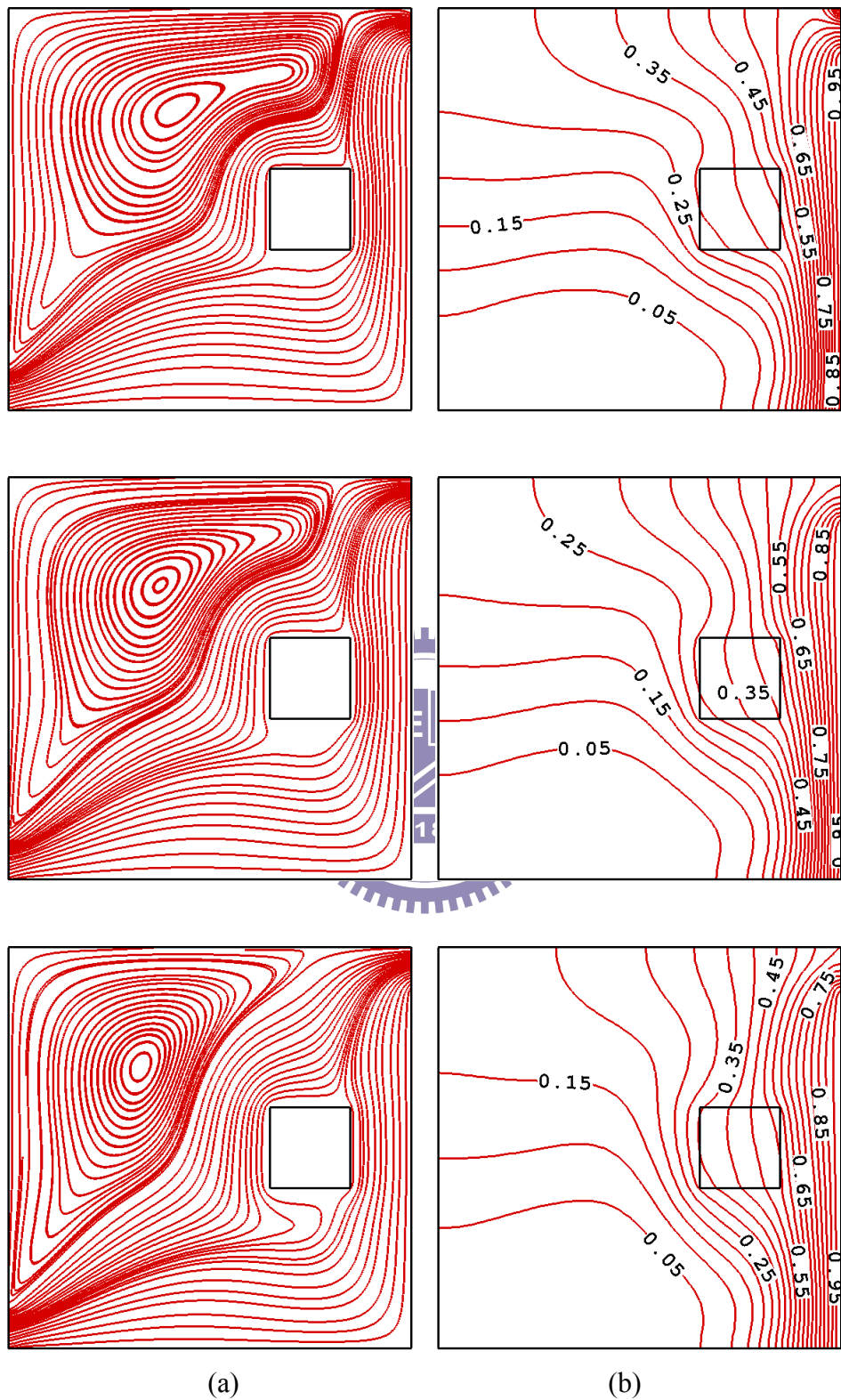


Figure 3-12: Distributions of (a) streamlines and (b) isotherms at  $Ri = 5$ ,  $Lx=0.75$  and  $Ly=0.5$ . Note:  $\Delta T=50$  K (top), 100 K (middle), and 200 K (bottom).

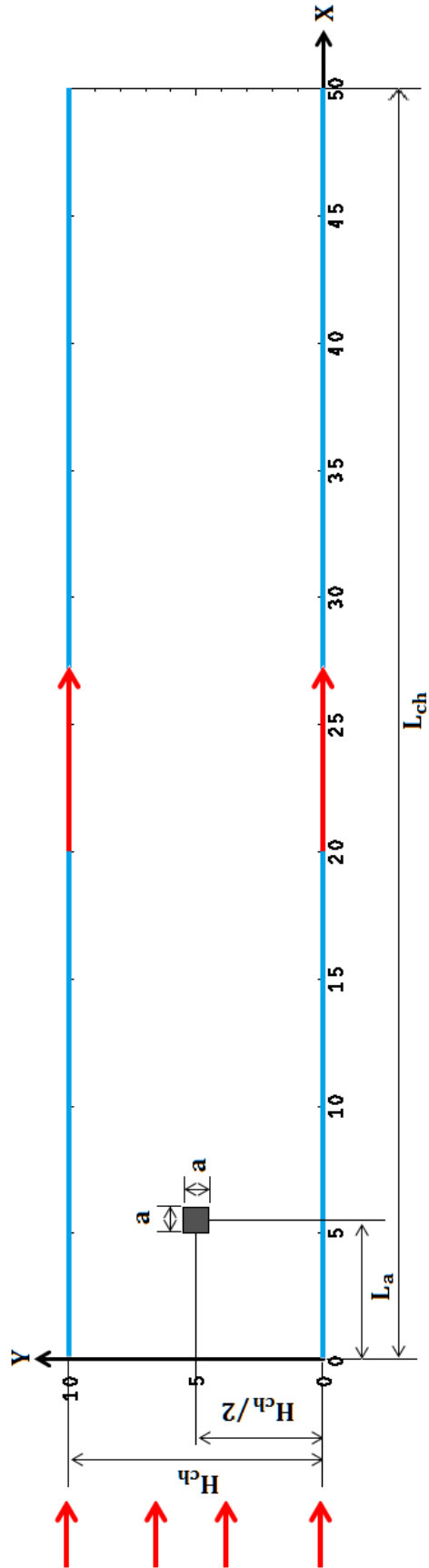


Figure 3-13: Schematic of the two-dimensional micro-scale channel flow

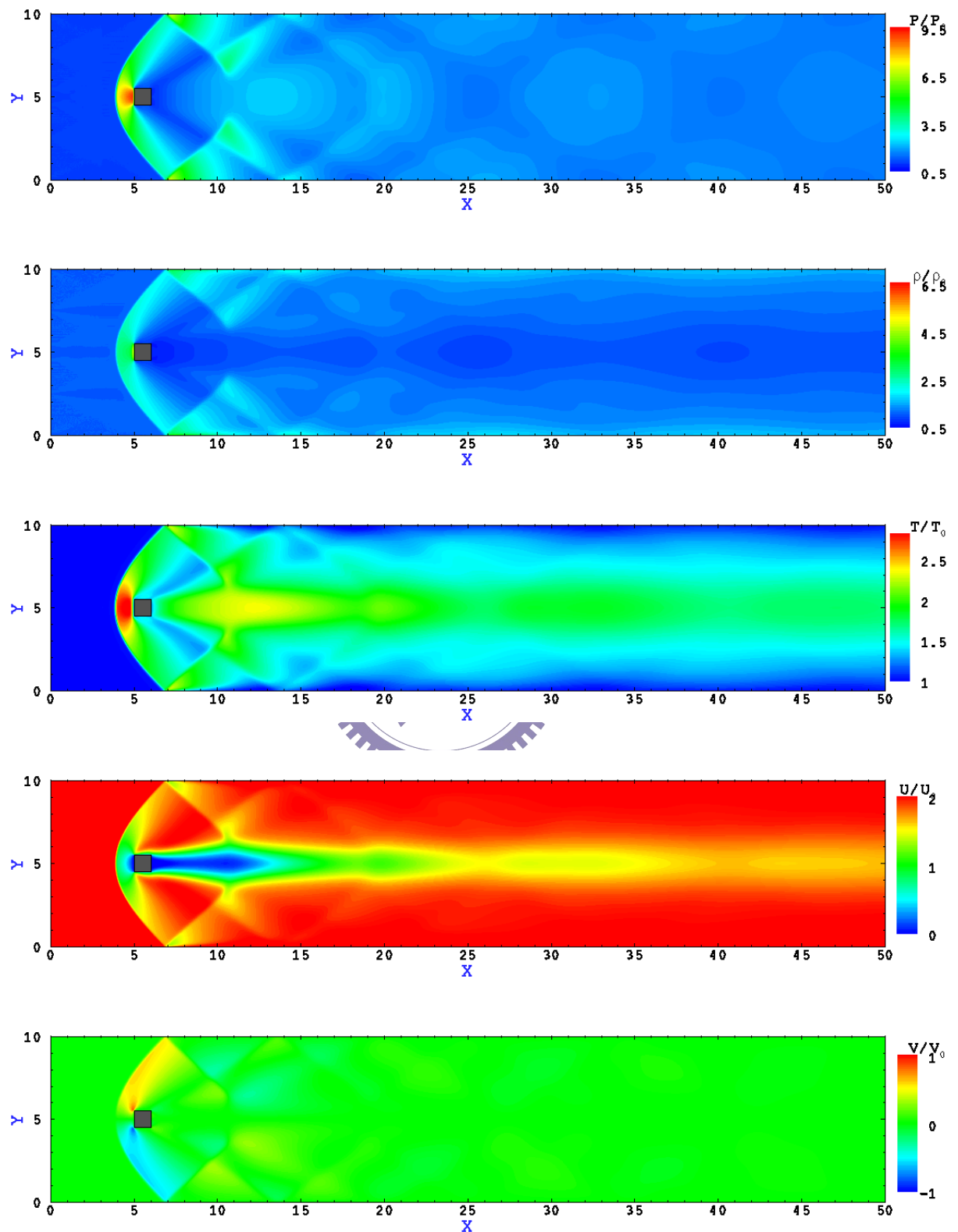


Figure 3-14: Normalization Distributions of Pressure, Density, Temperature, Velocity in x- and y-direction in the channel at Ma=2.4261 and Kn=0.05.

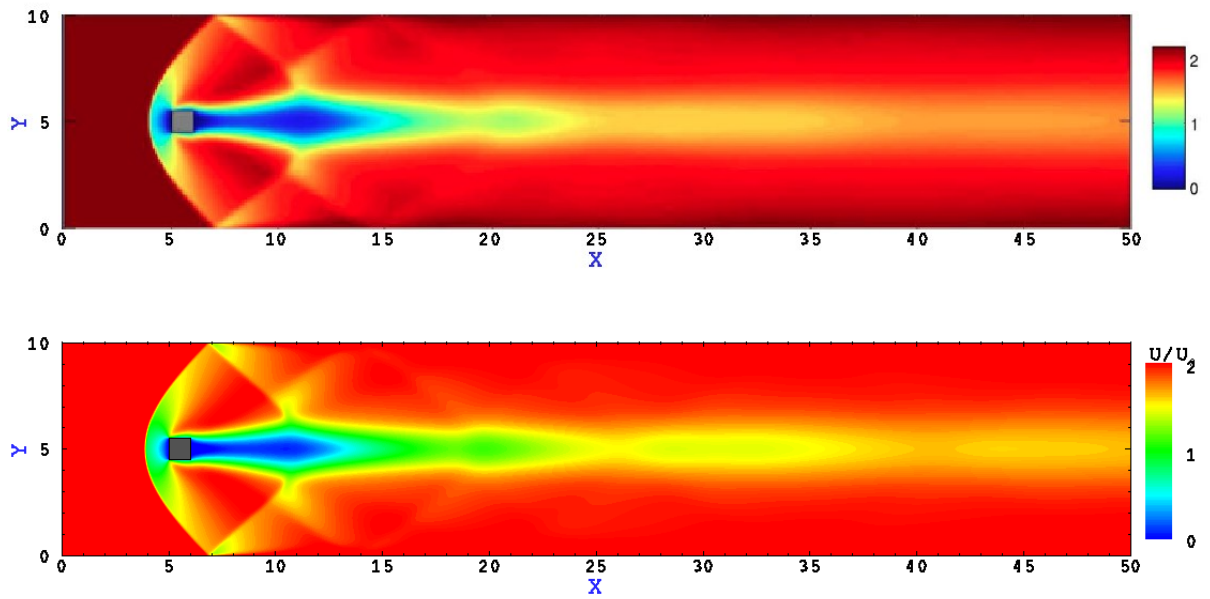


Figure 3-15: Normalization Distribution of horizontal velocity. Note: Shterev and

Stefanov [2010] (upper); present (lower).

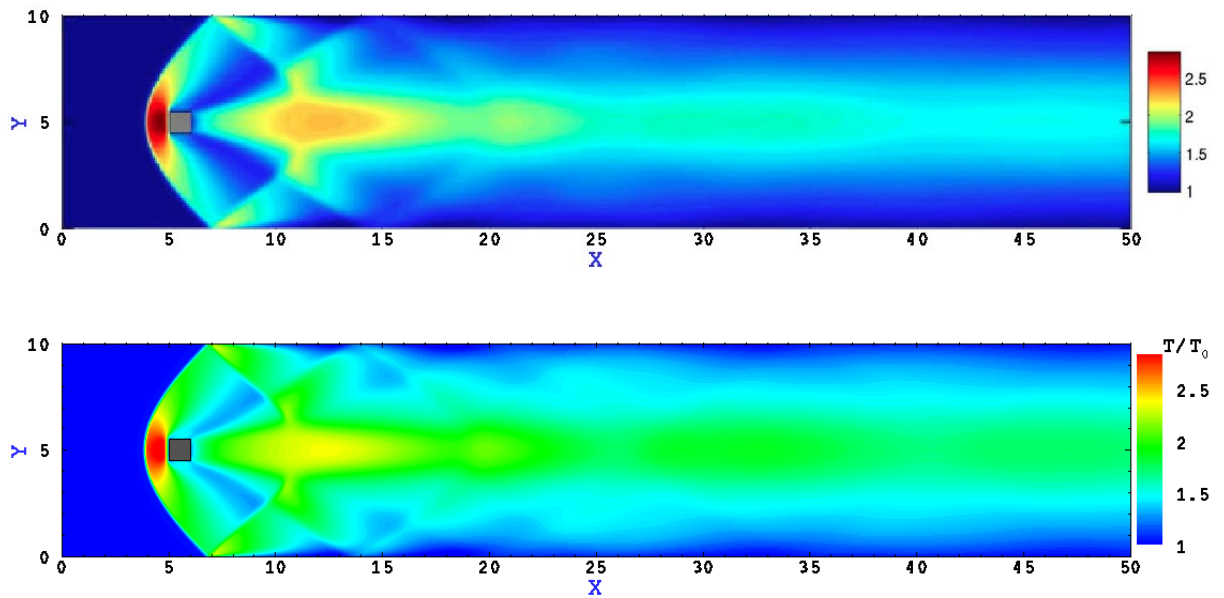
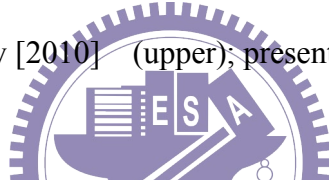


Figure 3-16: Normalization Distribution of temperature. Note: Shterev and Stefanov

[2010] (upper); present (lower).

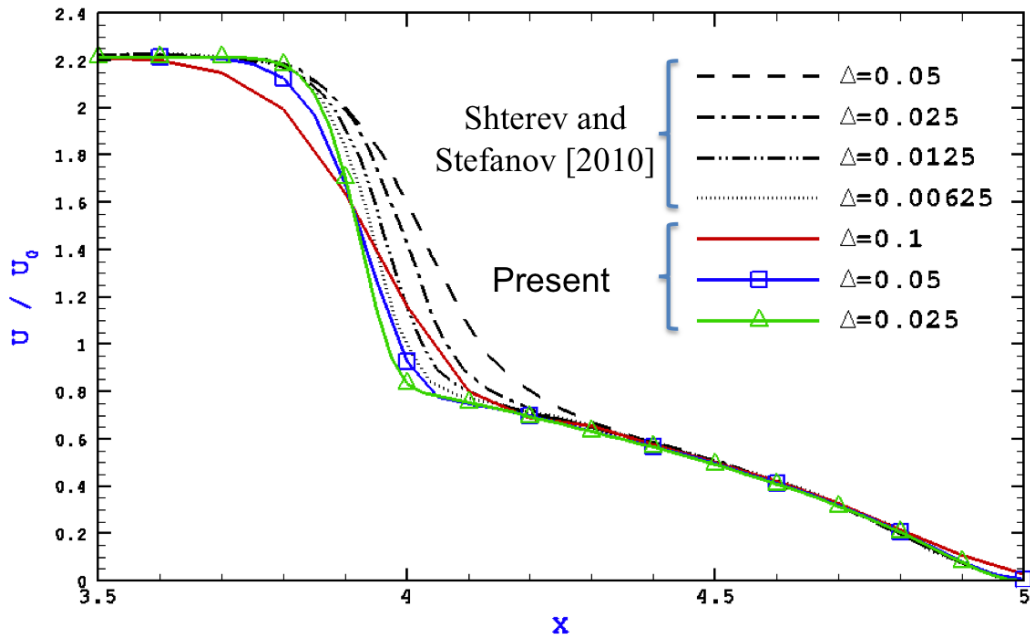


Figure 3-17: Profiles of the horizontal velocity along the center line of the channel ( $y=H_{ch}/2$ ) for different spatial steps in front of the square.

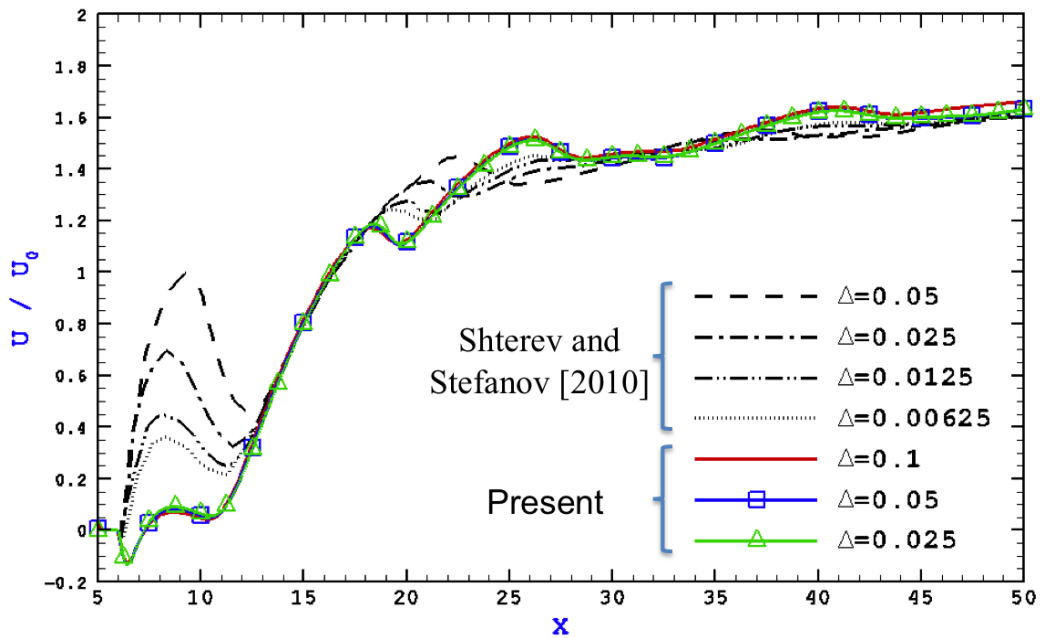


Figure 3-18: Profiles of the horizontal velocity along the center line of the channel ( $y=H_{ch}/2$ ) for different spatial steps behind of the square.

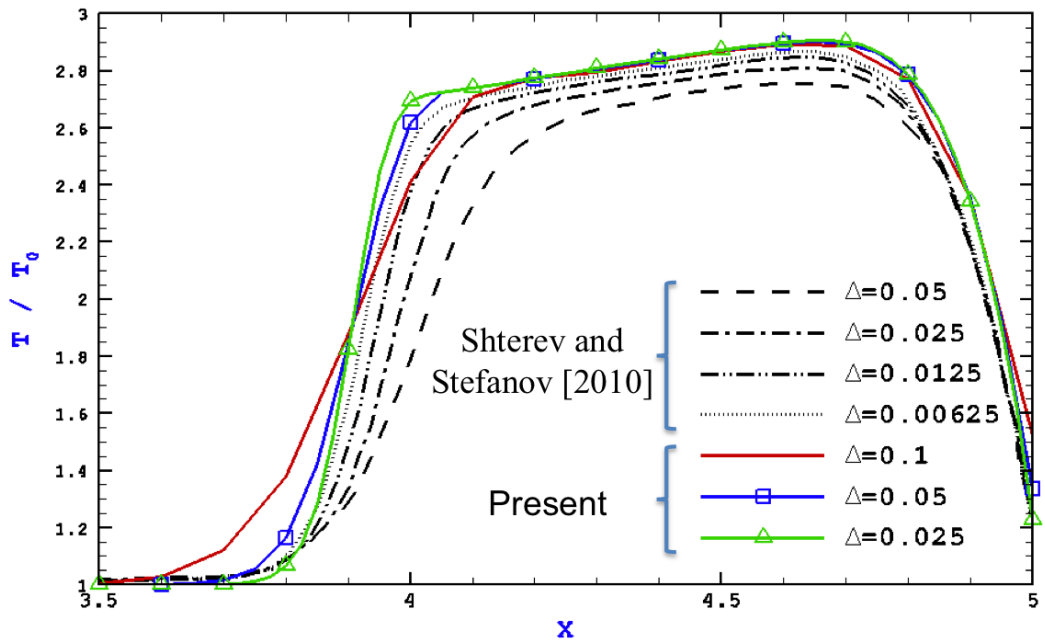


Figure 3-19: Temperature profiles along the center line of the channel ( $y=H_{ch}/2$ ) for different spatial steps in front of the square.

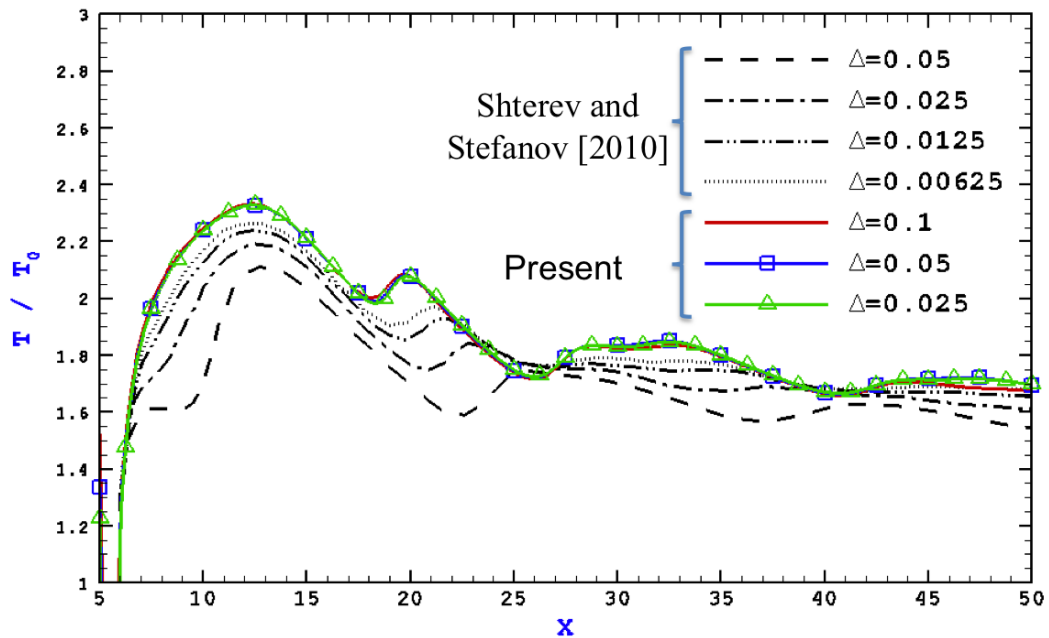


Figure 3-20: Temperature profiles along the center line of the channel ( $y=H_{ch}/2$ ) for different spatial steps behind of the square.



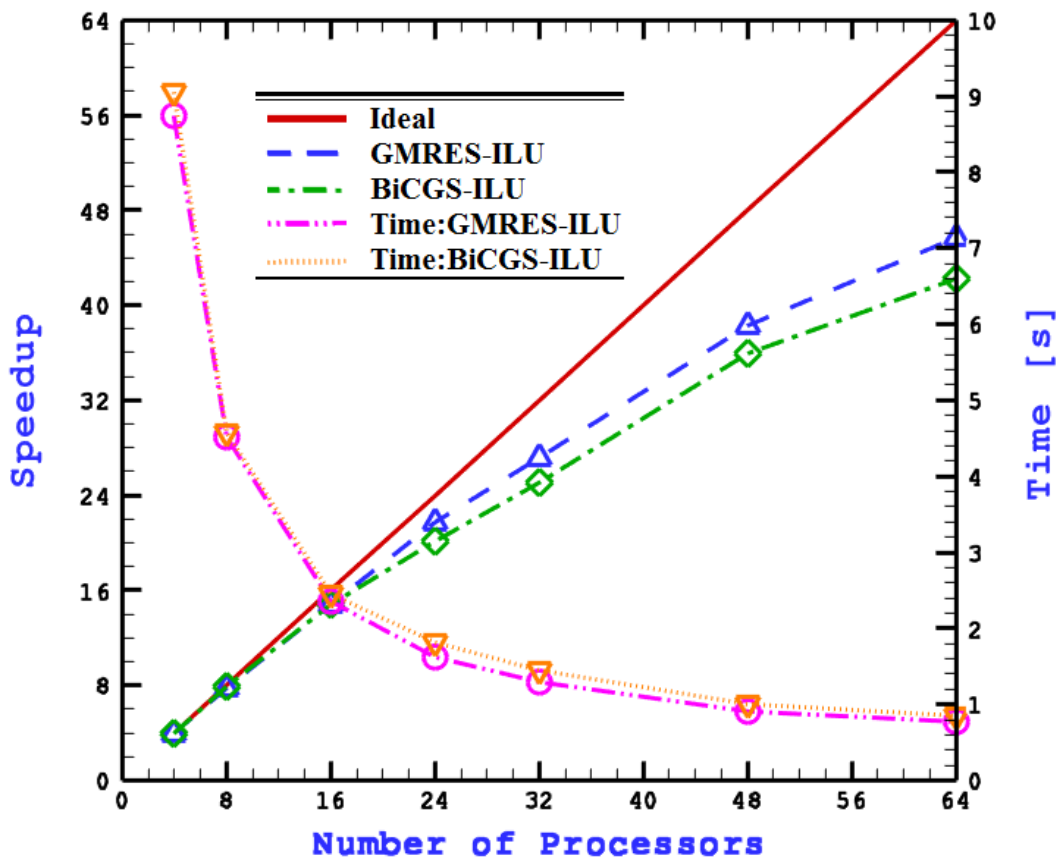


Figure 3-21: Parallel Performance and runtime per time step of a 2D micro-scale supersonic flow with 2000x400 computational cells.

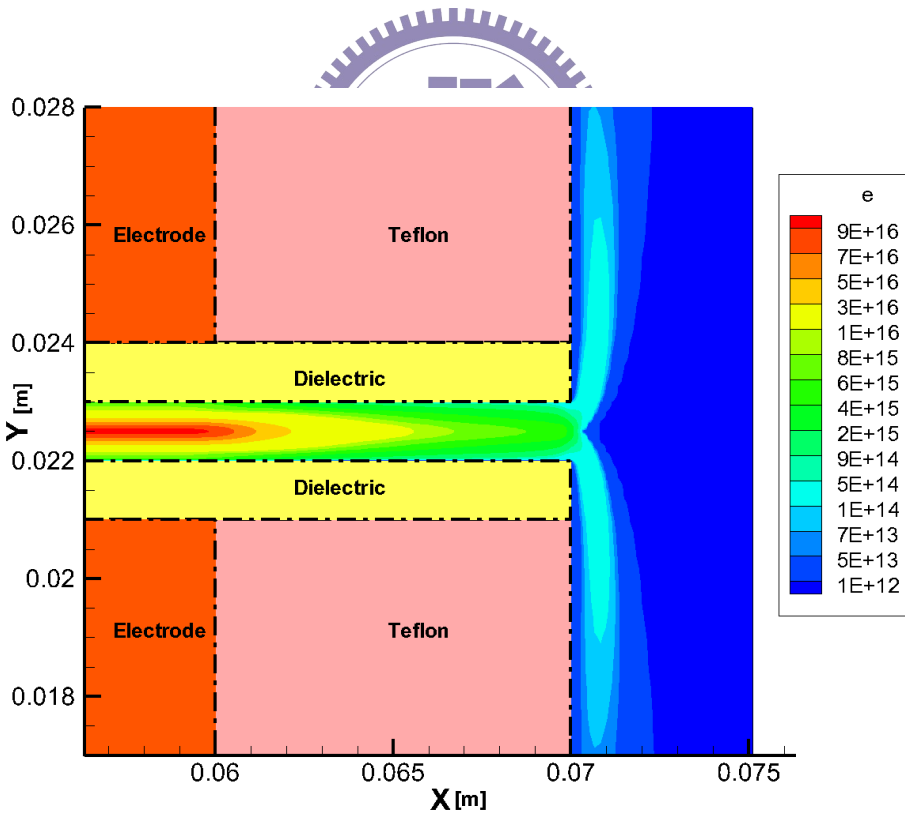
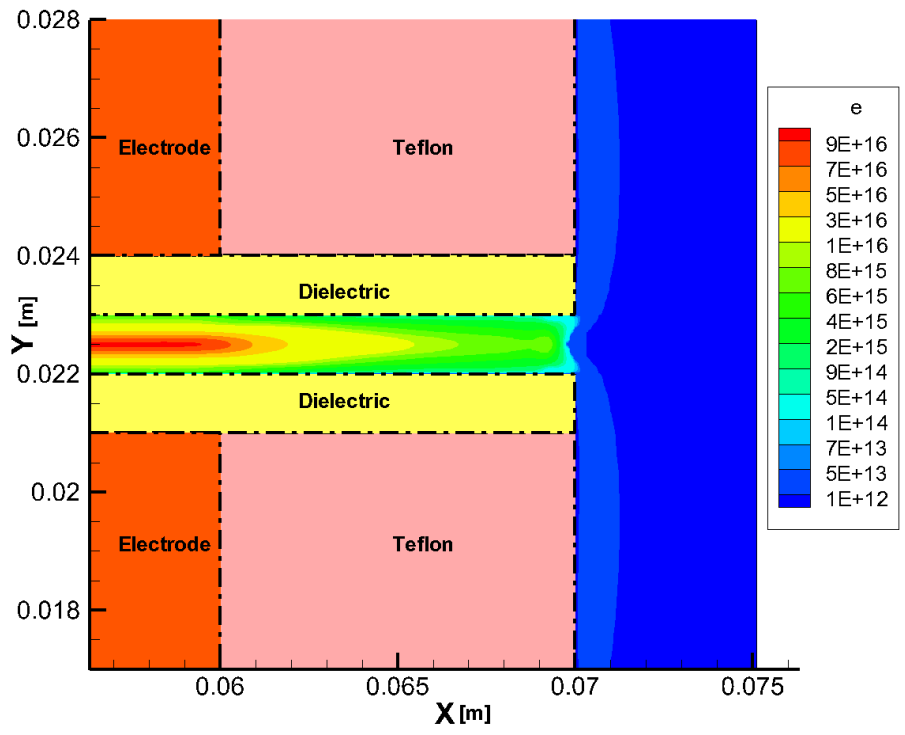


Figure 4-1: Simulated cycle average of electron number density (a) with and (b) without heating flow field.

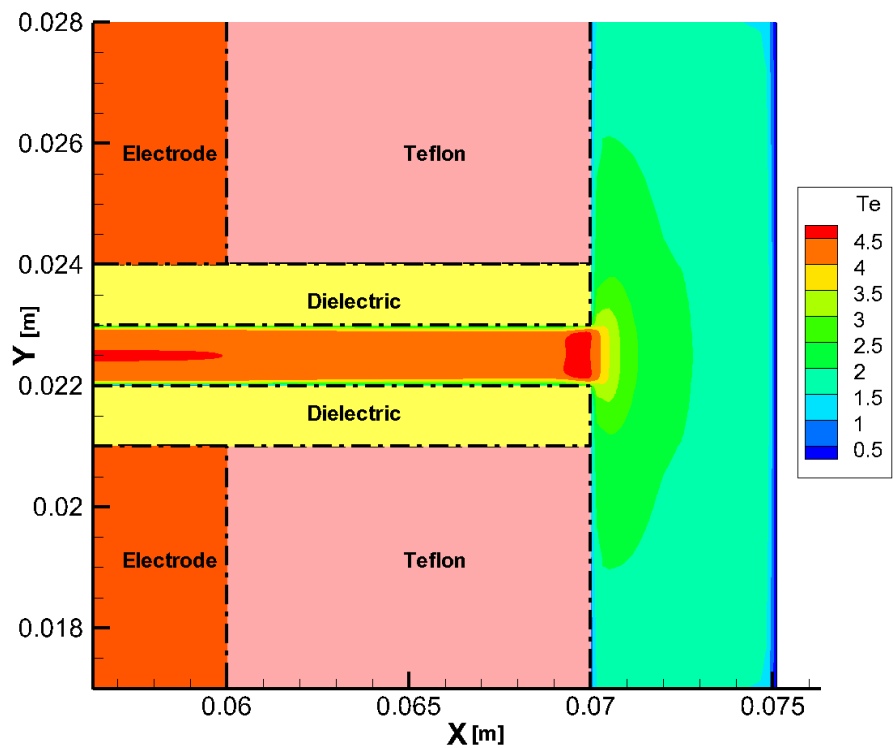
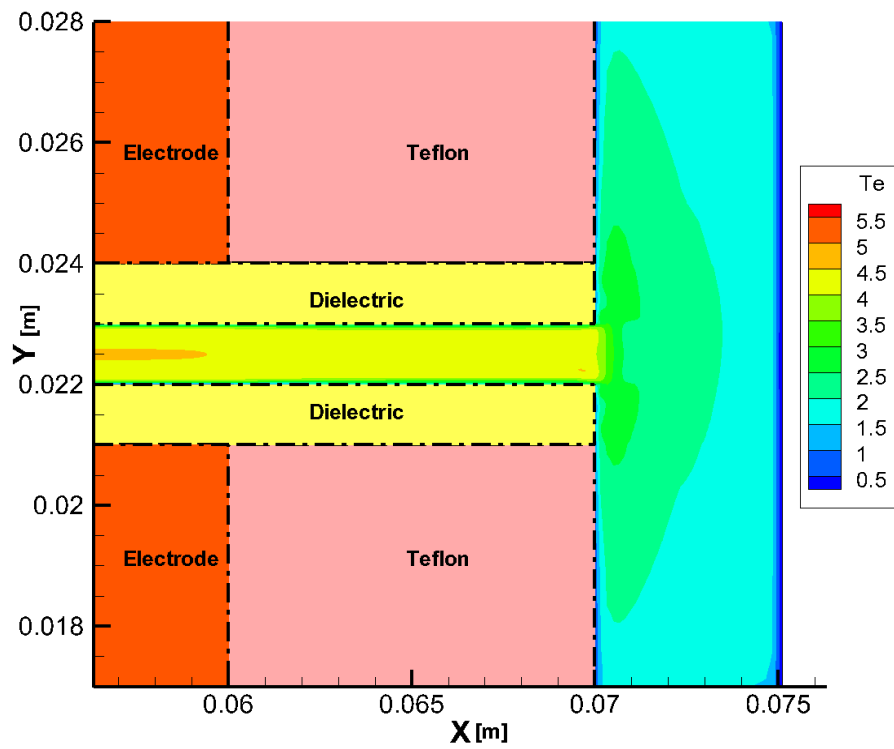


Figure 4-2: Simulated cycle averaged distributions of electron temperature (a) with and (b) without heating flow field.

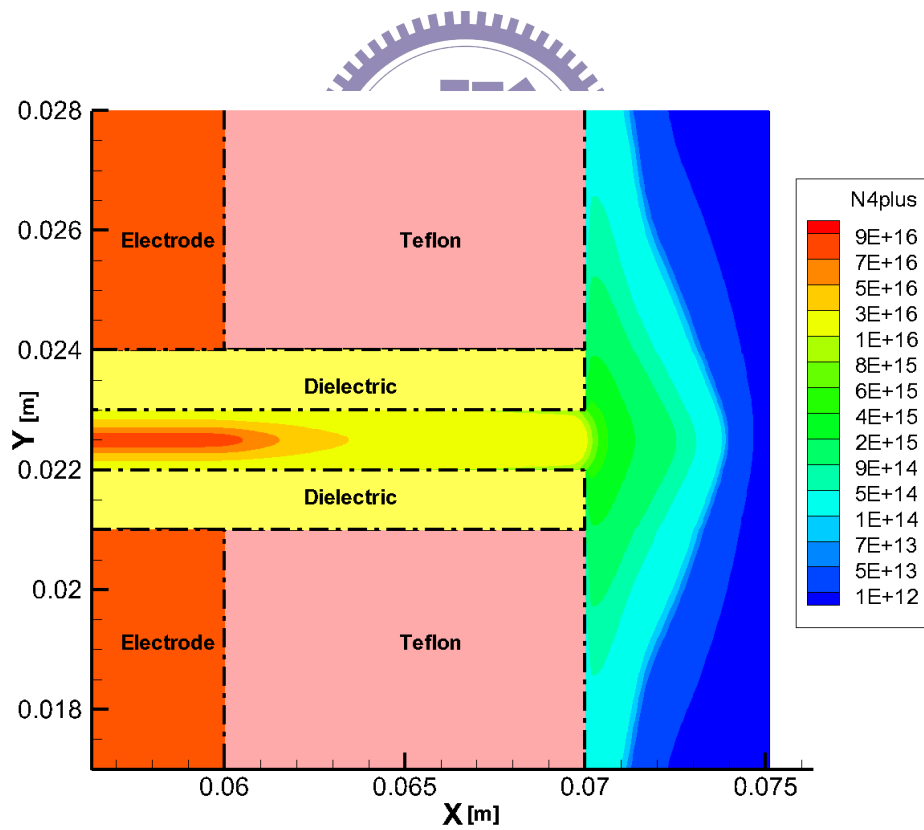
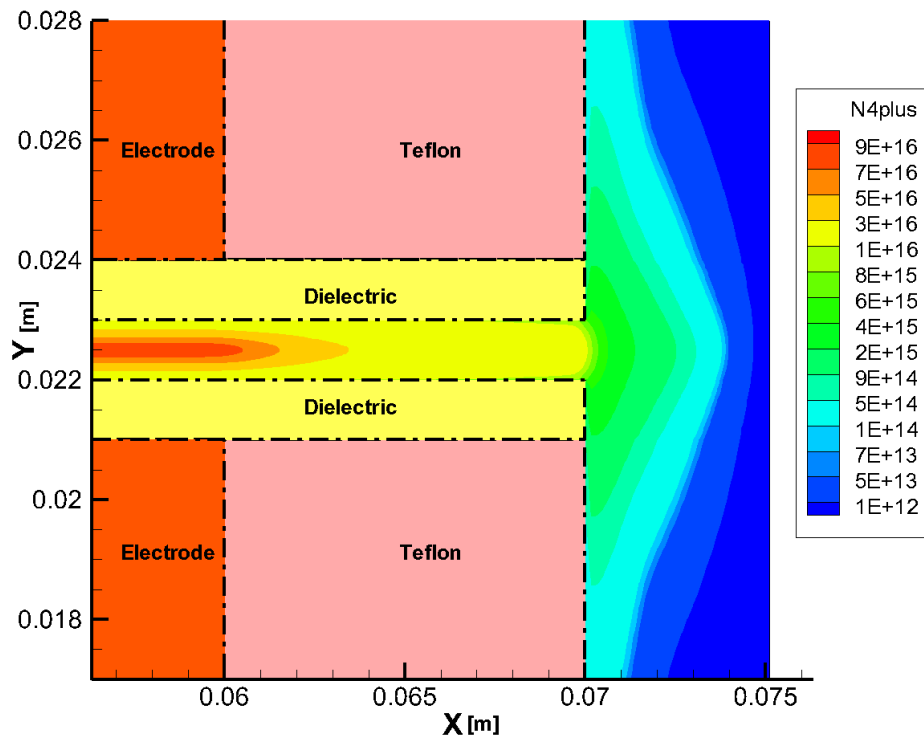


Figure 4-3: Simulated cycle averaged distributions of N4+ (a) with and (b) without considering neutral flow field.

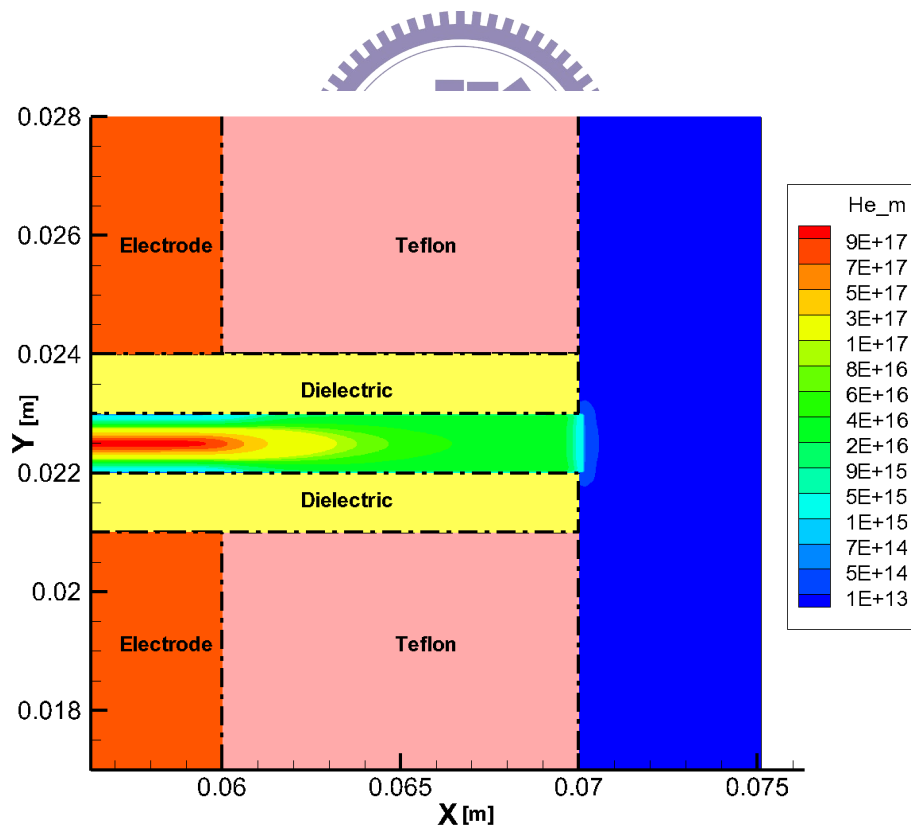
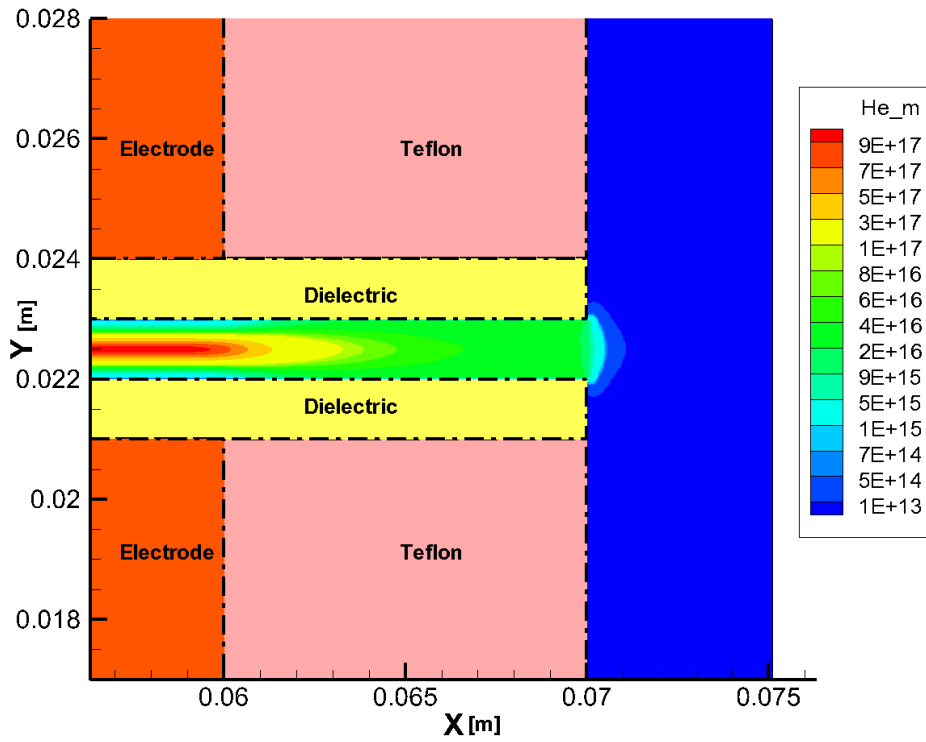


Figure 4-4: Simulated cycle averaged distributions of electron  $He_{meta}$  (a) with and (b) without heating flow field.

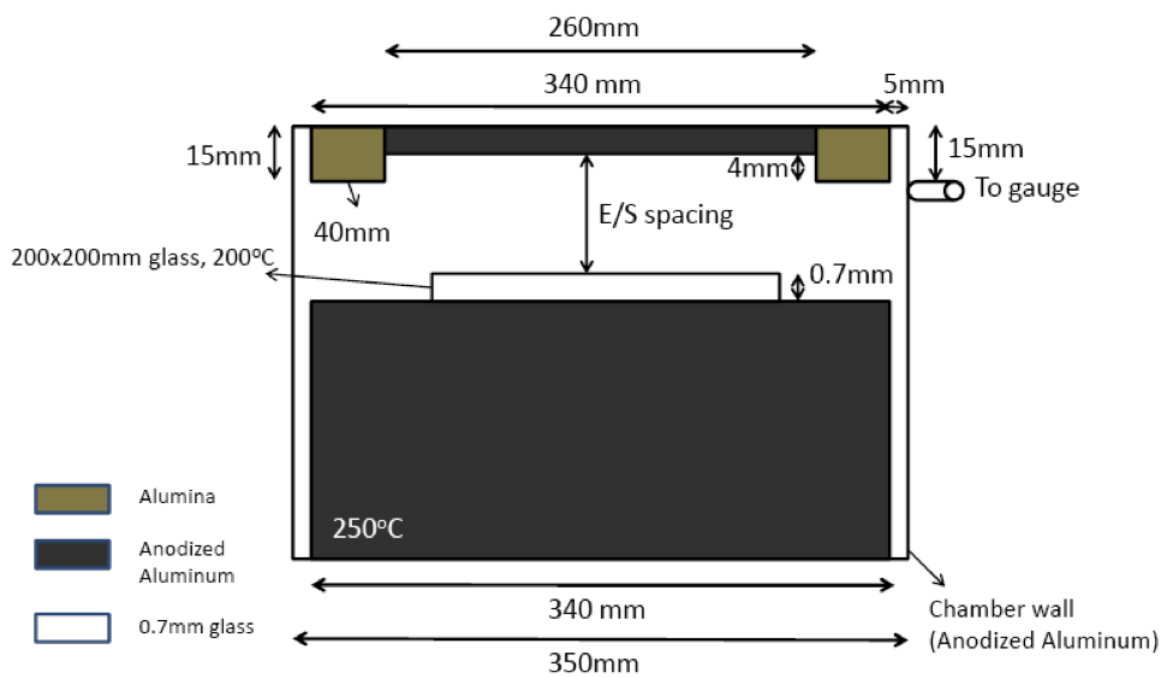


Figure 4-5: Sketch of a H<sub>2</sub>/SiF<sub>4</sub> PECVD chamber.

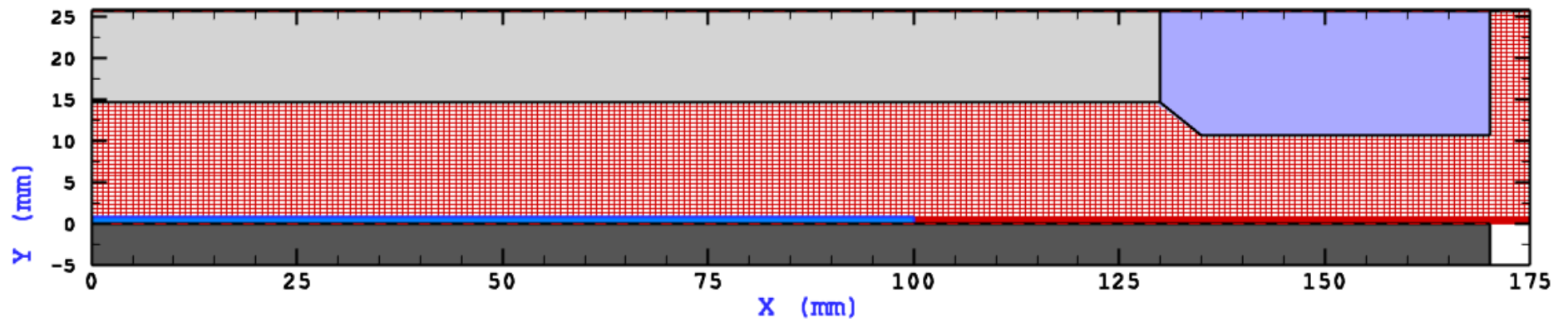


Figure 4-6: Schematic of the computational grid in the  $H_2/SiF_4$  PECVD chamber.

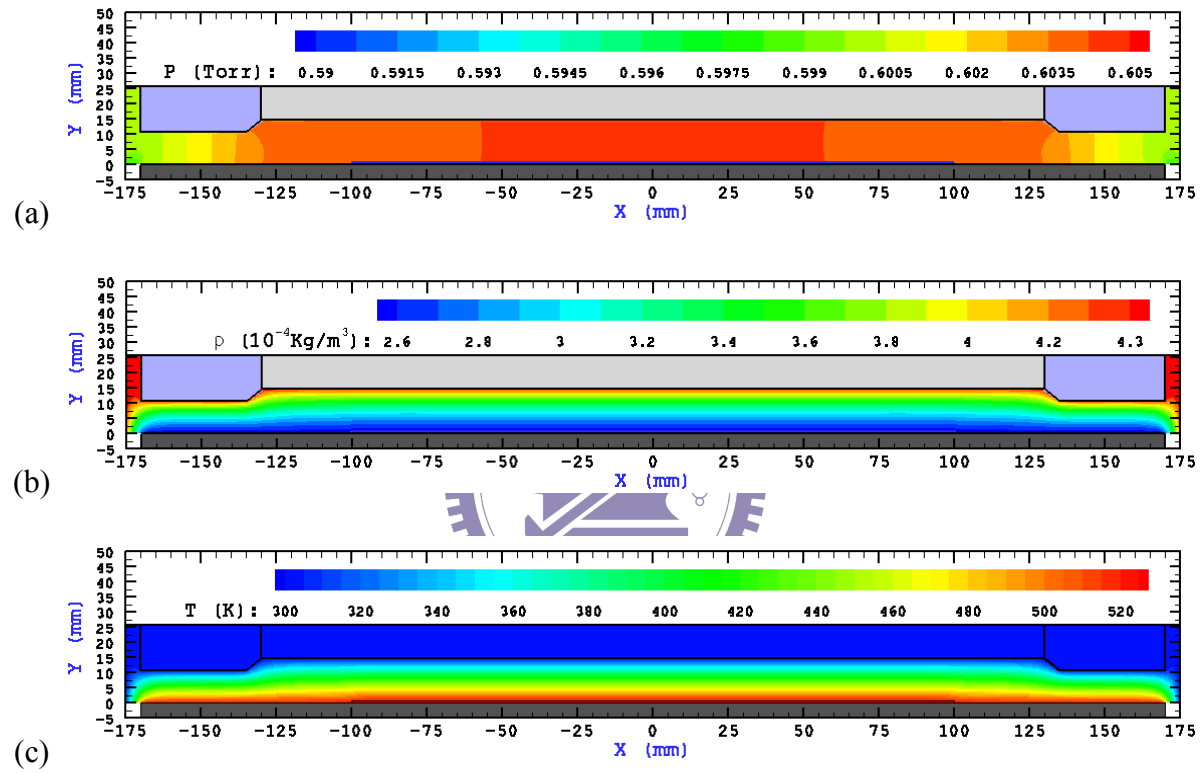


Figure 4-7: Distribution of (a) pressure, (b) density (c) and gas temperature in a PECVD chamber.



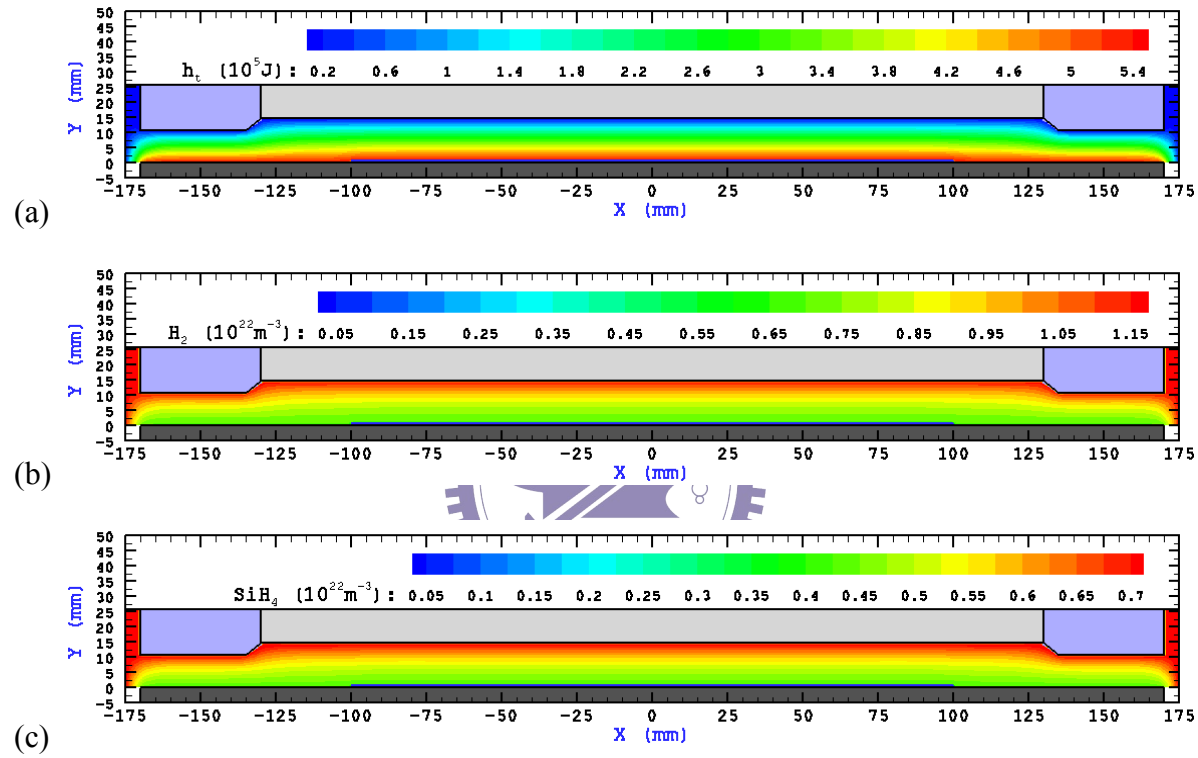


Figure 4-8: Distribution of (a) total enthalpy, (b) density of  $\text{H}_2$  and (c)  $\text{SiH}_4$  in a PECVD chamber.

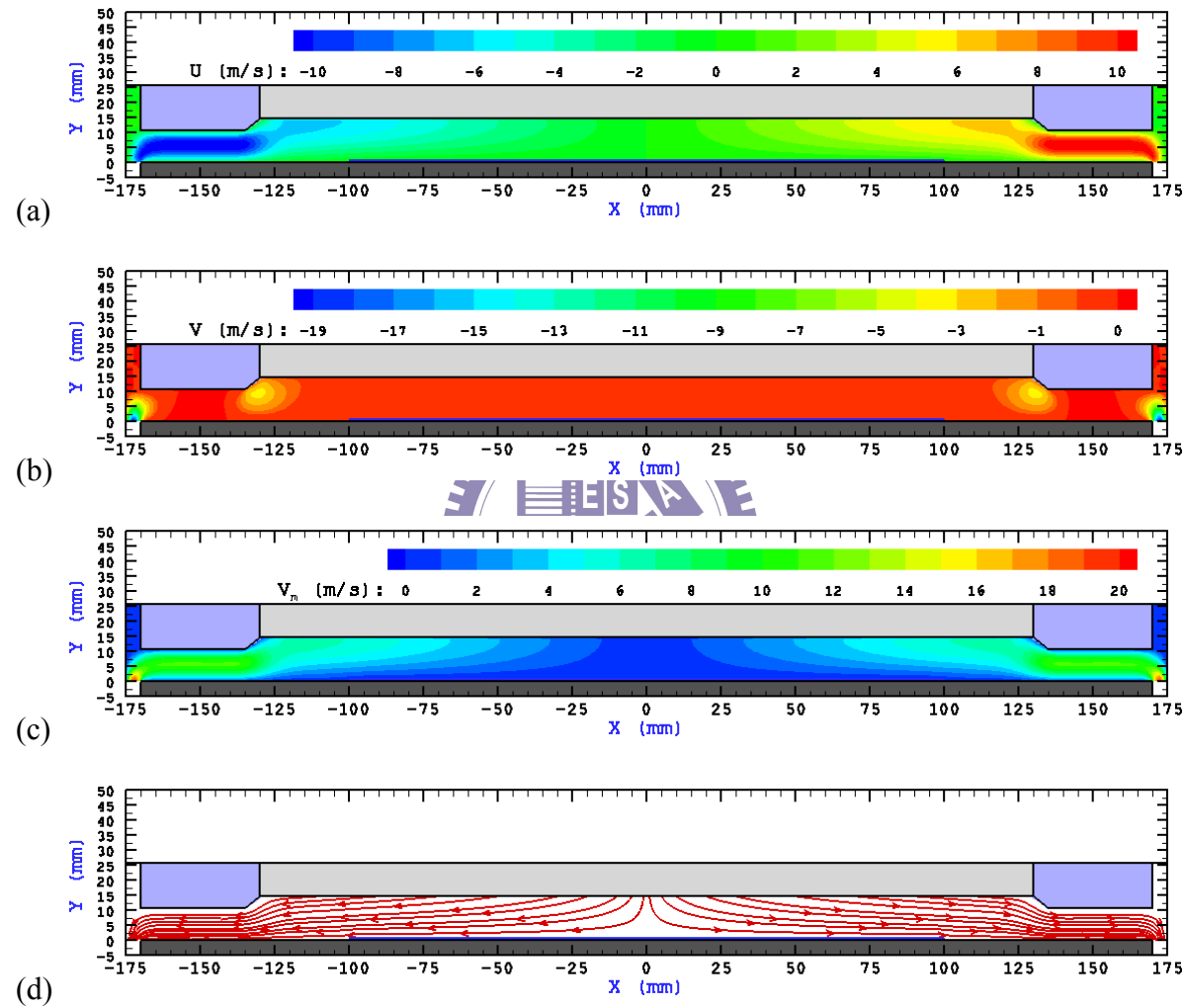


Figure 4-9: Distribution of (a) velocity in x-direction, (b) Velocity in y-direction, (c) Mean velocity and (d) streamline in a PECVD chamber.

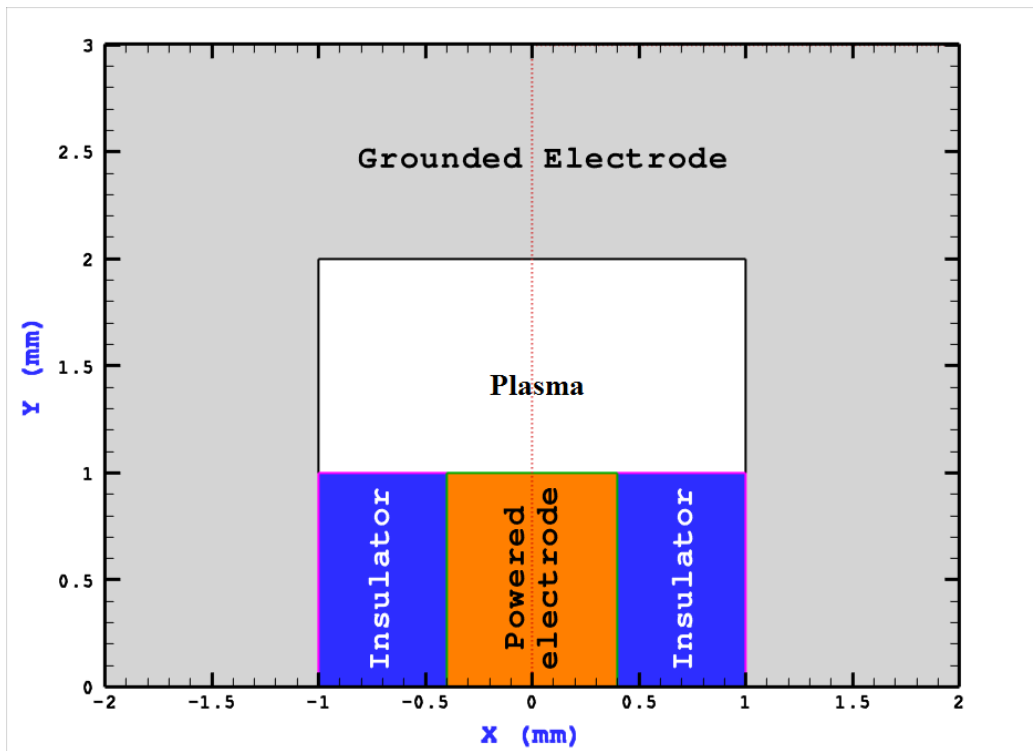


Figure 4-10: Sketch of helium micro-cell plasma.

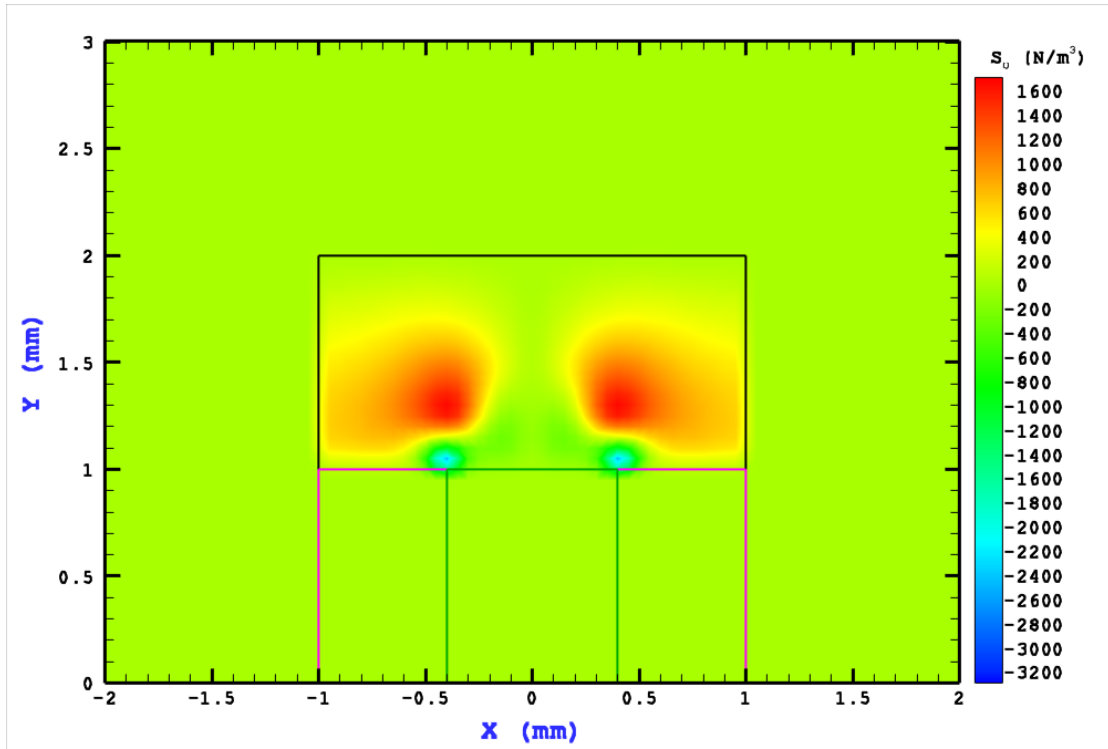


Figure 4-11: Distribution of plasma u-momentum source in the He micro-cell plasma.

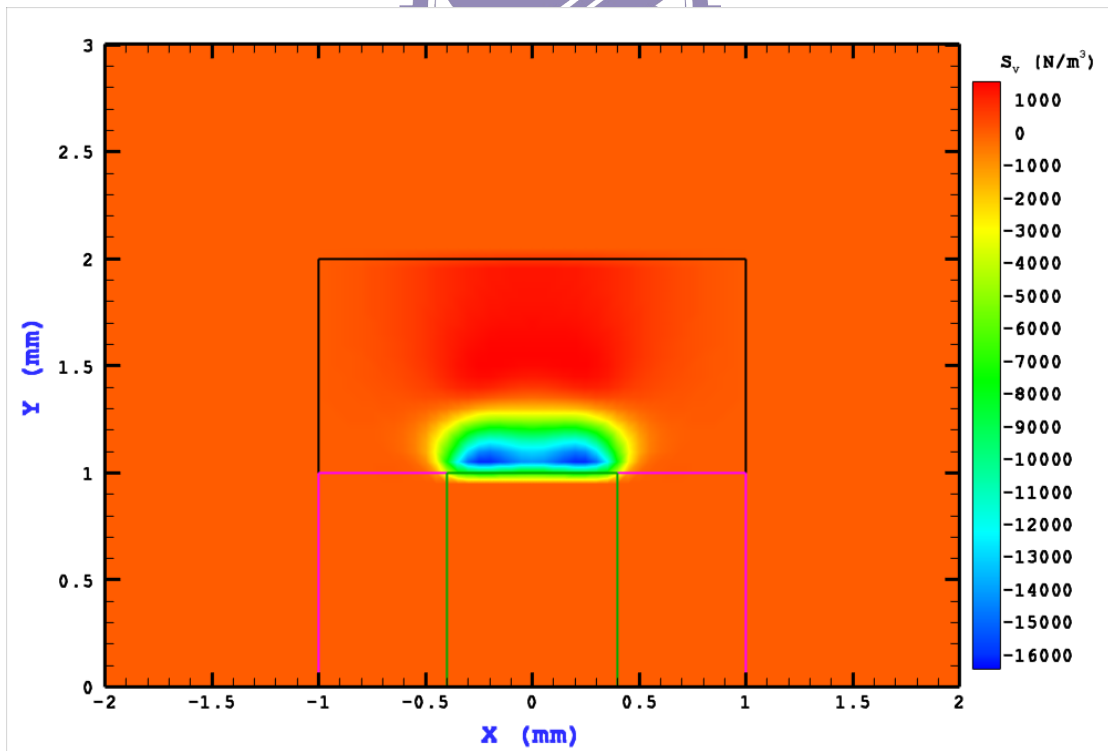


Figure 4-12: Distribution of plasma v-momentum source in the He micro-cell plasma

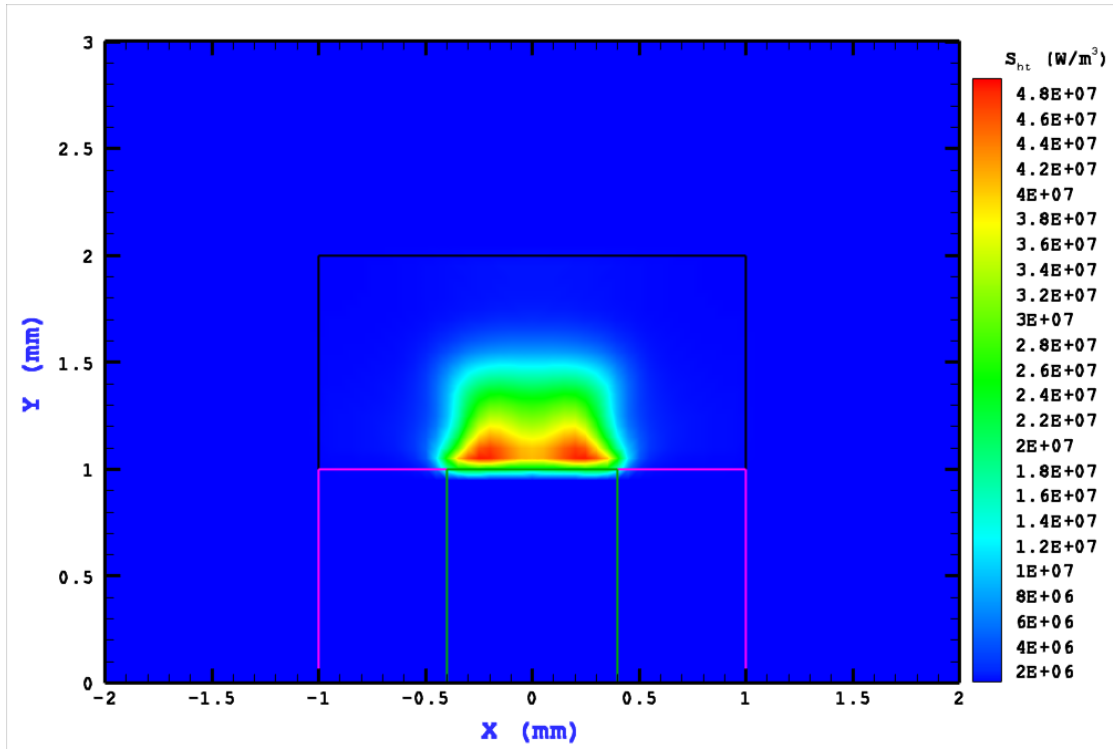


Figure 4-13: Distribution of plasma energy source in the He micro-cell plasma.

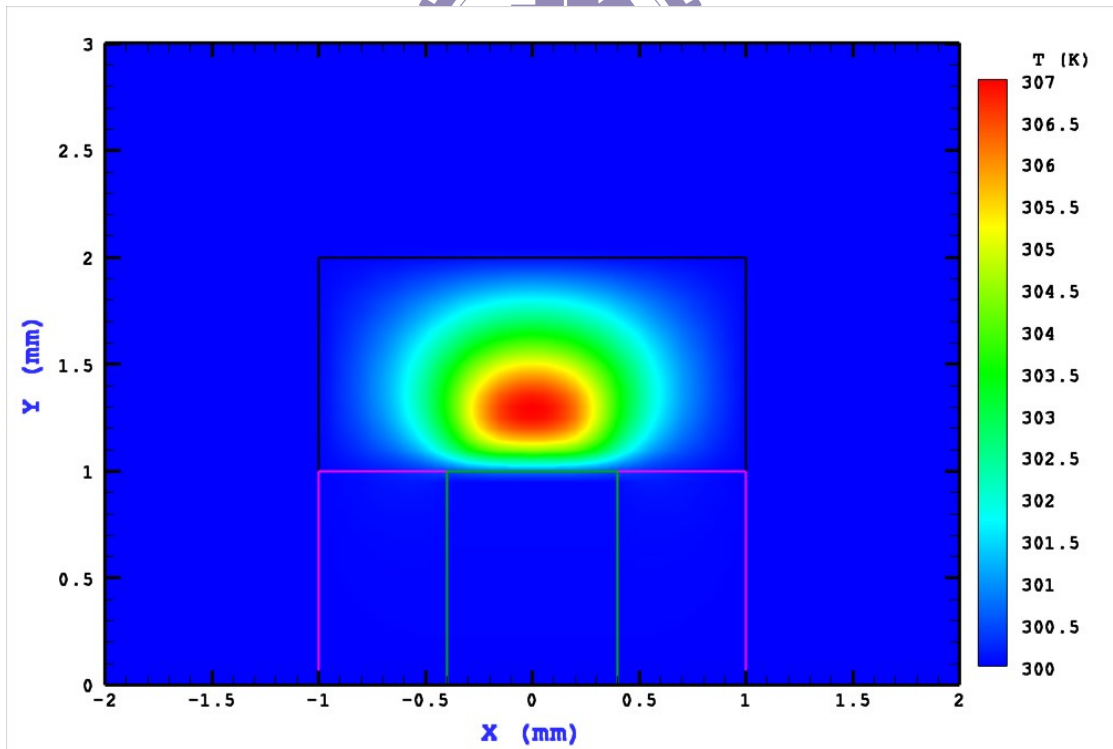


Figure 4-14: Temperature distribution of a He micro-cell plasma without considering plasma momentum source.

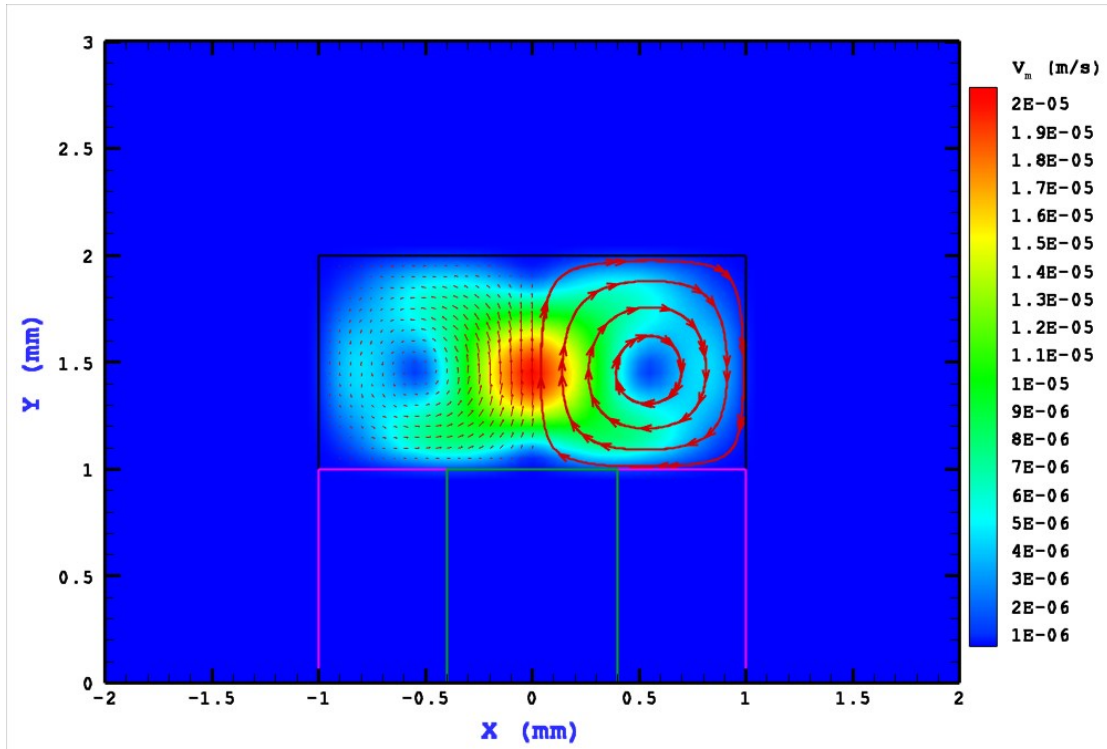


Figure 4-15: Mean speed distribution of a He micro-cell plasma without considering plasma momentum source.

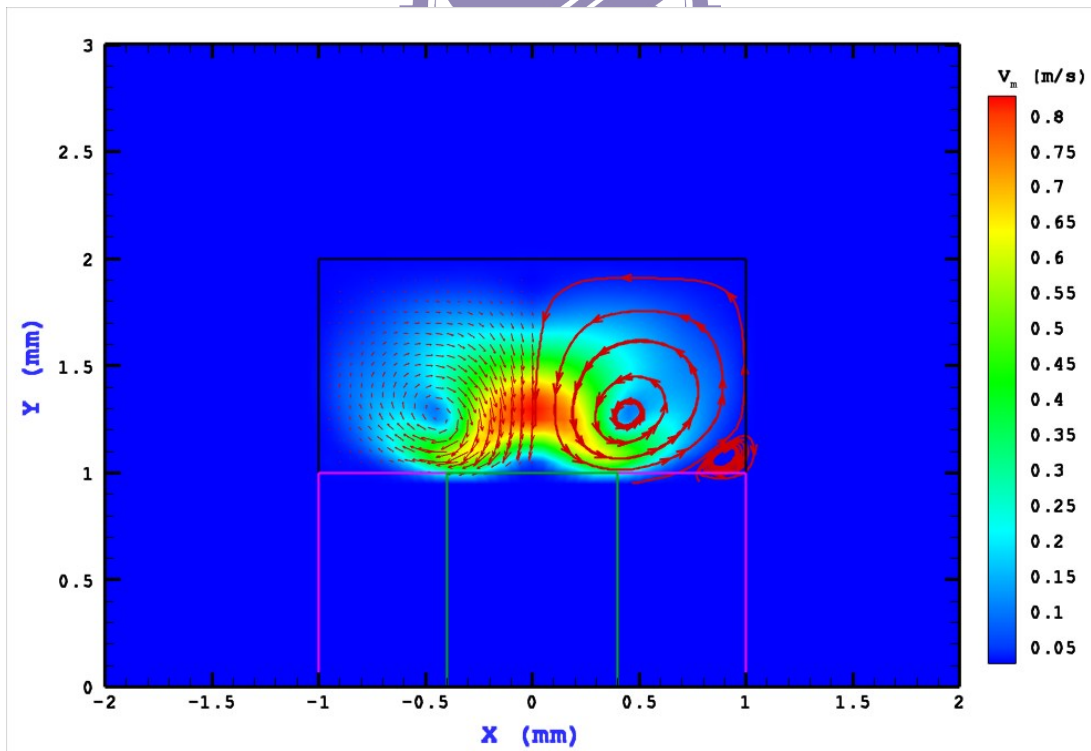


Figure 4-16: Mean speed distribution of a He micro-cell plasma with considering plasma momentum source.

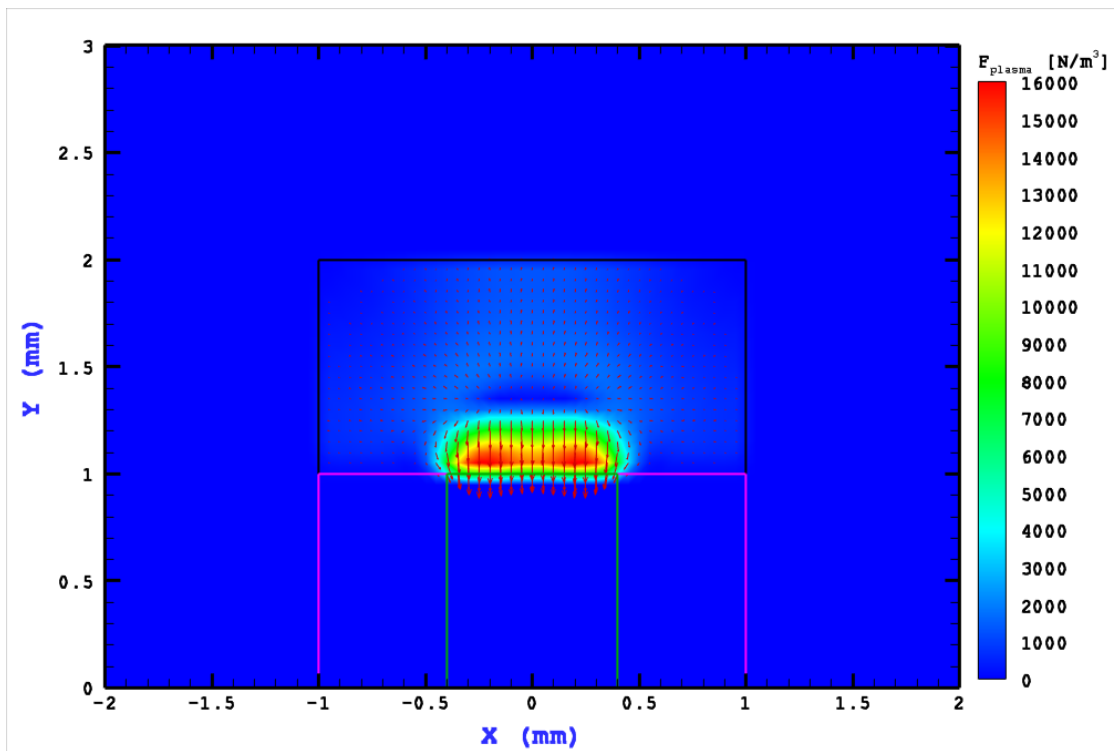


Figure 4-17: Force field distribution of a He micro-cell plasma.

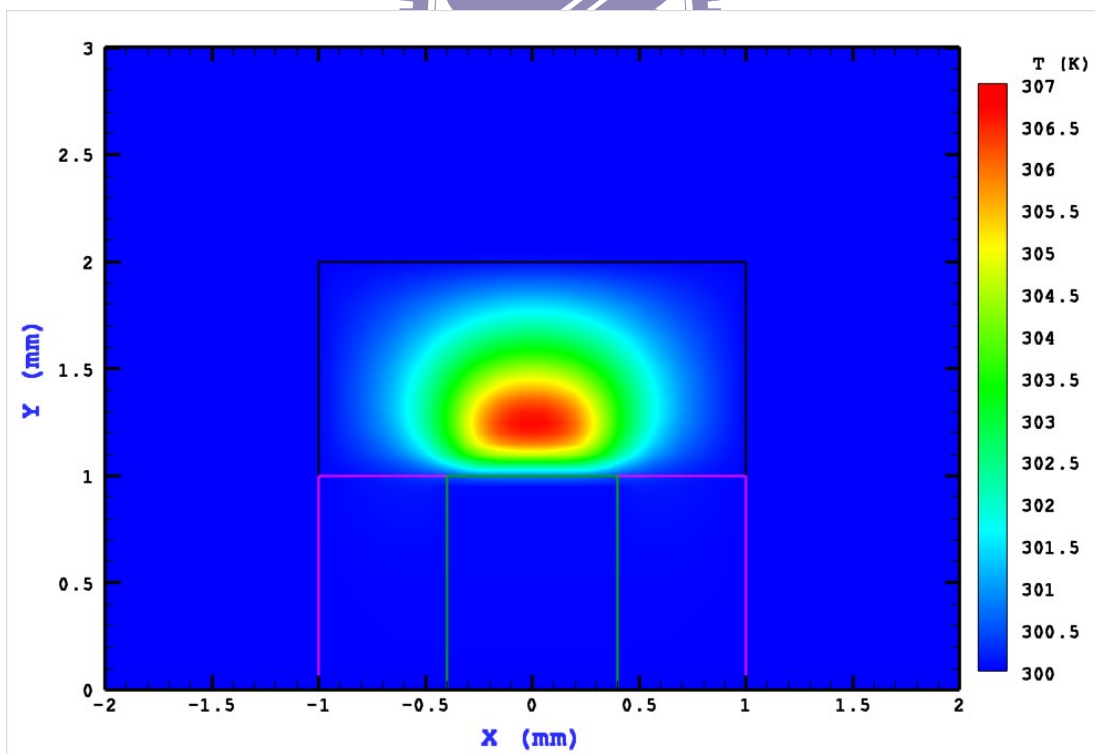


Figure 4-18: Temperature distribution of a He micro-cell plasma with considering plasma momentum source.

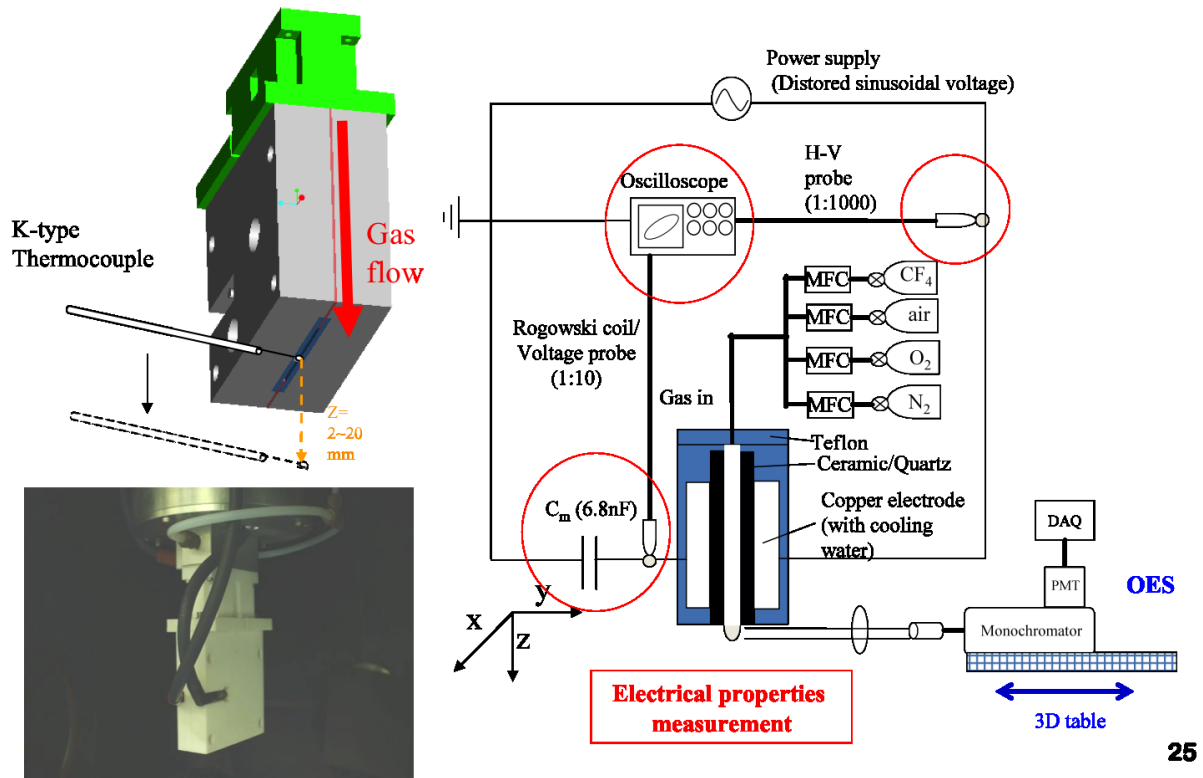


Figure 4-19: Schematic sketch of a planar dielectric barrier discharge atmospheric-pressure plasma jet.



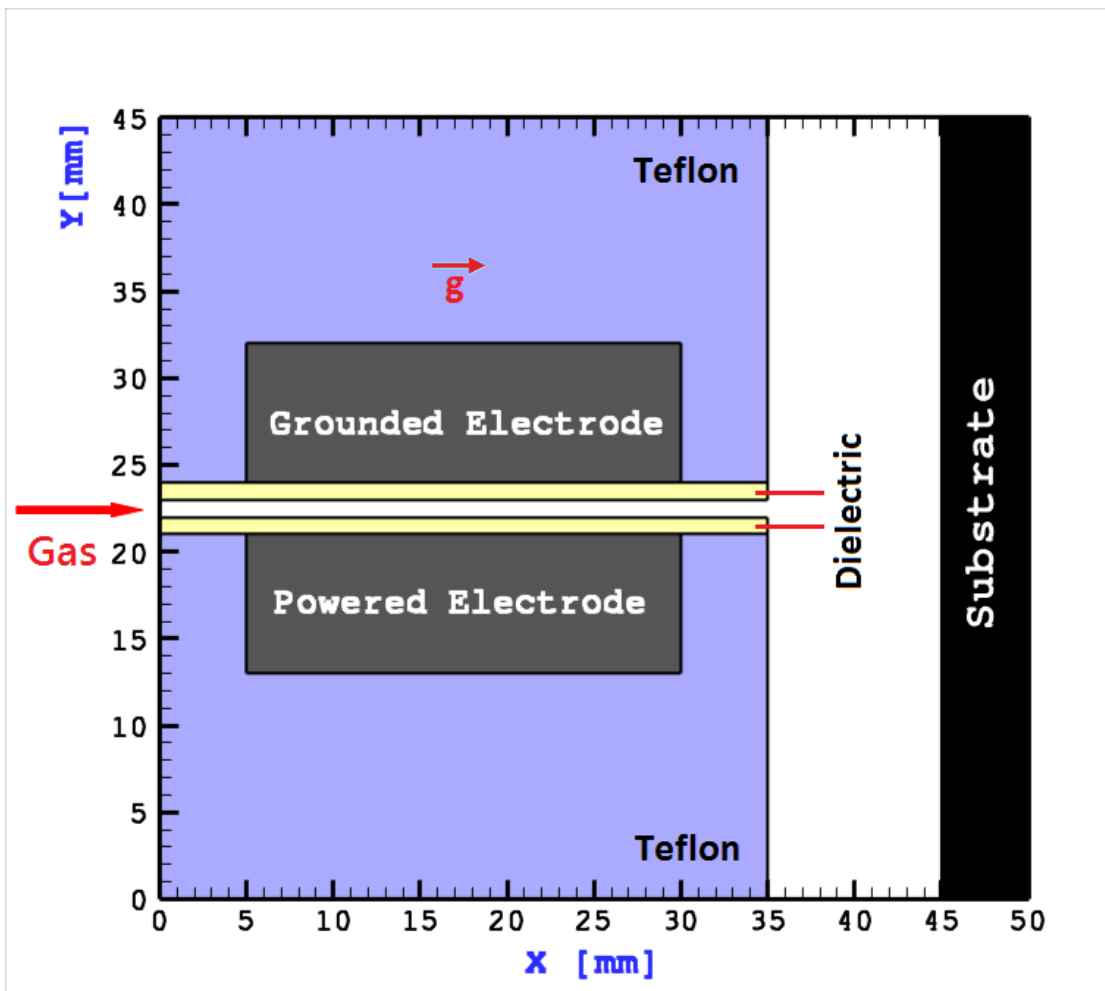


Figure 4-20. Sketch of two-dimensional dielectric barrier discharge atmospheric-pressure plasma jet.

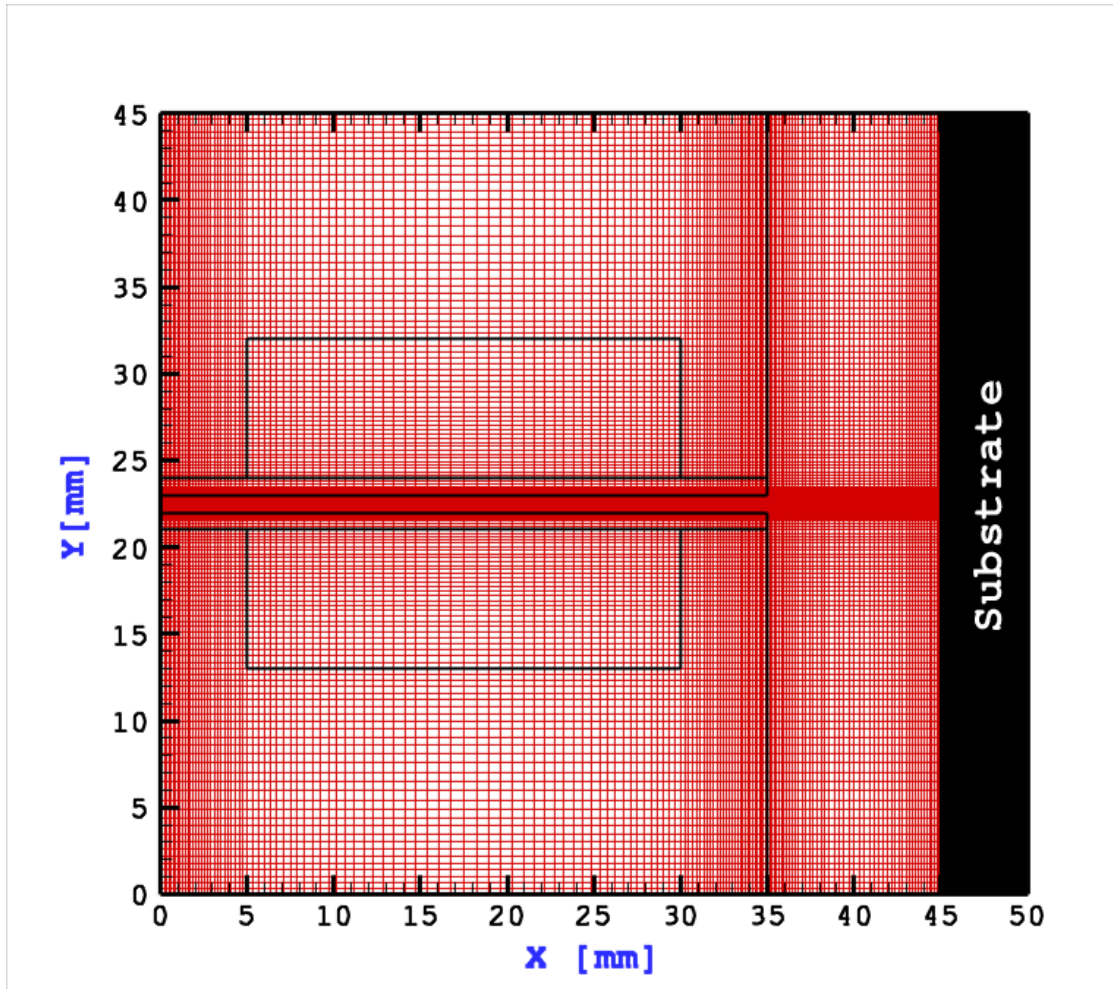


Figure 4-21. Schematic of the computational grid in the two-dimensional dielectric barrier discharge atmospheric-pressure plasma jet.

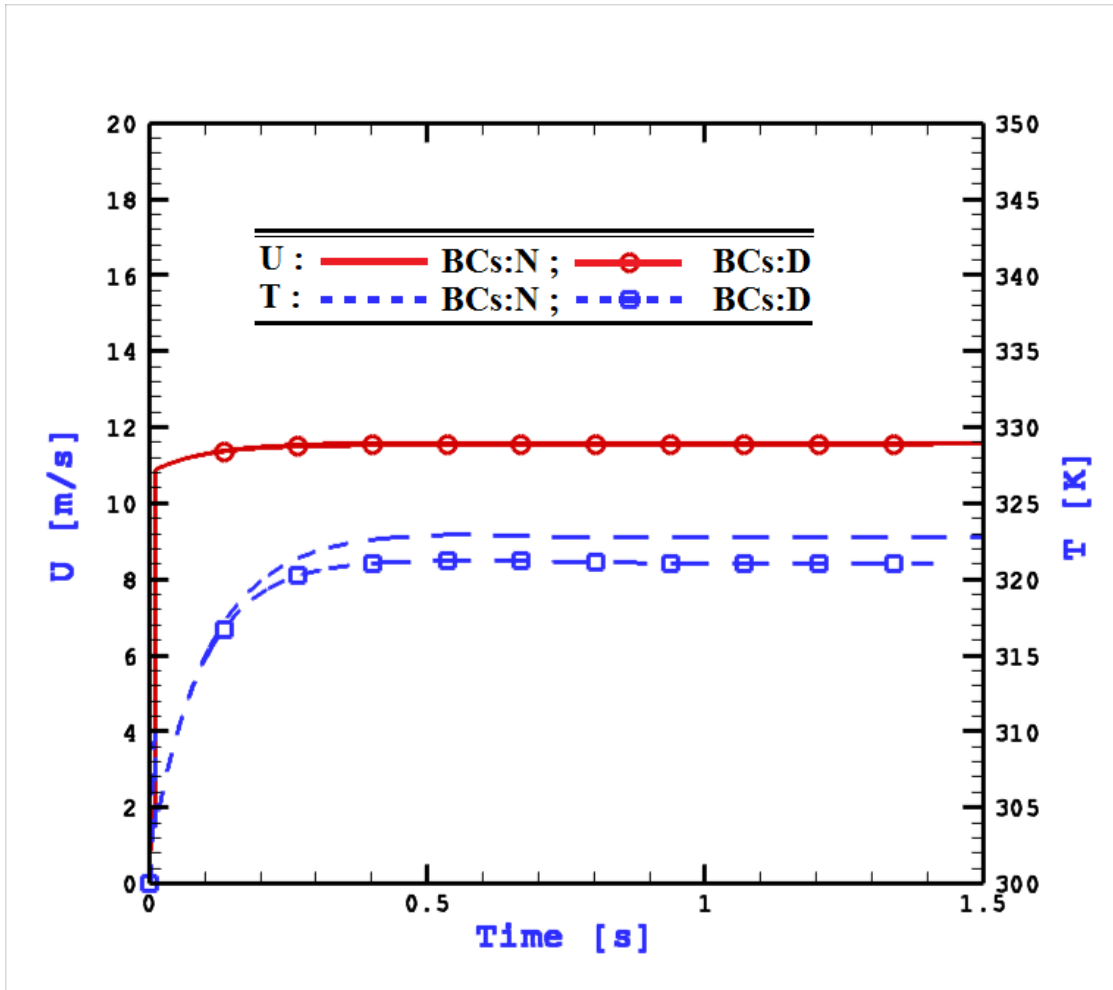


Figure 4-22. Time history of velocity and temperature profiles at the export of helium

DBD APPJ for  $d = 1 \text{ mm}$ ,  $H/d = 10$ ,  $Re = 60$  and gas flow rate of 20 slm.

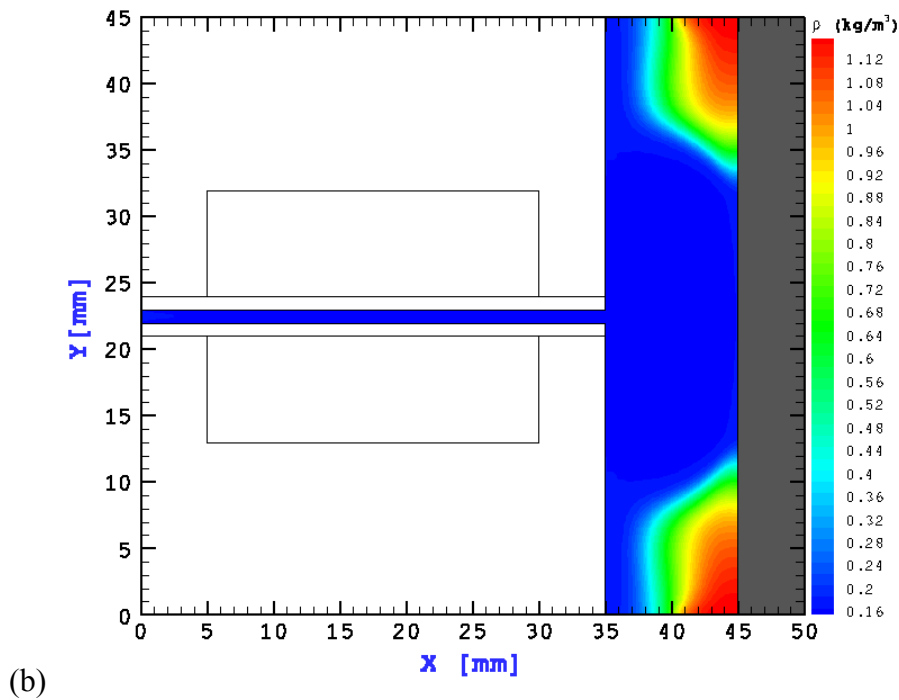
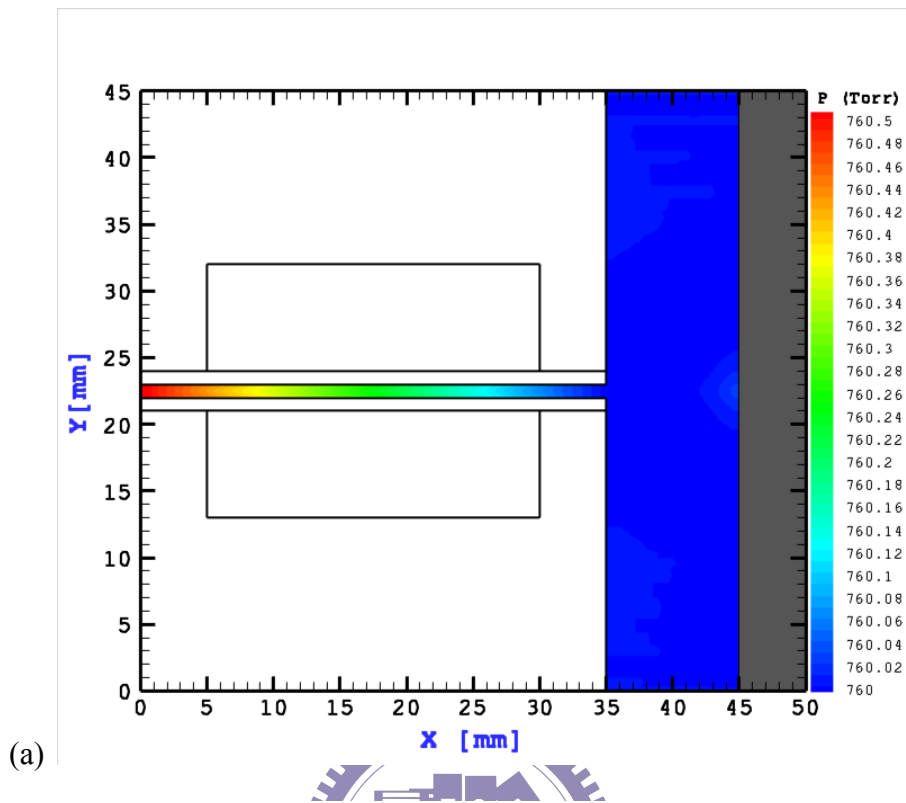


Figure 4-23: Steady-state distribution of (a) pressure and (b) density of helium DBD

APPJ for  $d = 1 \text{ mm}$ ,  $H/d = 10$ ,  $Re = 60$  and gas flow rate of  $20 \text{ slm}$ .

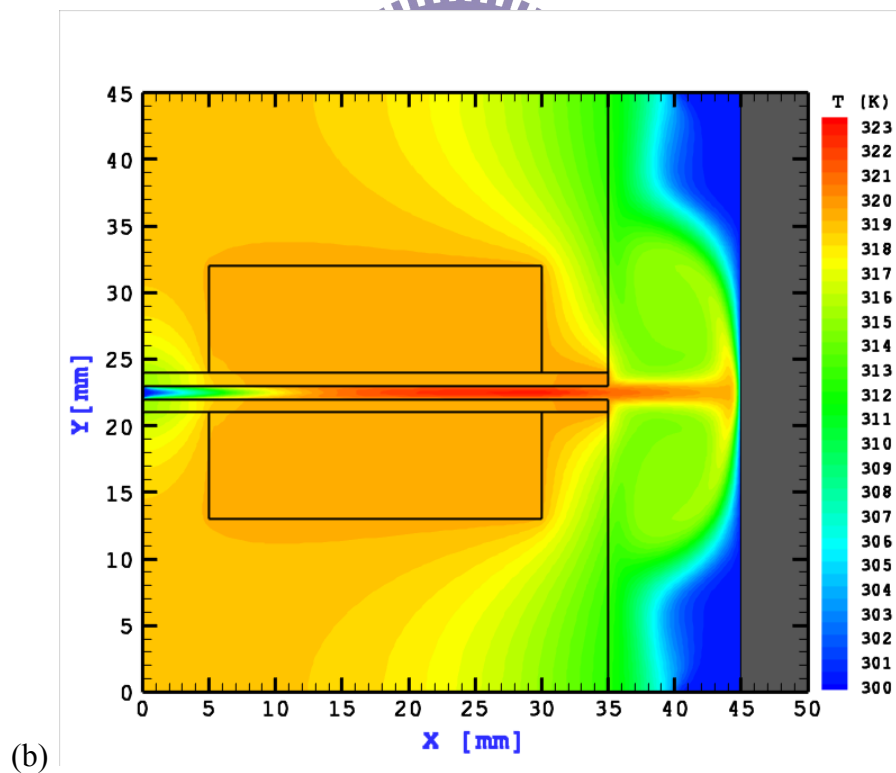
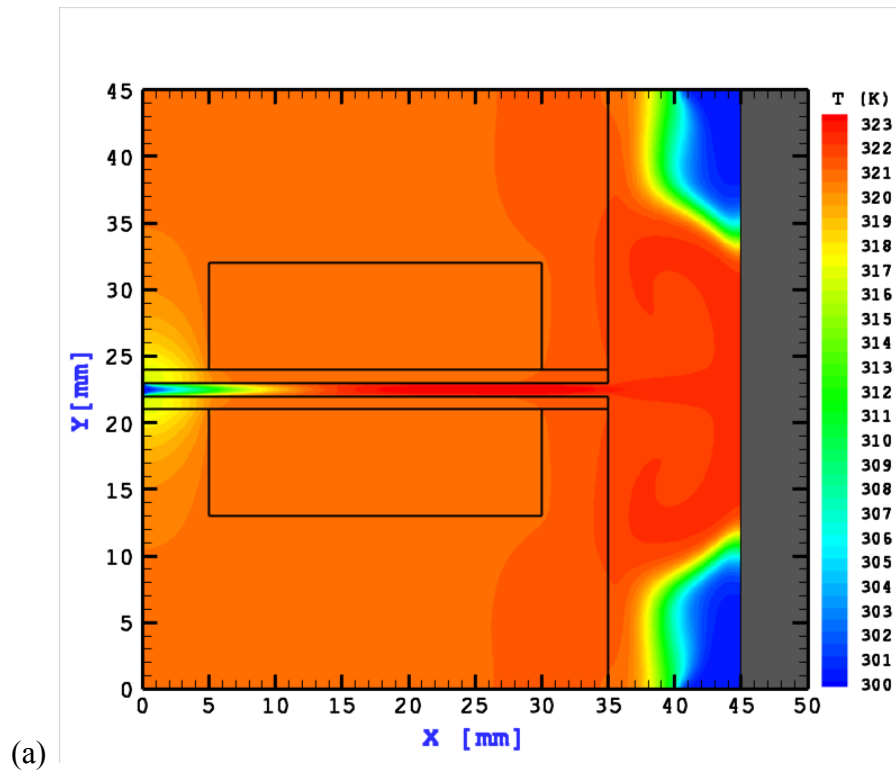


Figure 4-24: Spatial distribution of temperature with (a) a adiabatic substrate surface; (b) an isothermal substrate surface of a helium DBD APPJ for  $d = 1 \text{ mm}$ ,  $H/d = 10$ ,  $Re = 60$  and gas flow rate of  $20 \text{ slm}$ .

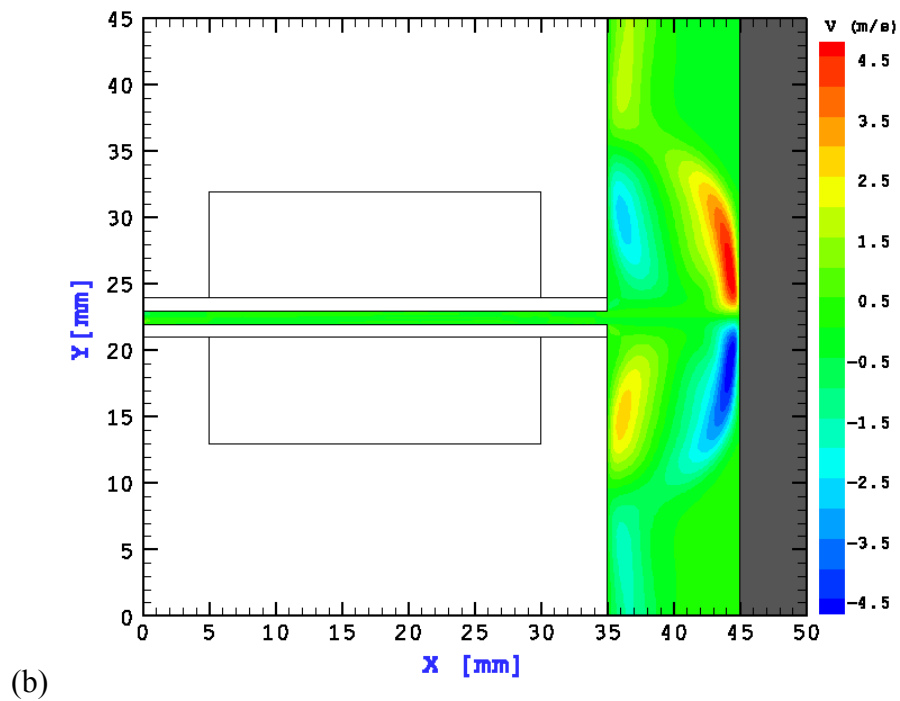
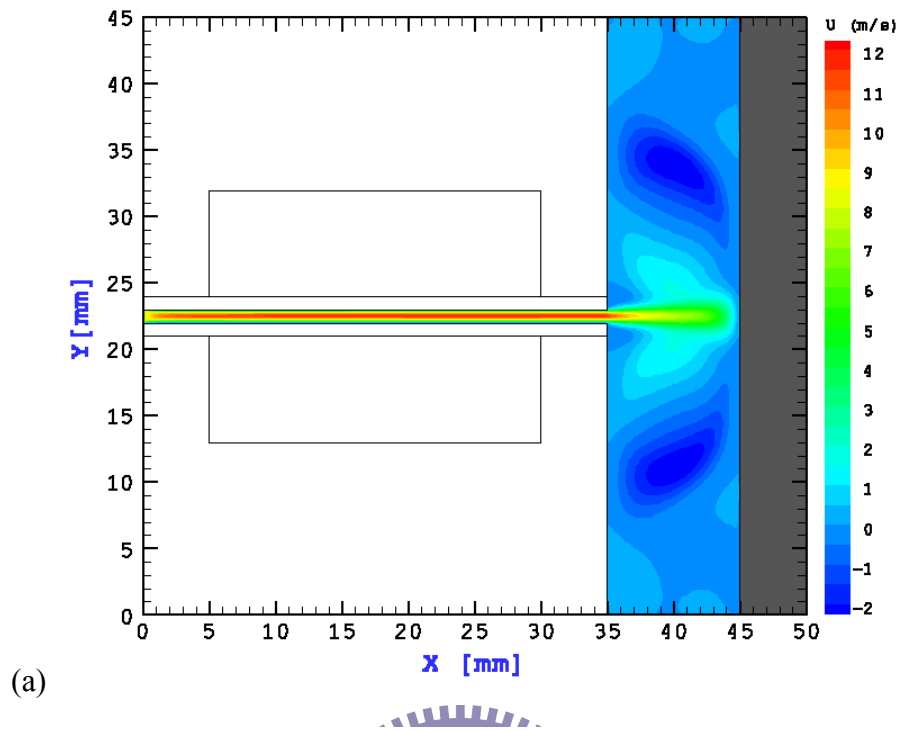


Figure 4-25: Spatial distribution of velocity (a) in x-direction and (b) in y-direction of helium DBD APPJ for  $d = 1 \text{ mm}$ ,  $H/d = 10$ ,  $\text{Re} = 60$  and gas flow rate of  $20 \text{ slm}$ .

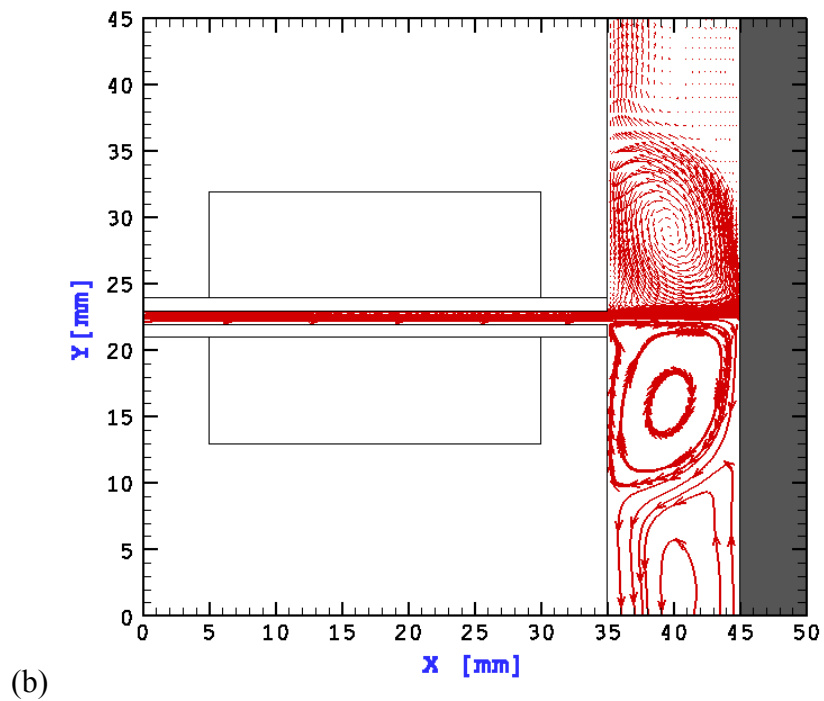
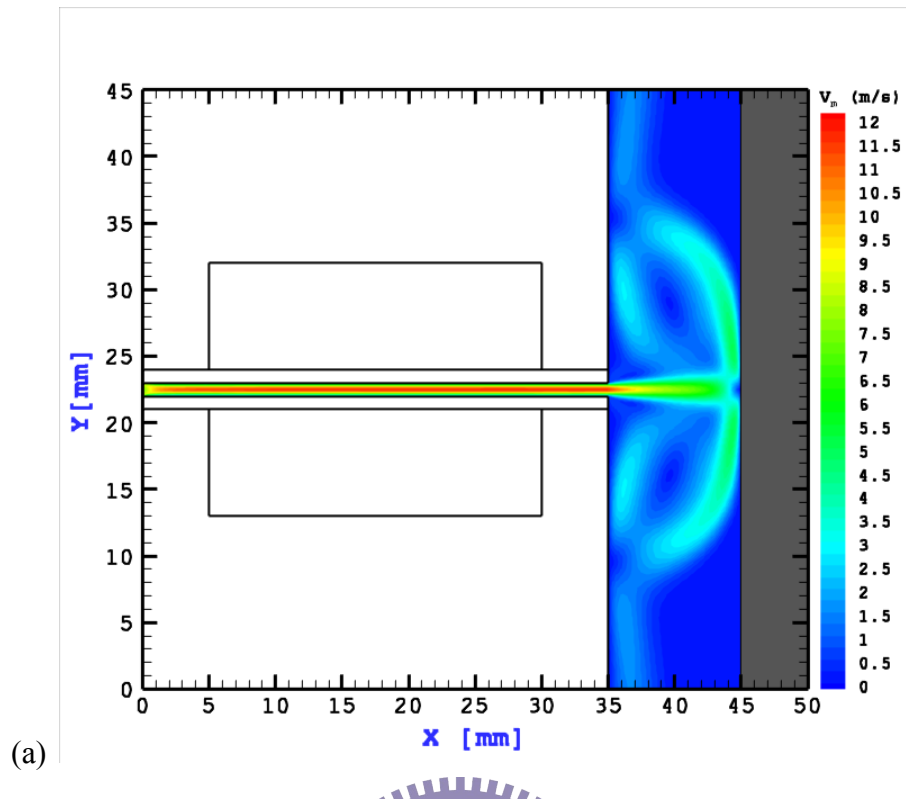


Figure 4-26: Steady-steady distributions of (a) mean speed, (b) streamlines and velocity vector of helium DBD APPJ for  $d = 1$  mm,  $H/d = 10$ ,  $Re = 60$  and gas flow rate of 20 slm.

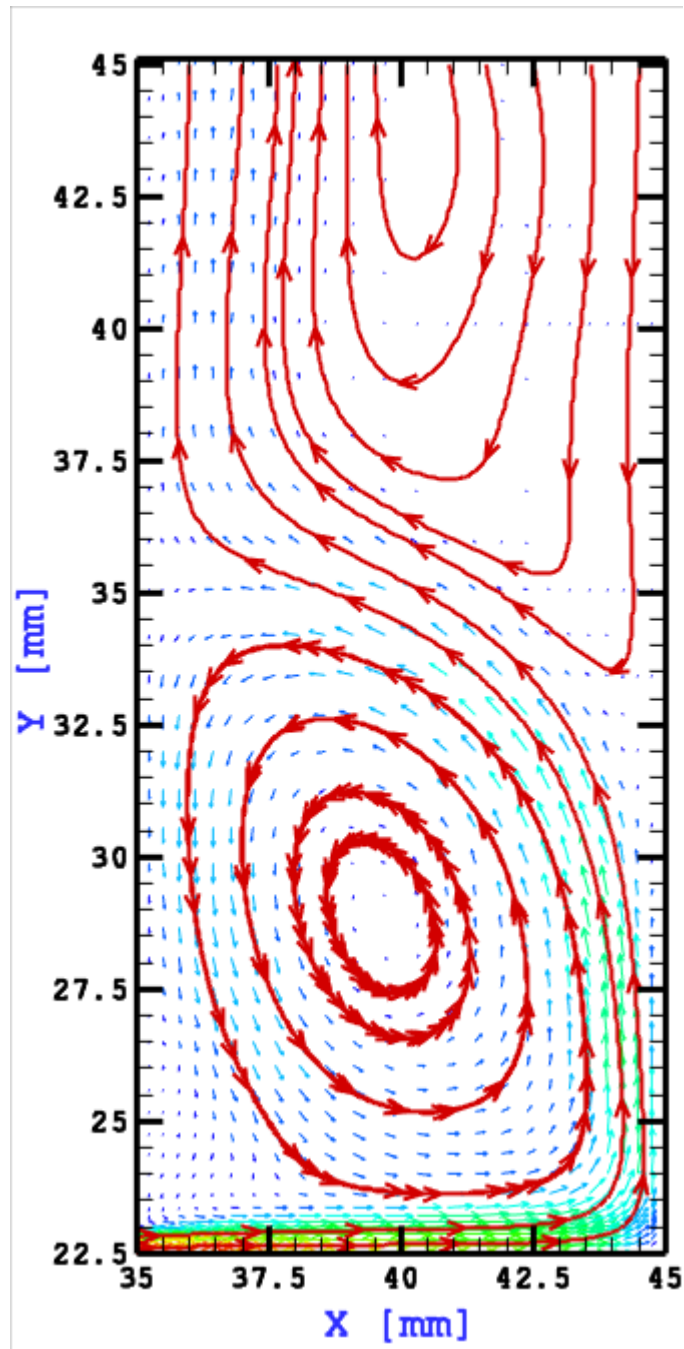


Figure 4-27: streamlines and velocity vector patterns of helium DBD APPJ for  $d = 1 \text{ mm}$ ,  $H/d = 10$ ,  $Re = 60$  and gas flow rate of  $20 \text{ slm}$ .



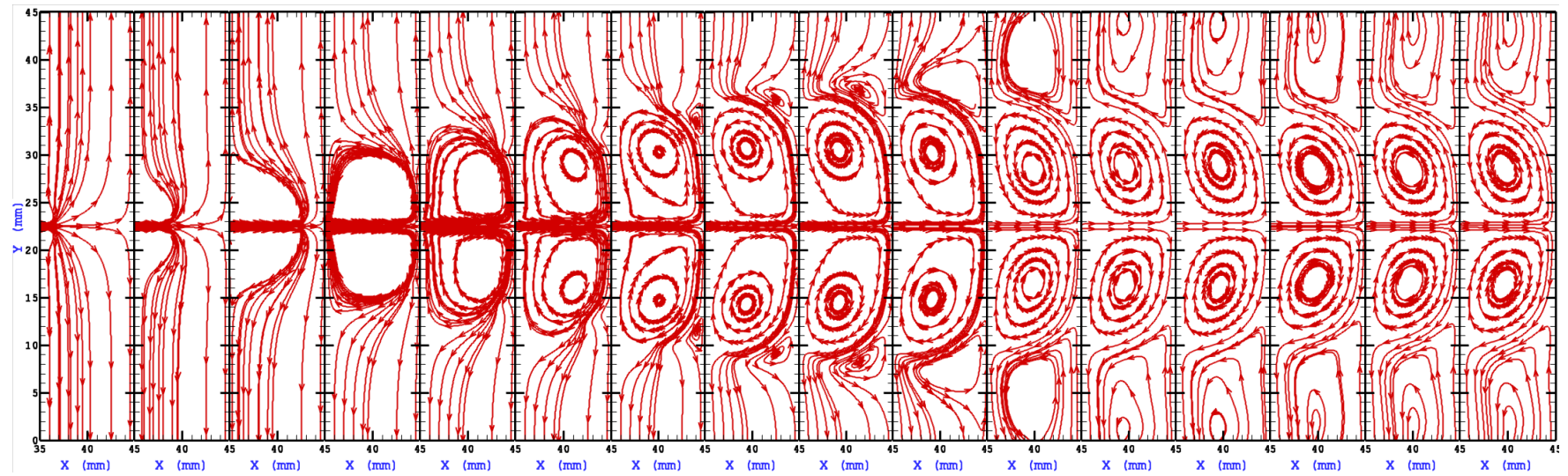


Figure 4-28: Time history of streamlines and velocity vector patterns of helium DBD APPJ for  $d = 1$  mm,  $H/d = 10$ ,  $Re = 60$  and gas flow rate of 20 slm .

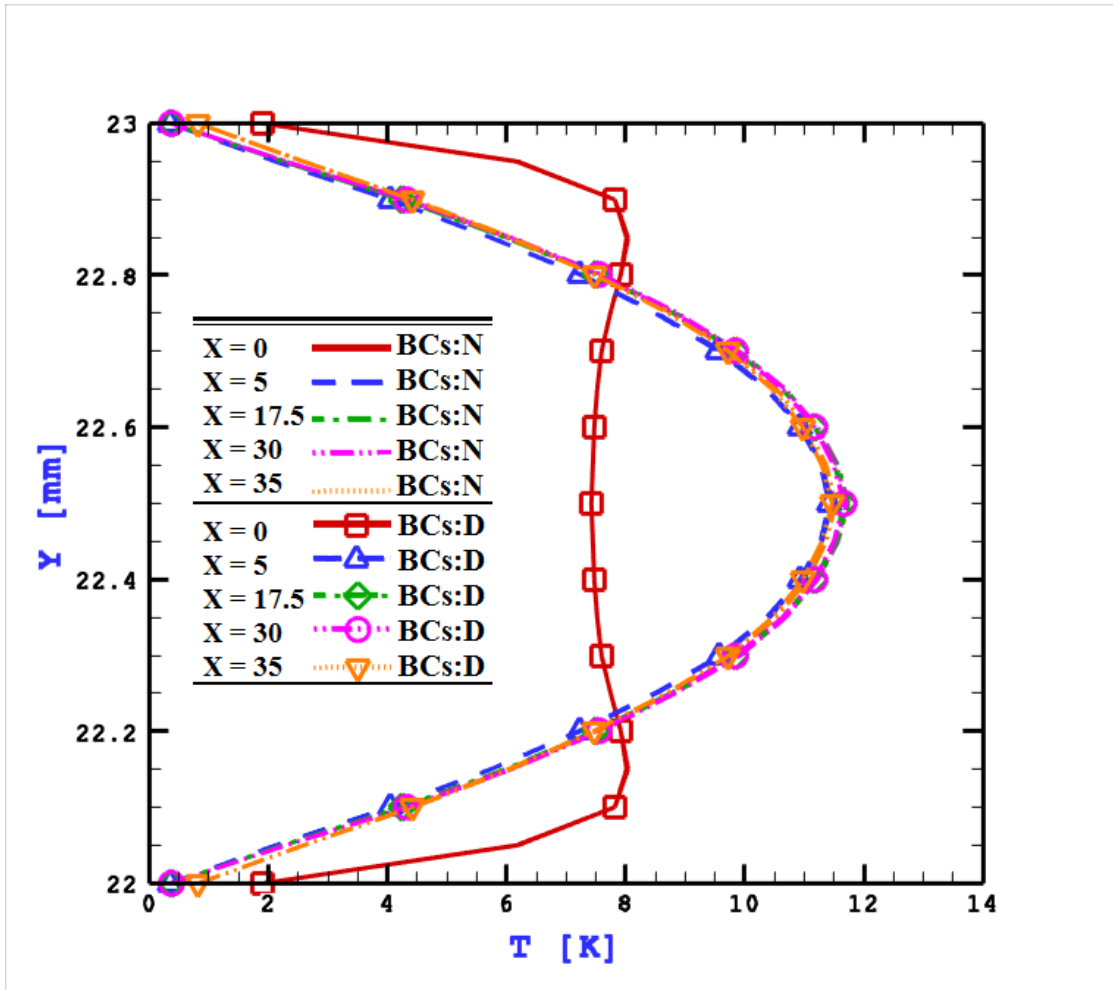


Figure 4-29. Horizontal velocity profiles in the helium DBD APPJ channel at different x positions for  $d = 1$  mm,  $H/d = 10$ ,  $Re = 60$  and gas flow rate of 20 slm .

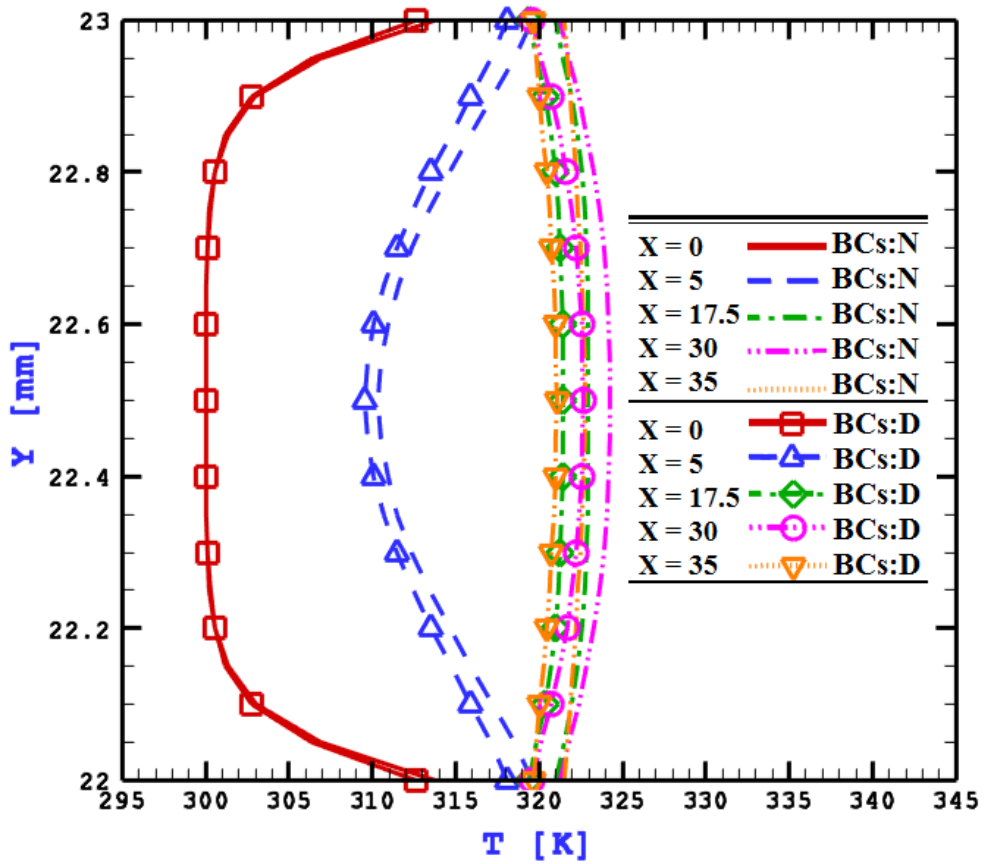


Figure 4-30. Temperature profiles in the helium DBD APPJ channel at different x positions for  $d = 1 \text{ mm}$ ,  $H/d = 10$ ,  $Re = 60$  and gas flow rate of  $20 \text{ slm}$ .

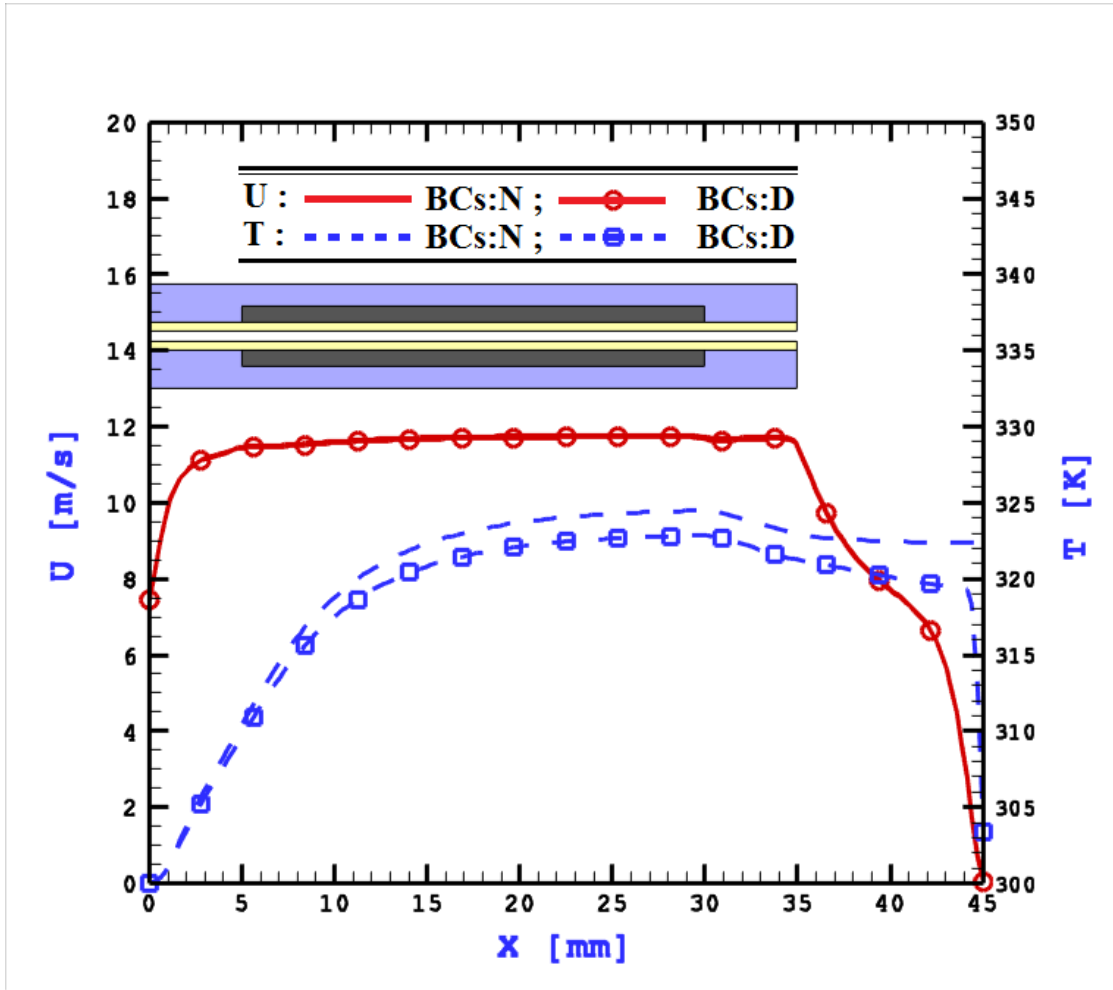


Figure 4-31. Horizontal velocity and temperature profiles along the center line of the helium DBD APPJ channel for  $d = 1$  mm,  $H/d = 10$ ,  $Re = 60$  and gas flow rate of 20 slm .

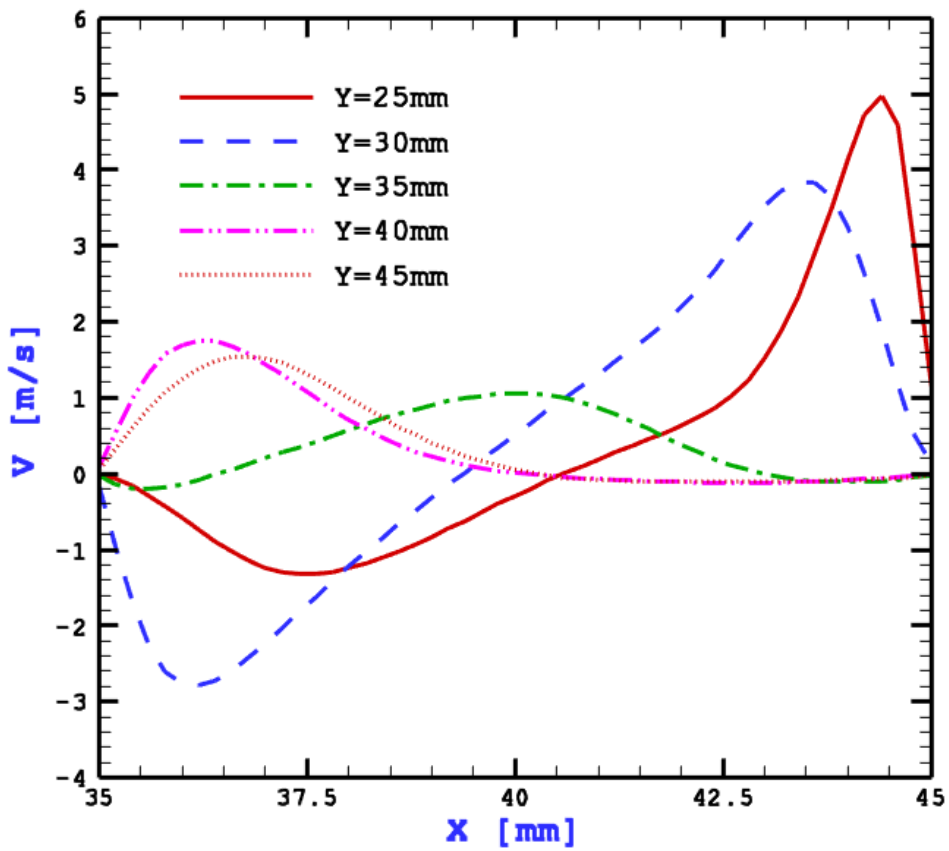


Figure 4-32. Vertical velocity profiles between helium DBD APPJ and substrate at different y positions for  $d = 1 \text{ mm}$ ,  $H/d = 10$ ,  $Re = 60$  and gas flow rate of 20 slm .

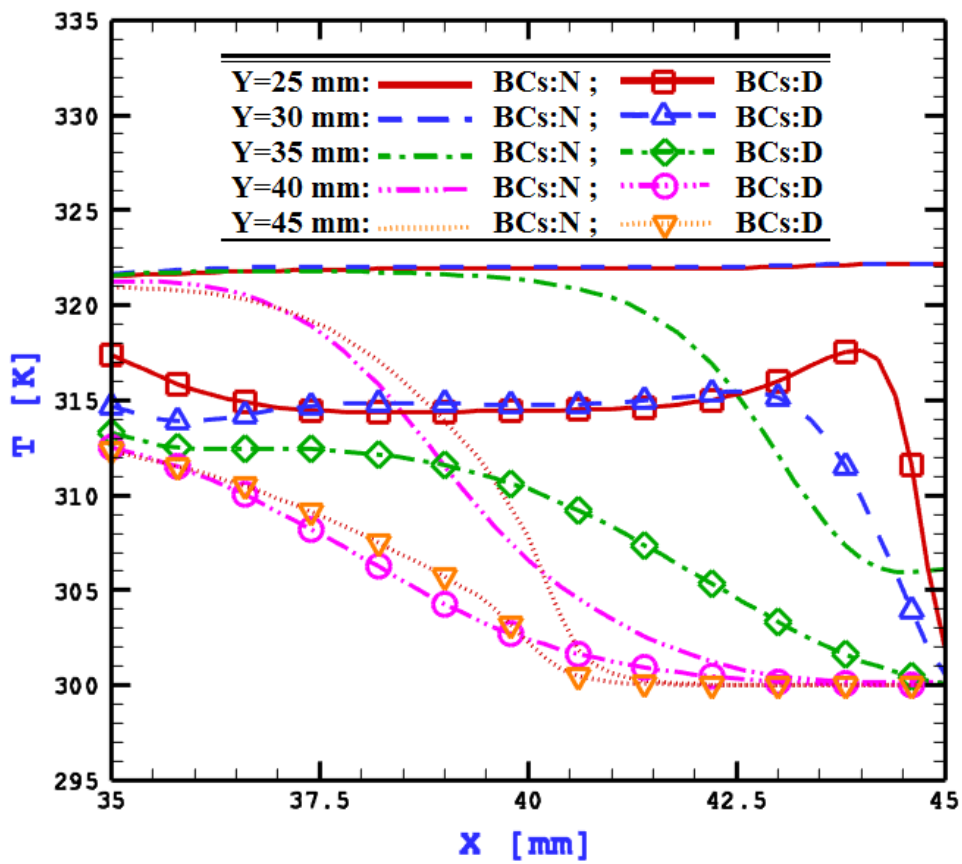


Figure 4-33. Temperature profiles between helium DBD APPJ and substrate at different y positions for  $d = 1$  mm,  $H/d = 10$ ,  $Re = 60$  and gas flow rate of 20 slm .

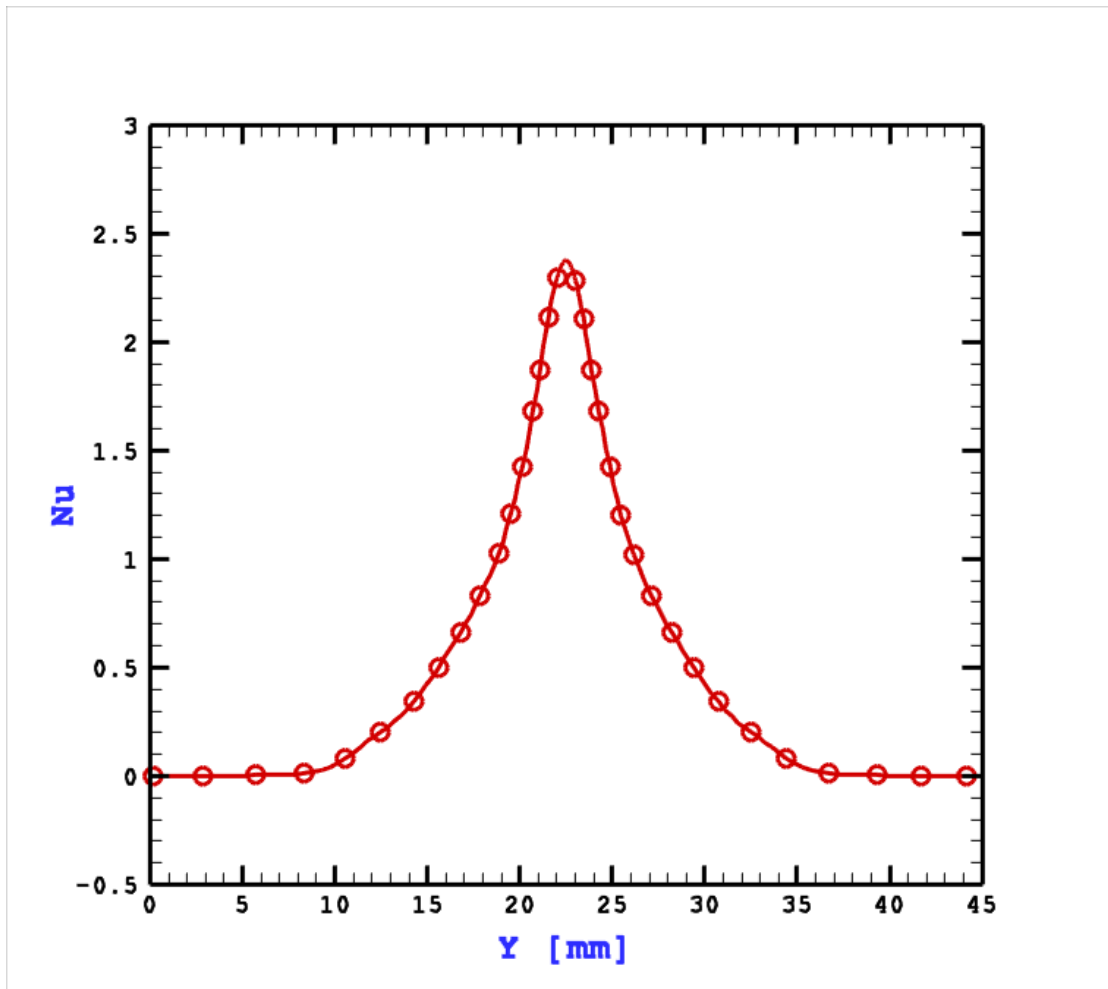


Figure 4-34. Local Nusselt number along a isothermal substrate surface for  $d = 1$  mm ,

$H/d = 10$ ,  $Re = 60$  and gas flow rate of 20 slm .

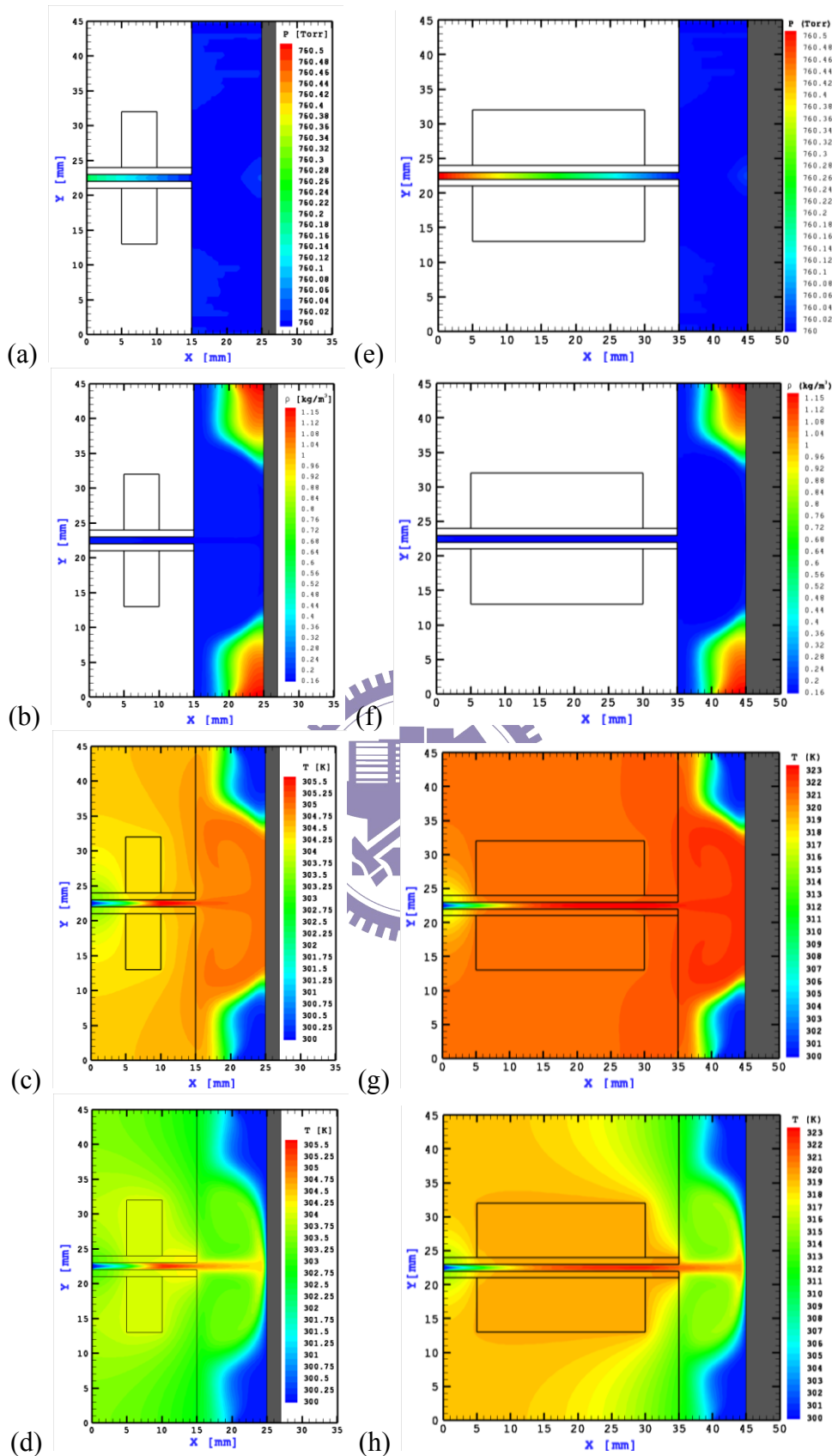


Figure 5-1. Comparison of the distributions of (a, e) pressure, (b, f) over-all density, (c, g) temperature for an adiabatic wall, and (d, h) temperature for an adiabatic wall for electrode lengths of 5 mm and 25 mm, respectively.



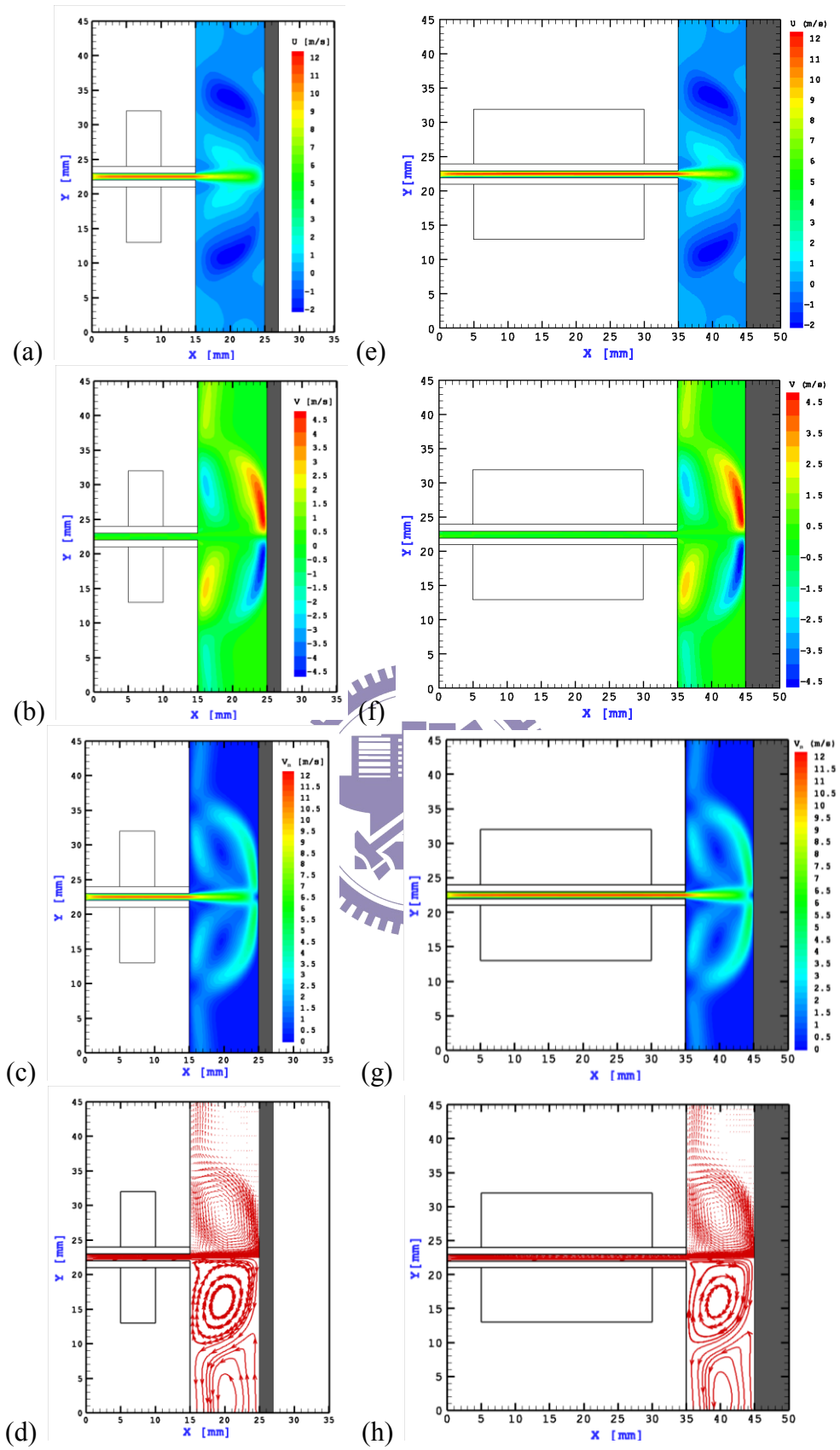


Figure 5-2. Comparison of the distributions of velocity components for electrode lengths of (a-d) 5 mm and of (e-h) 25 mm, respectively.

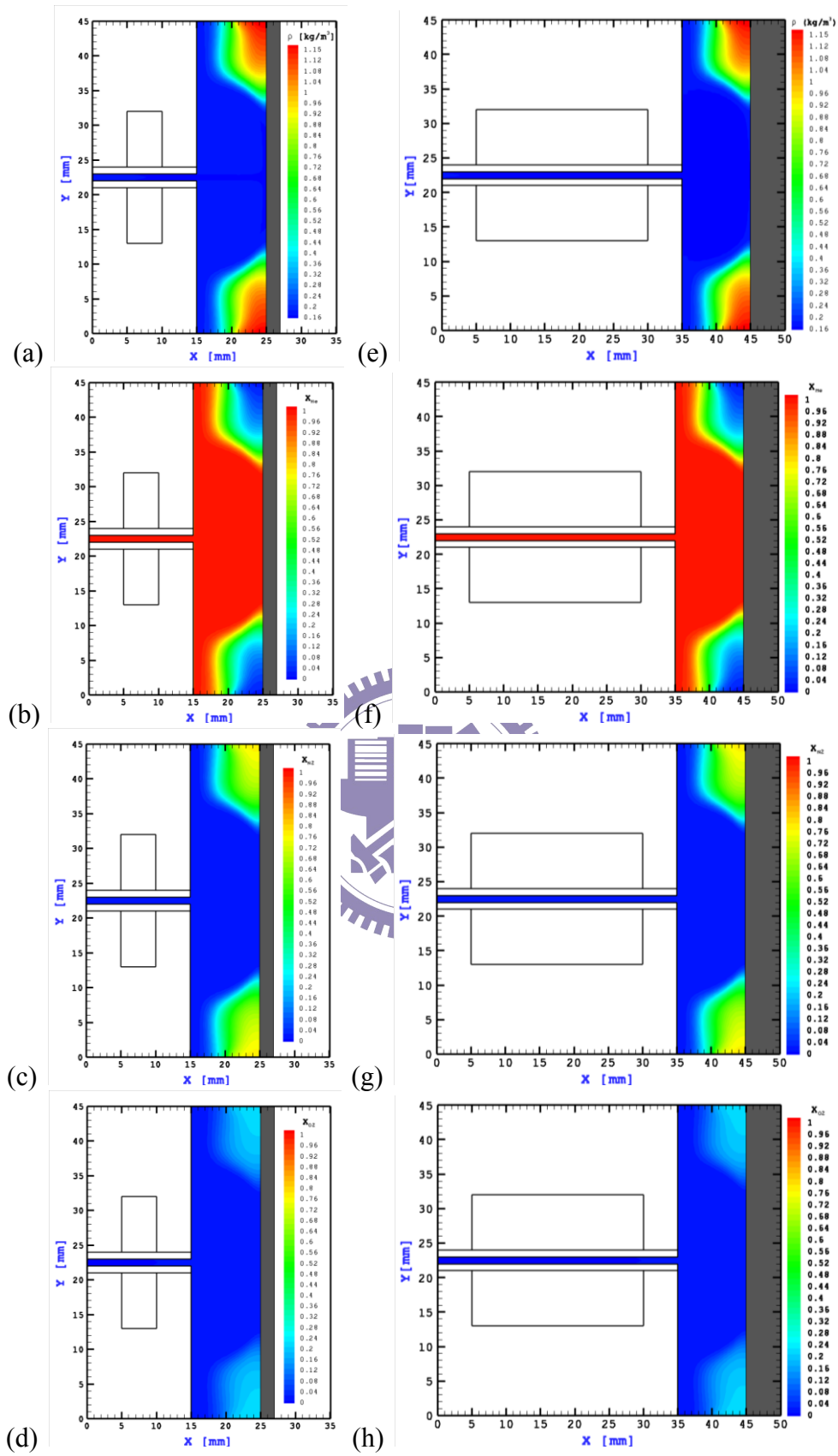


Figure 5-3. Comparison of the distributions of species mole fraction for electrode lengths of (a-d) 5 mm and of (e-h) 25 mm, respectively.

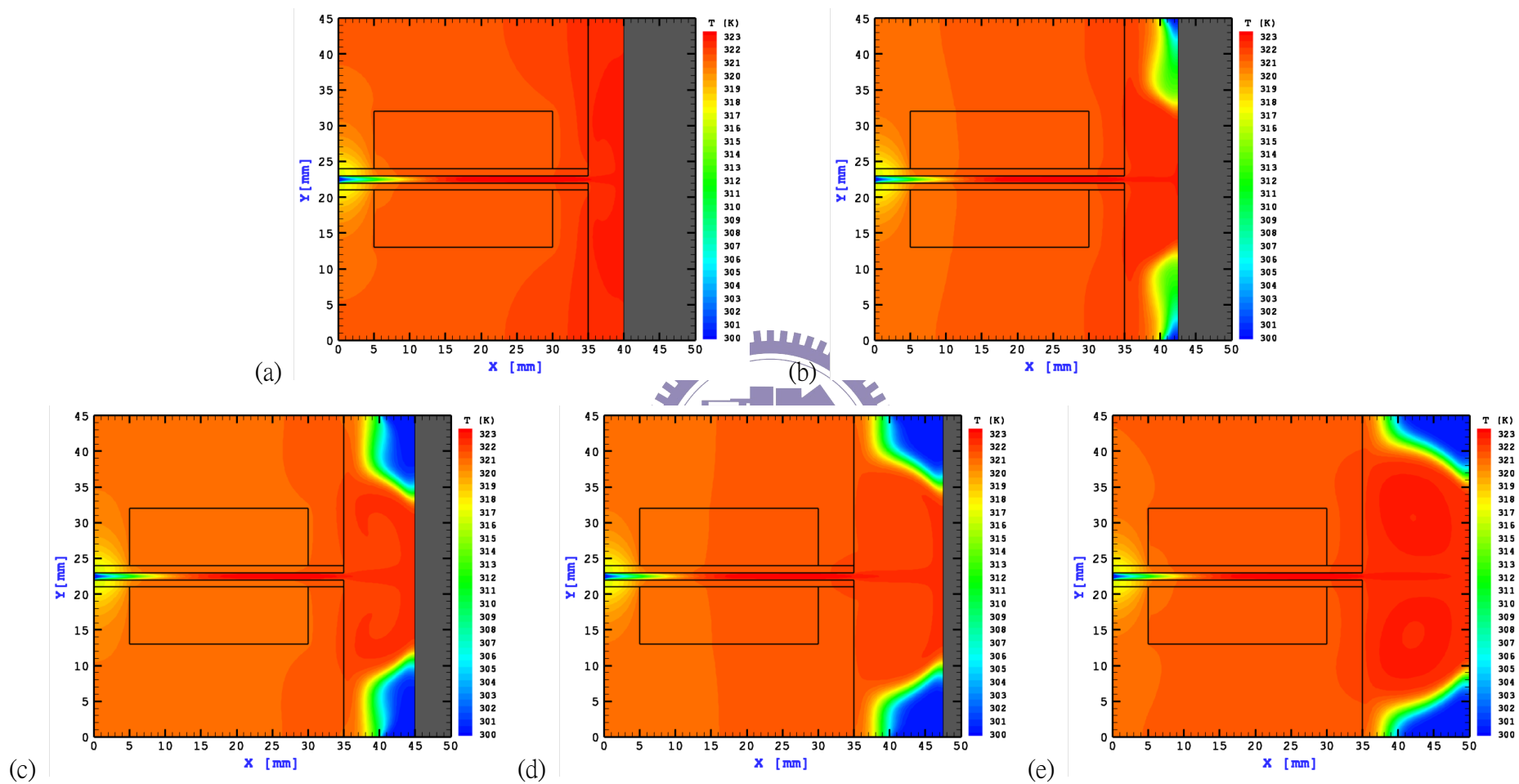


Figure 5-4. Comparison of the temperature distributions for an adiabatic substrate for  $H/d =$  (a) 5, (b) 7.5, (c) 10, (d) 12.5, (e) and 15, respectively.

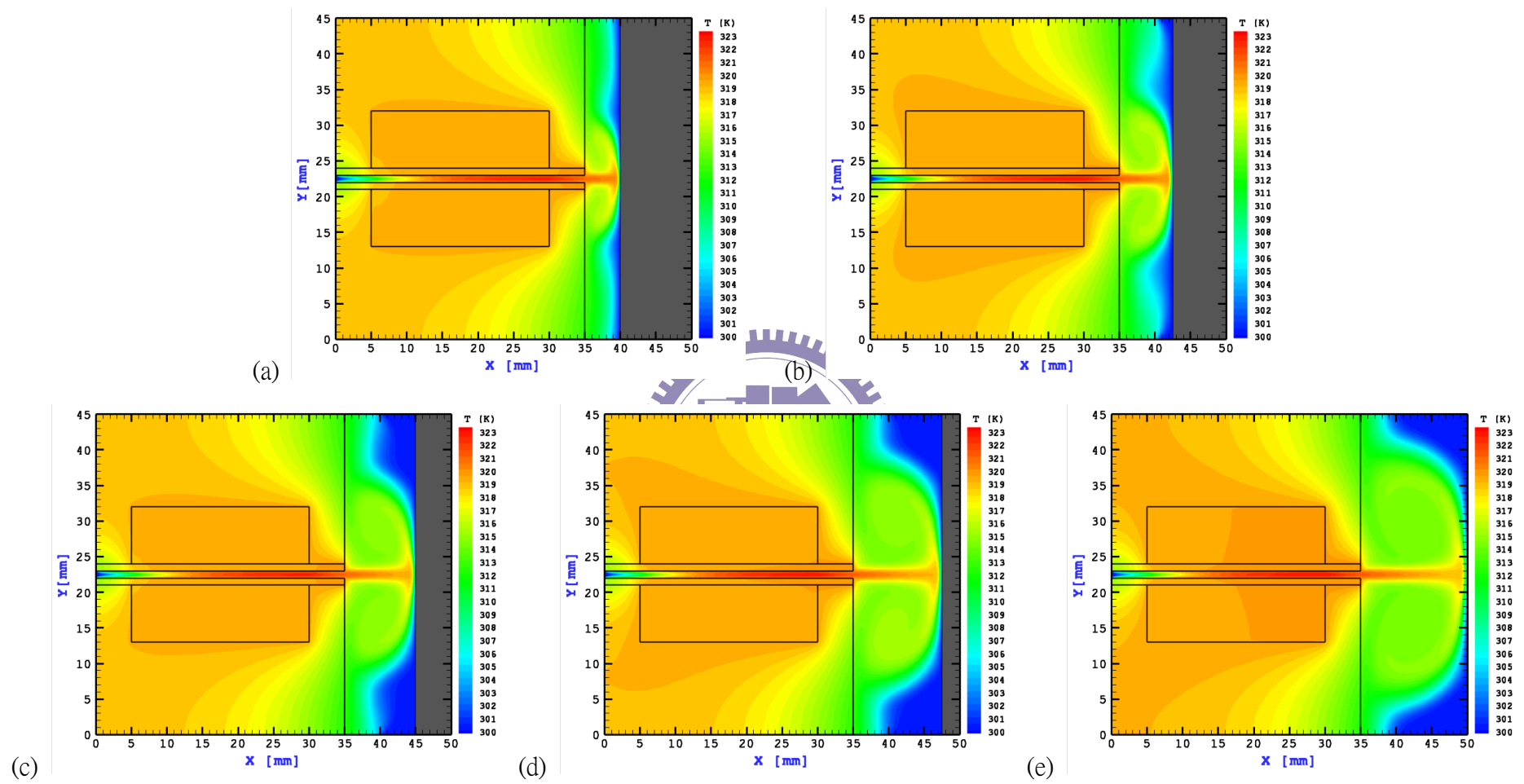


Figure 5-5. Comparison of the temperature distributions of an isothermal substrate for  $H/d =$  (a) 5, (b) 7.5, (c) 10, (d) 12.5, (e) and 15, respectively.

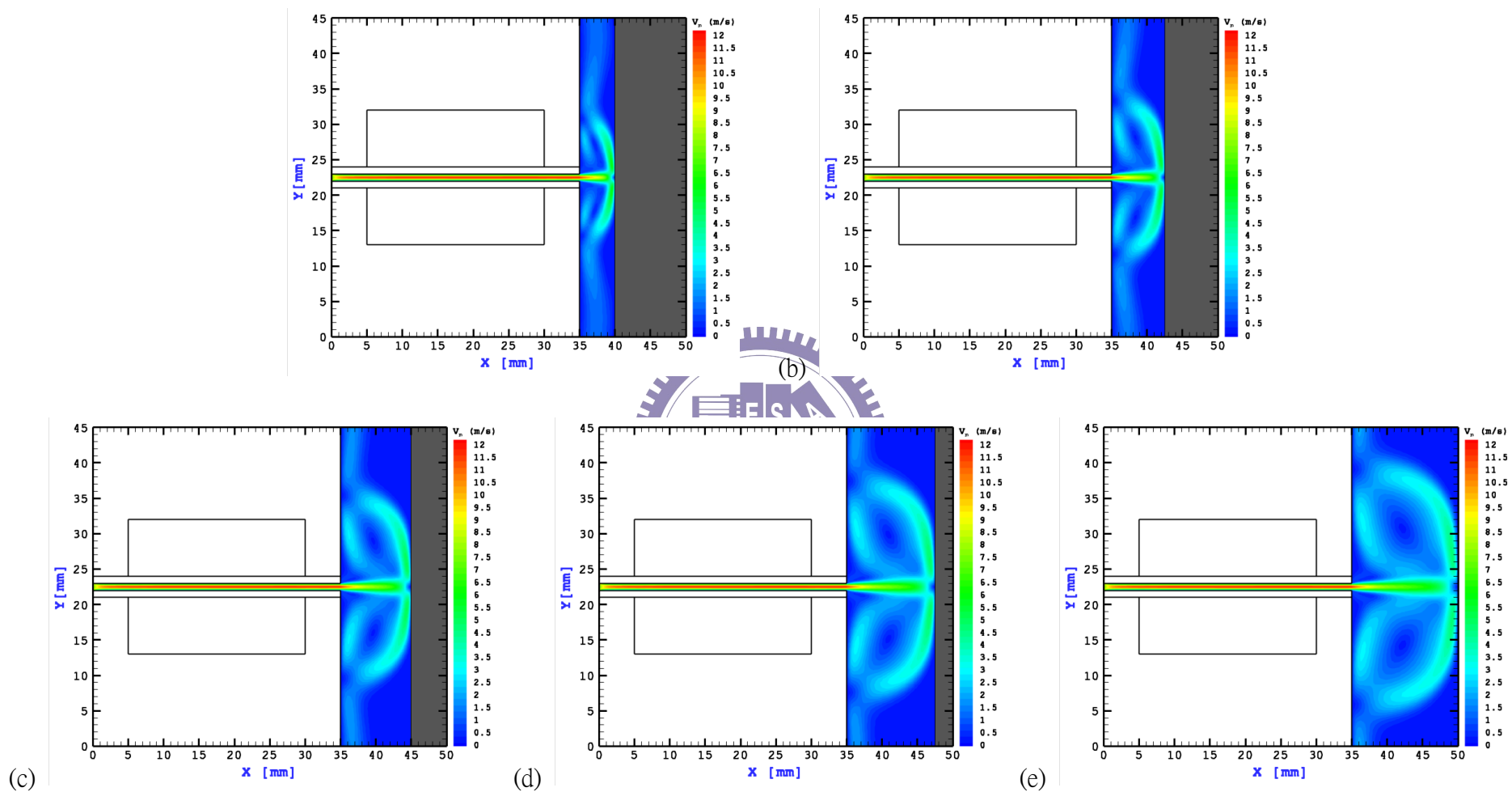


Figure 5-6. Comparison of the mean speed distributions for  $H/d =$  (a) 5, (b) 7.5, (c) 10, (d) 12.5, (e) and 15, respectively.

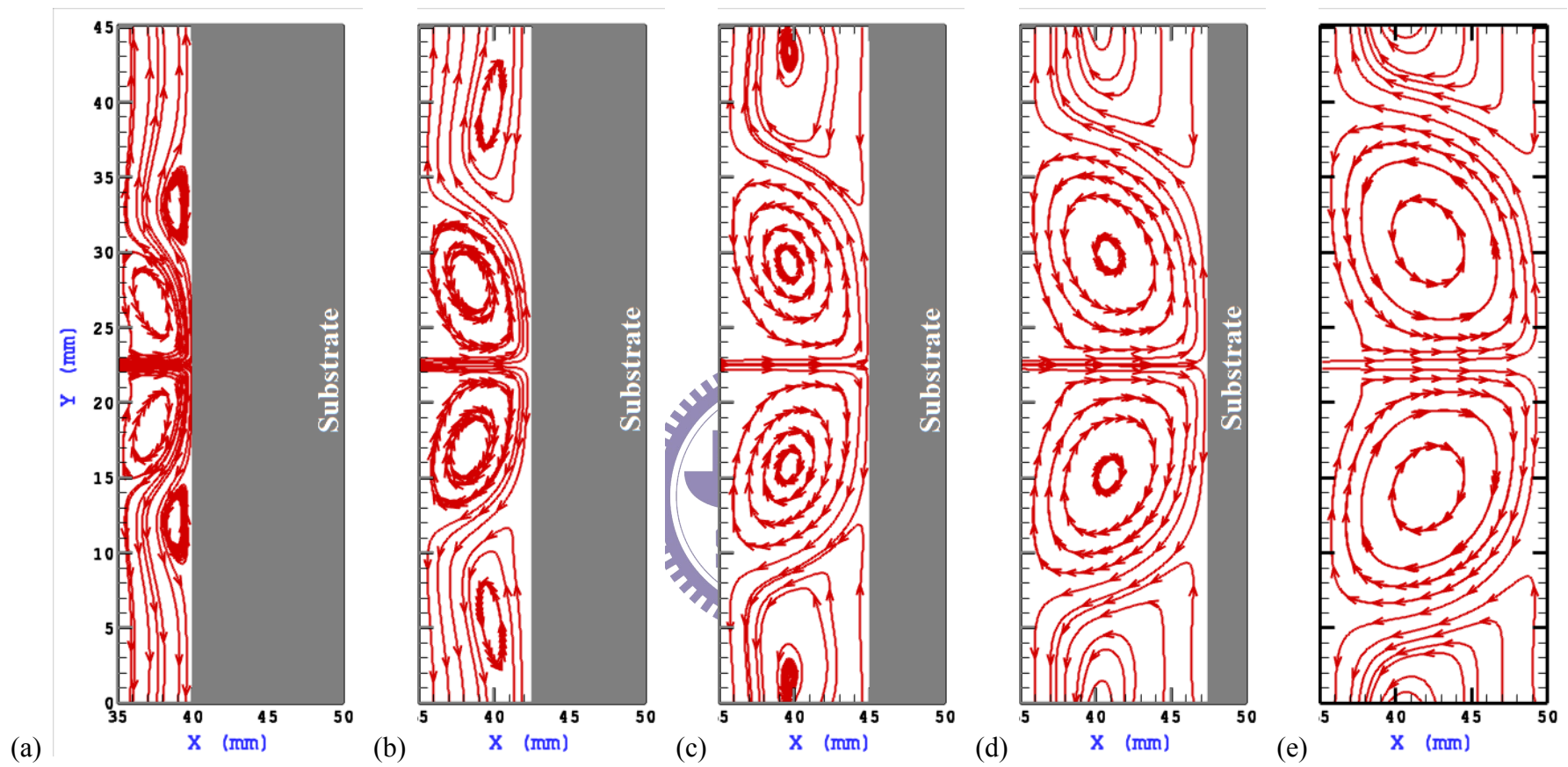


Figure 5-7. Comparison of the streamline profiles for  $H/d =$  (a) 5, (b) 7.5, (c) 10, (d) 12.5, (e) and 15, respectively.

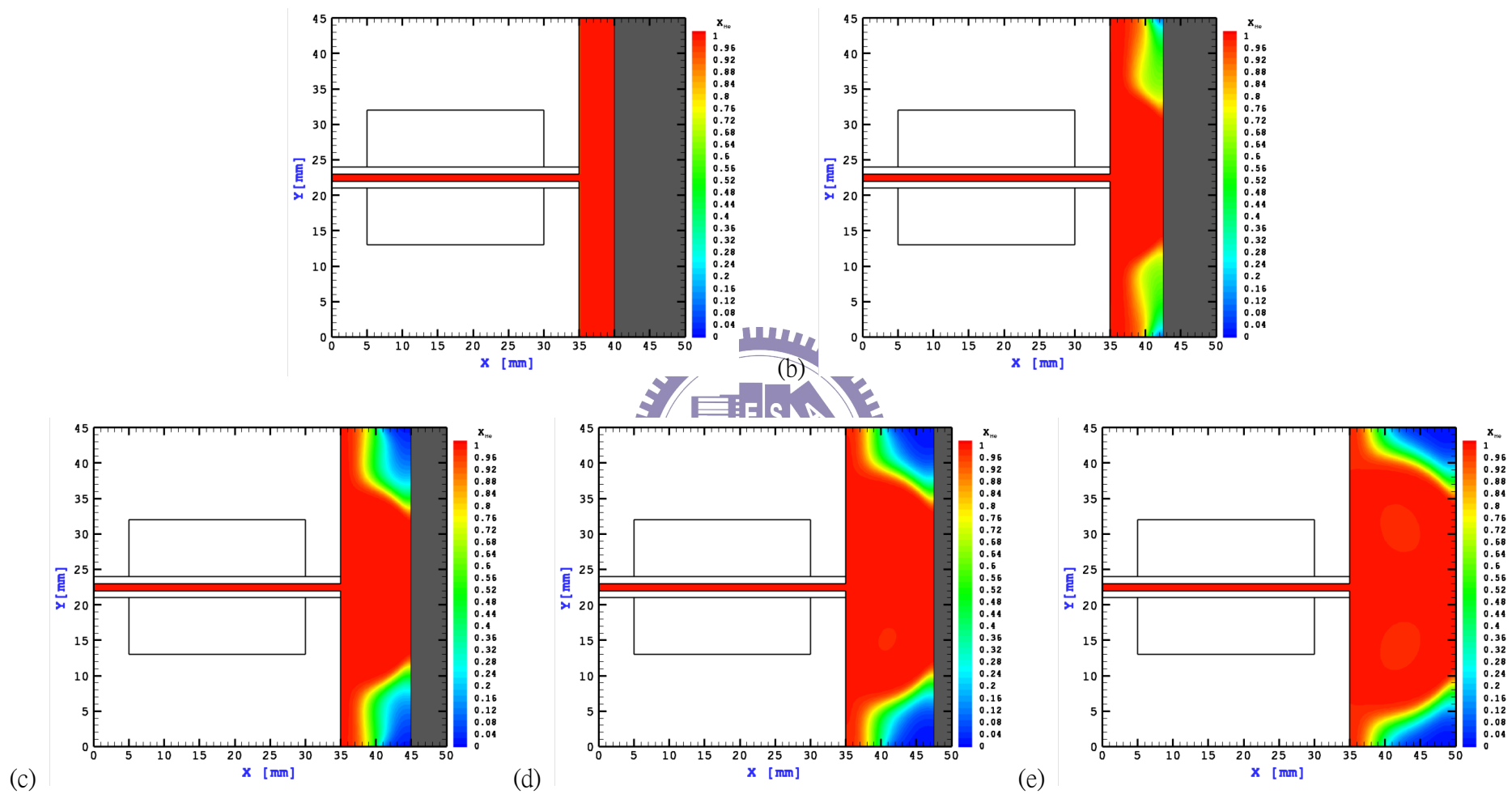


Figure 5-8. Comparison of the distributions of  $X_{He}$  for various  $H/d =$  (a) 5, (b) 7.5, (c) 10, (d) 12.5, (e) and 15, respectively.

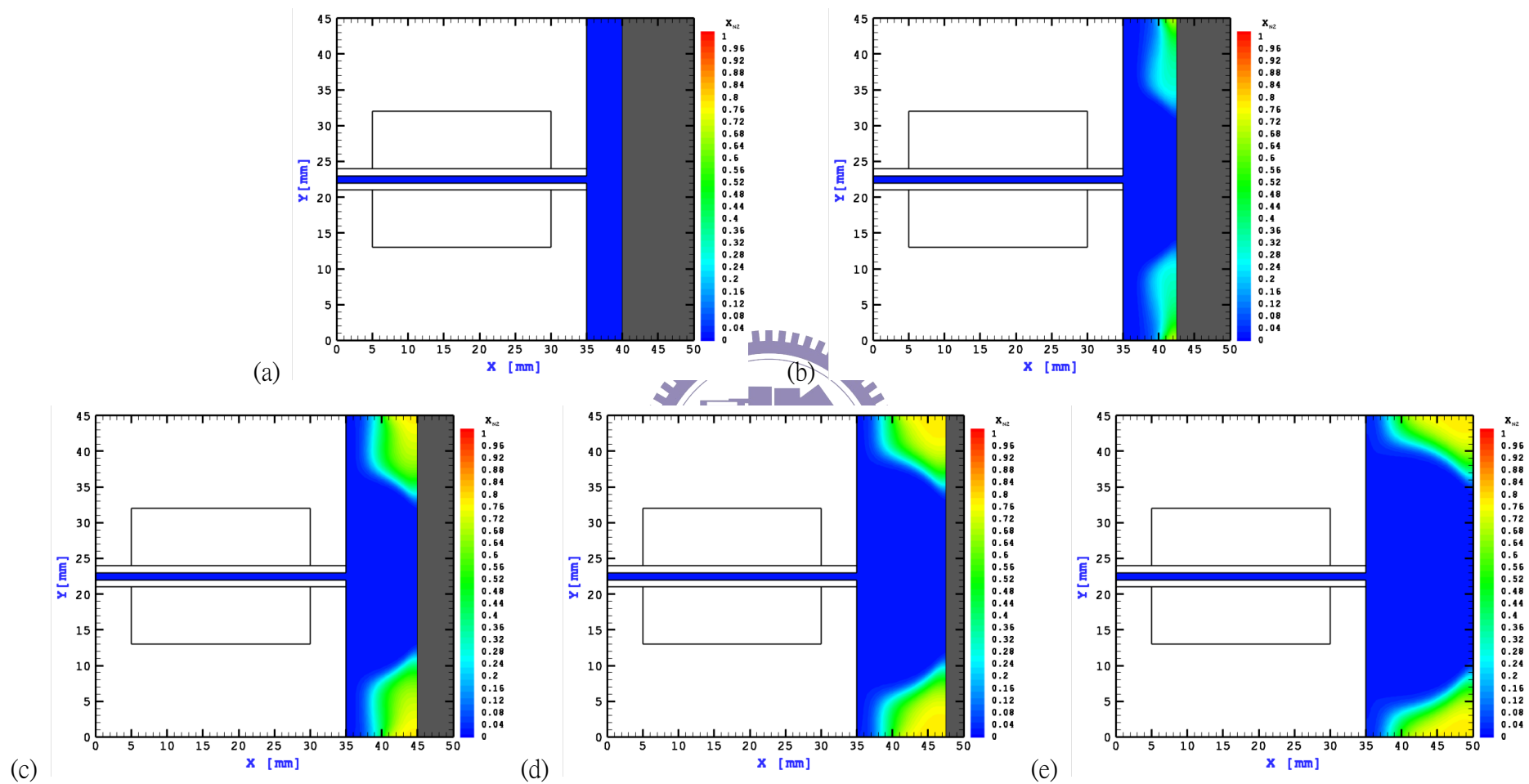


Figure 5-9. Comparison of the distributions of  $X_{N_2}$  for various  $H/d =$  (a) 5, (b) 7.5, (c) 10, (d) 12.5, (e) and 15, respectively.



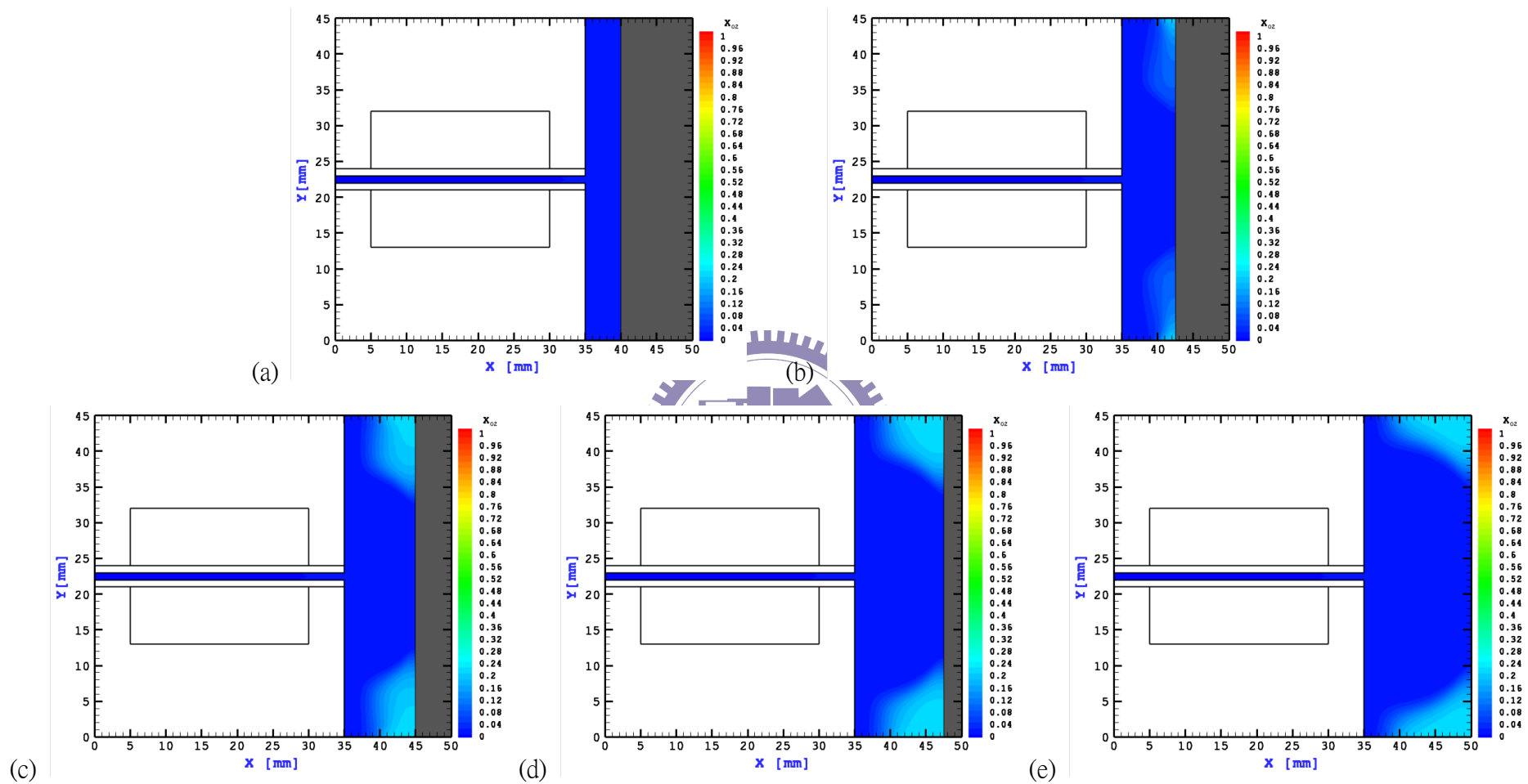


Figure 5-10. Comparison of the distributions of  $X_{O_2}$  for various  $H/d =$  (a) 5, (b) 7.5, (c) 10, (d) 12.5, (e) and 15, respectively.

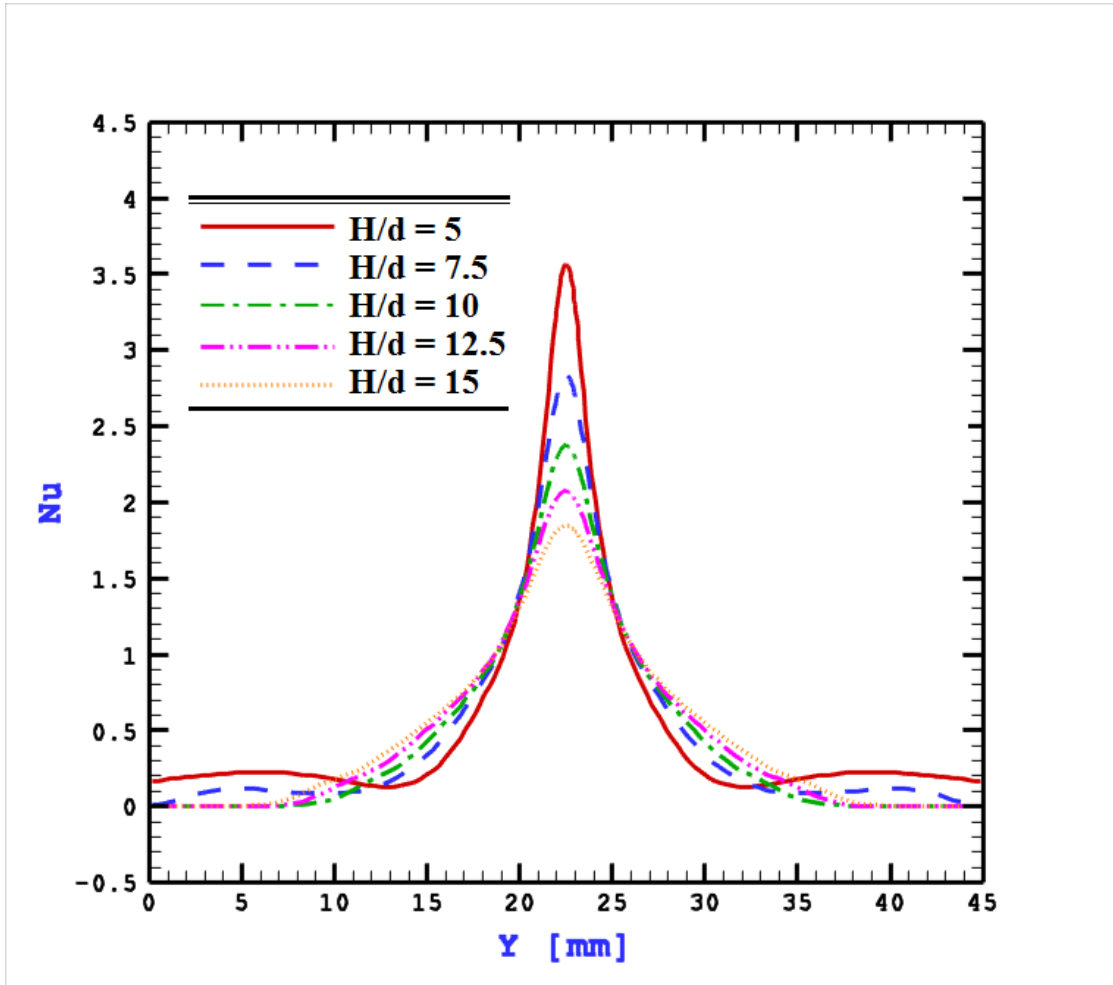


Figure 5-11. Local Nusselt number along a isothermal substrate surface for various  $H/d$ .

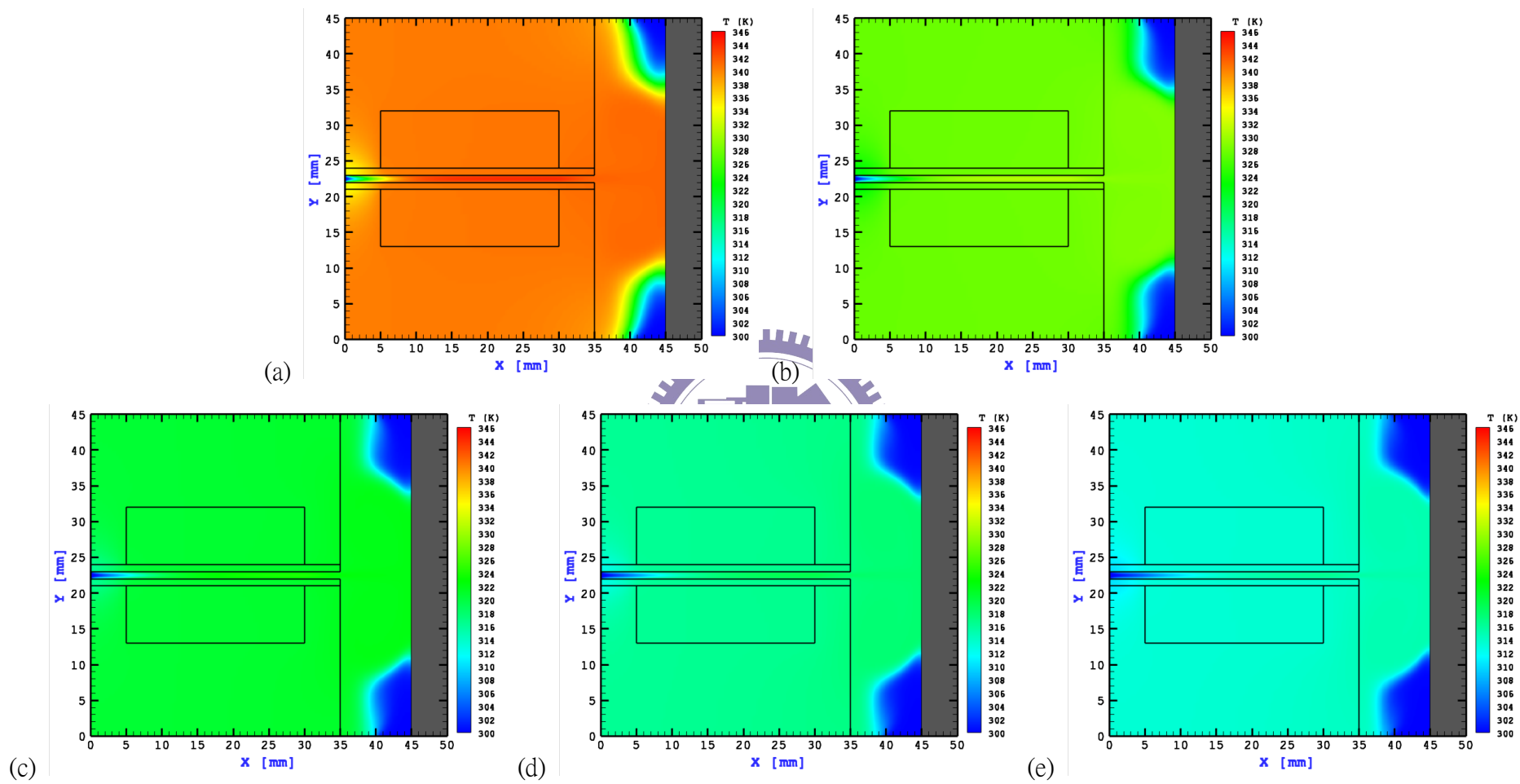


Figure 5-12. Comparison of the temperature distributions for an adiabatic substrate for various gas flow rates of (a) 10 *slm*, (b) 15 *slm*, (c) 20 *slm*, (d) 25 *slm*, (e) and 30 *slm*, respectively.

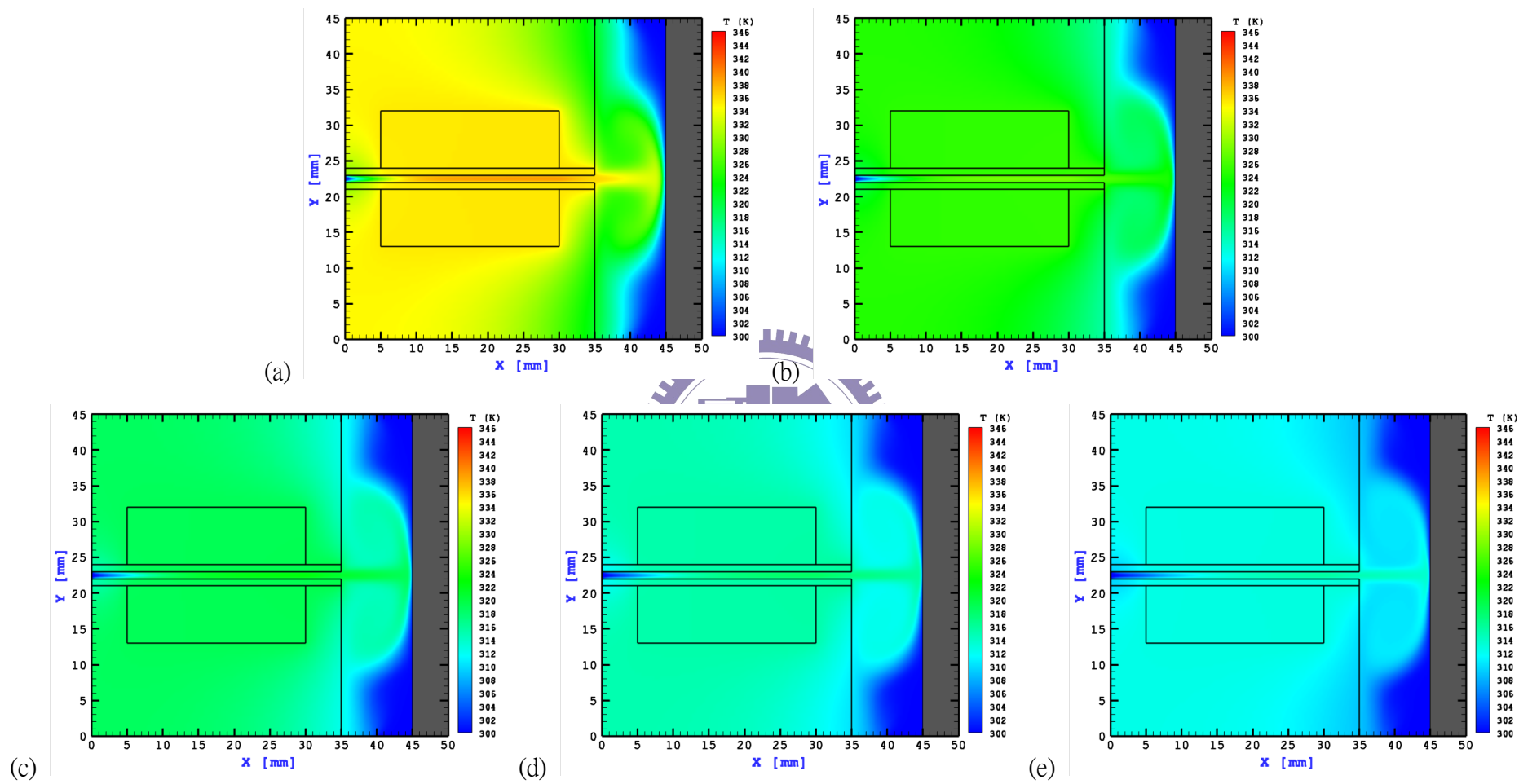


Figure 5-13. Comparison of the temperature distributions for an isothermal wall for various gas flow rates of (a) 10 *slm* , (b) 15 *slm* , (c) 20 *slm* , (d) 25 *slm* , (e) and 30 *slm* , respectively.

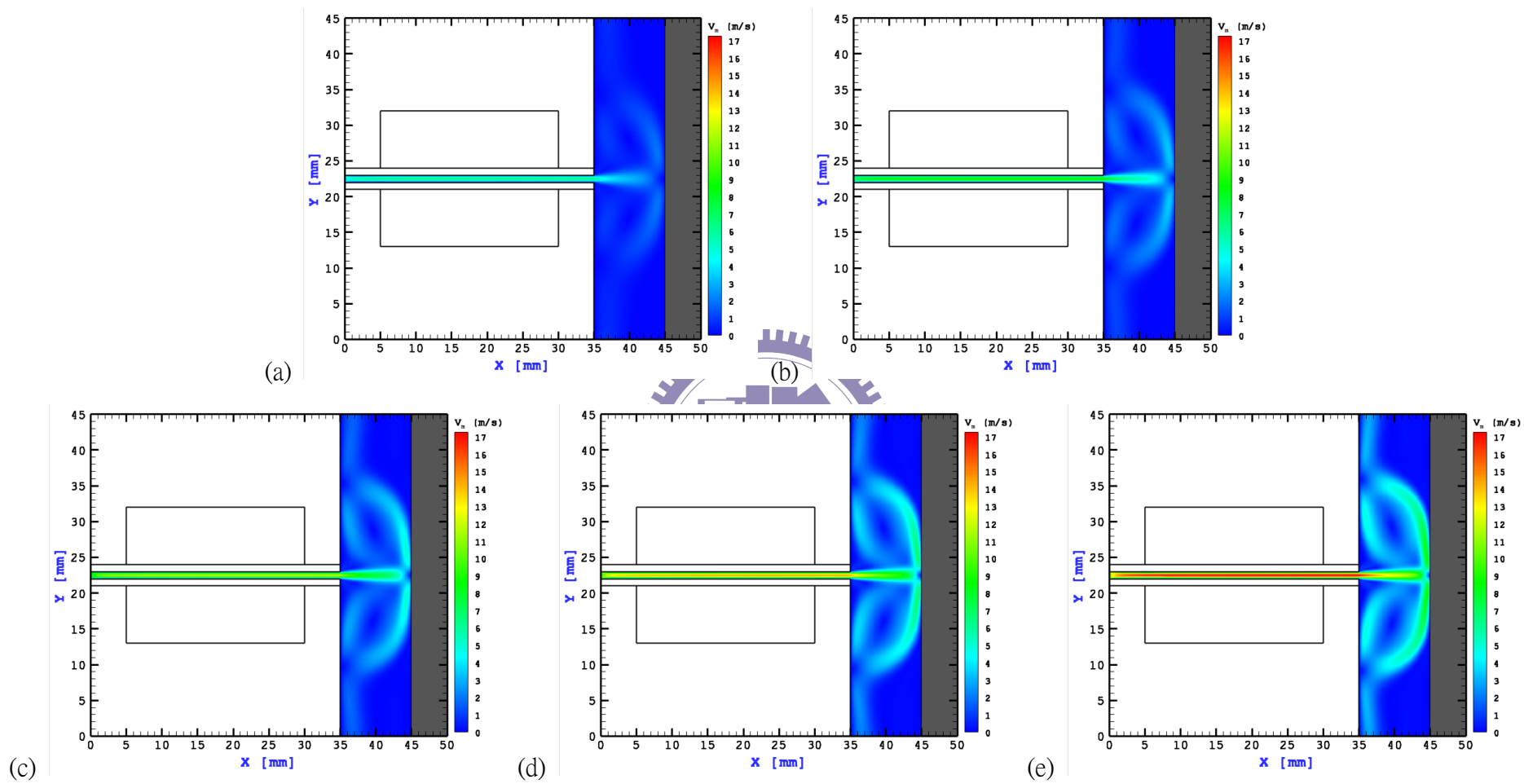


Figure 5-14. Comparison of the mean speed distributions for gas flow rates of (a) 10 *slm* , (b) 15 *slm* , (c) 20 *slm* , (d) 25 *slm* , (e) and 30 *slm* , respectively.

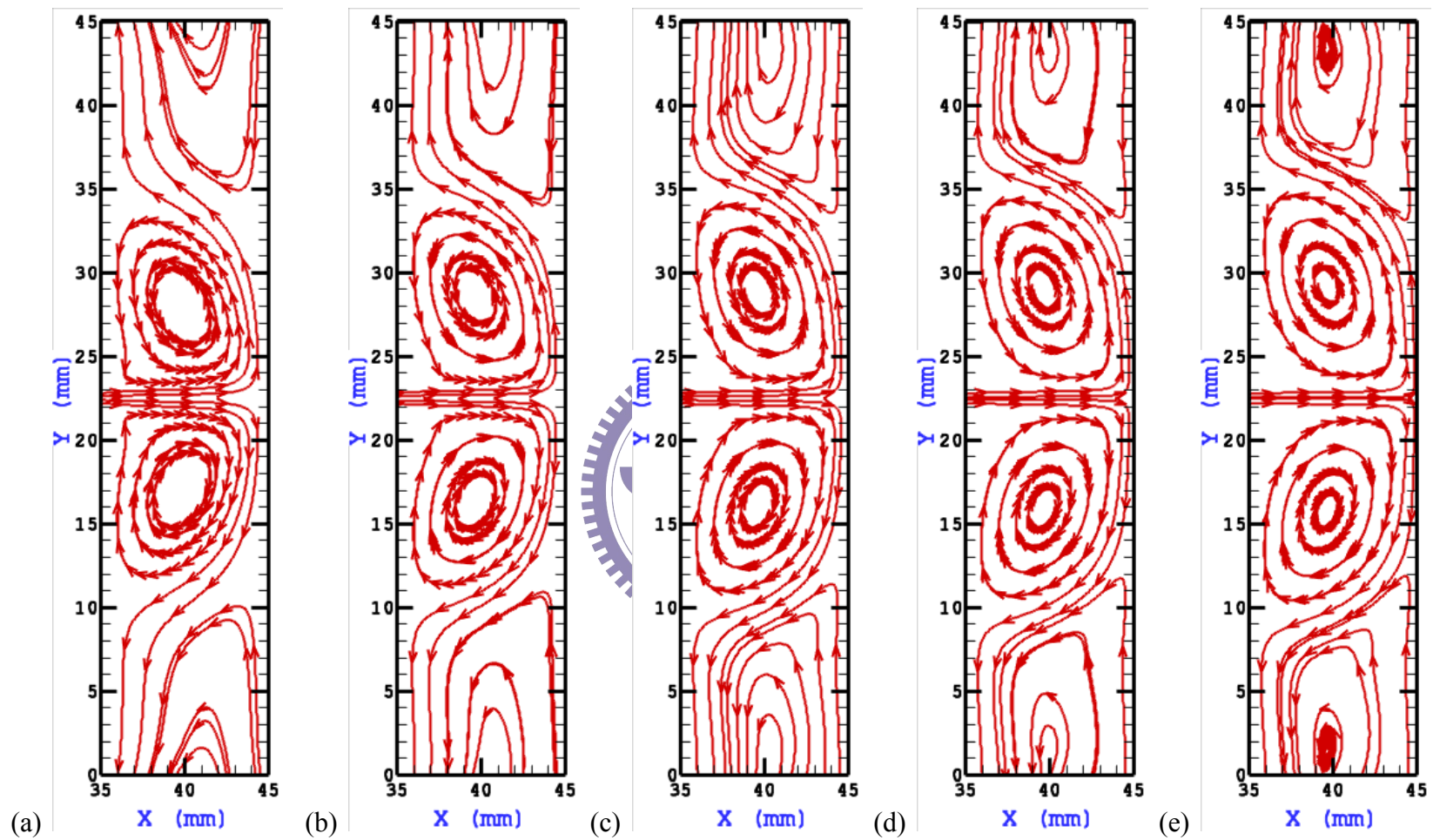


Figure 5-15. Comparison of the streamline profiles for various gas flow rates of (a) 10 *slm* , (b) 15 *slm* , (c) 20 *slm* , (d) 25 *slm* , (e) and 30 *slm* , respectively.

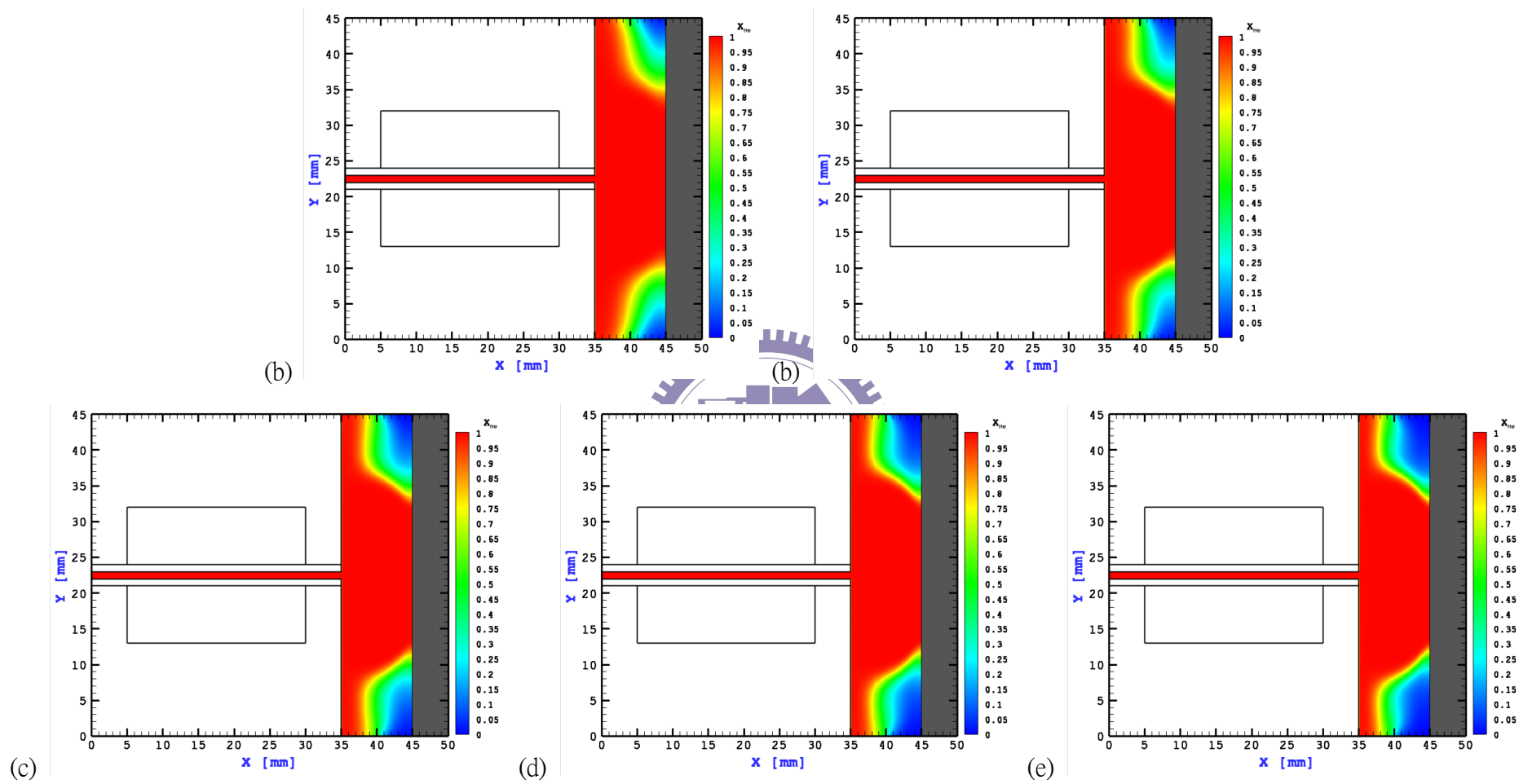


Figure 5-16. Comparison of the distributions of  $X_{He}$  for various gas flow rates of (a) 10 *slm* , (b) 15 *slm* , (c) 20 *slm* , (d) 25 *slm* , (e) and 30 *slm* , respectively.

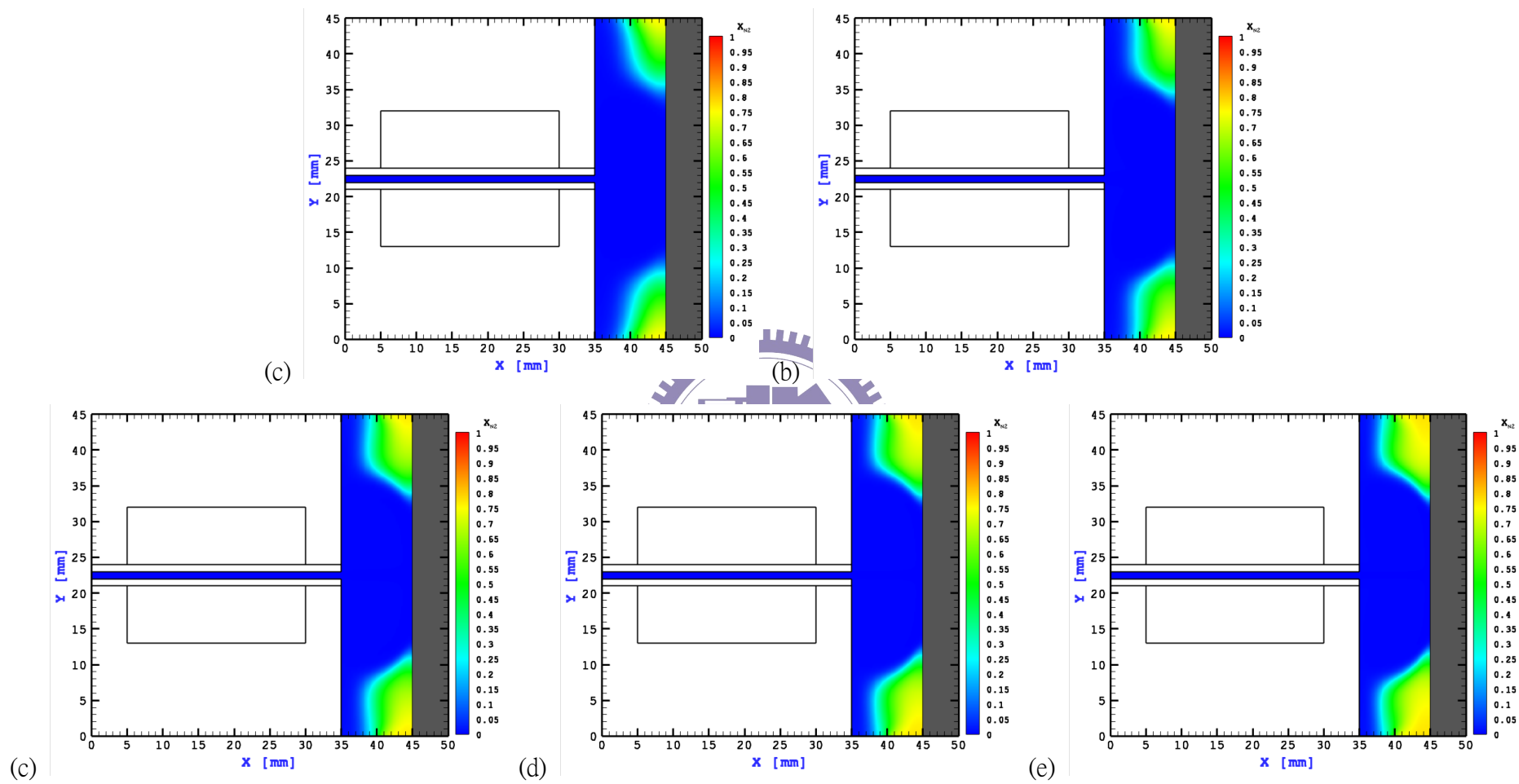


Figure 5-17. Comparison of the distributions of  $X_{N_2}$  for various gas flow rates of (a) 10 *slm*, (b) 15 *slm*, (c) 20 *slm*, (d) 25 *slm*, (e) and 30 *slm*, respectively.



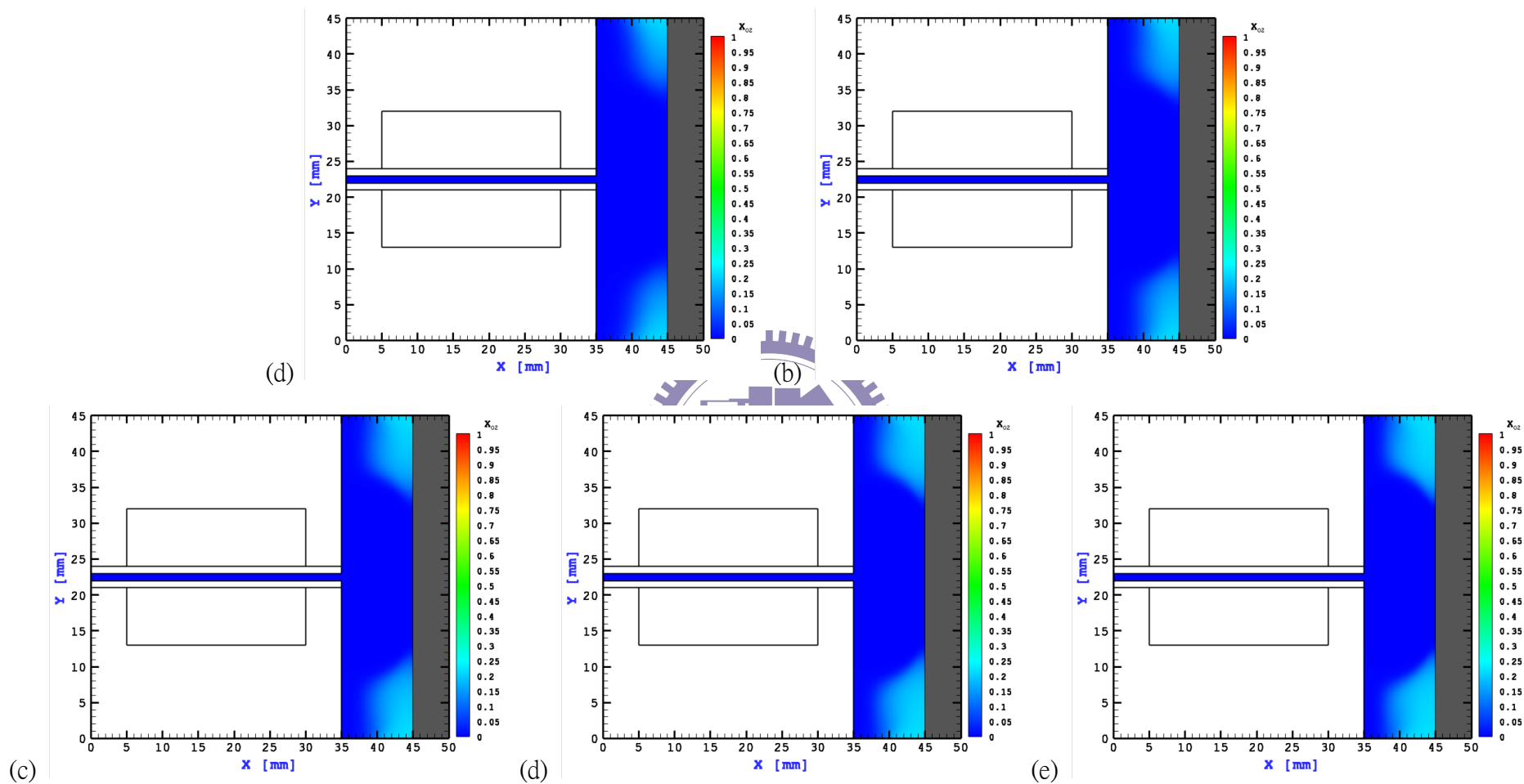


Figure 5-18. Comparison of the distributions of  $X_{O_2}$  for various gas flow rates of (a) 10 *slm*, (b) 15 *slm*, (c) 20 *slm*, (d) 25 *slm*, (e) and 30 *slm*, respectively.

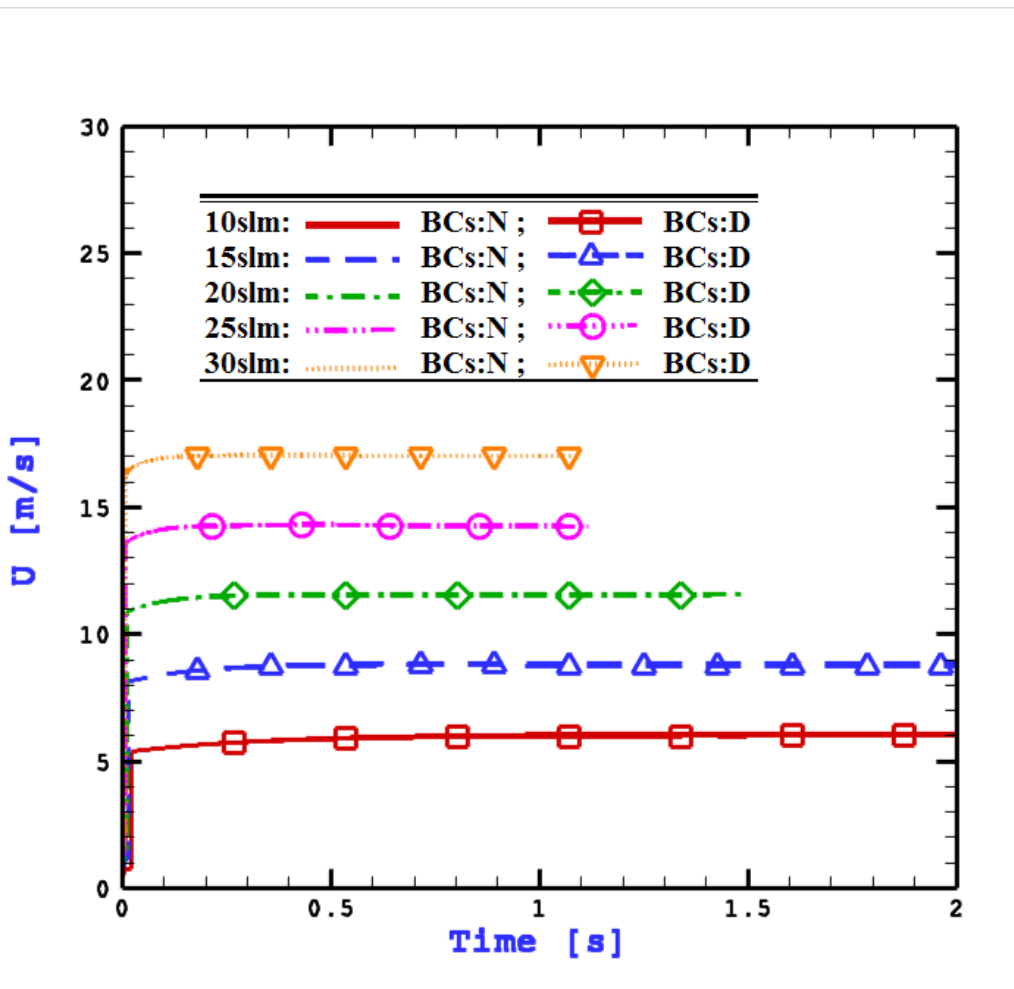


Figure 5-19. Horizontal velocity profiles at export of helium DBD APPJ as a function of times for various gas flow rates.

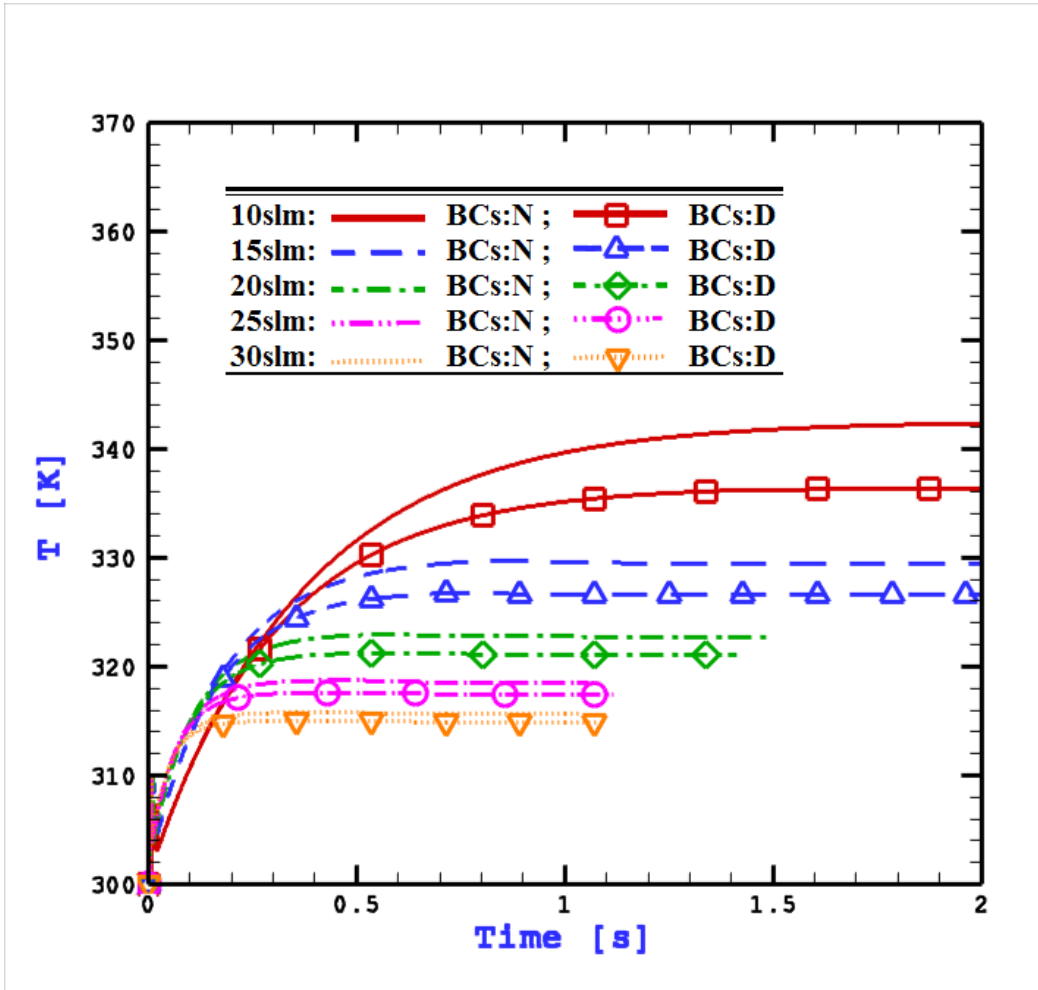


Figure 5-20. Temperature profiles at export of helium DBD APPJ as a function of times for various gas flow rates.

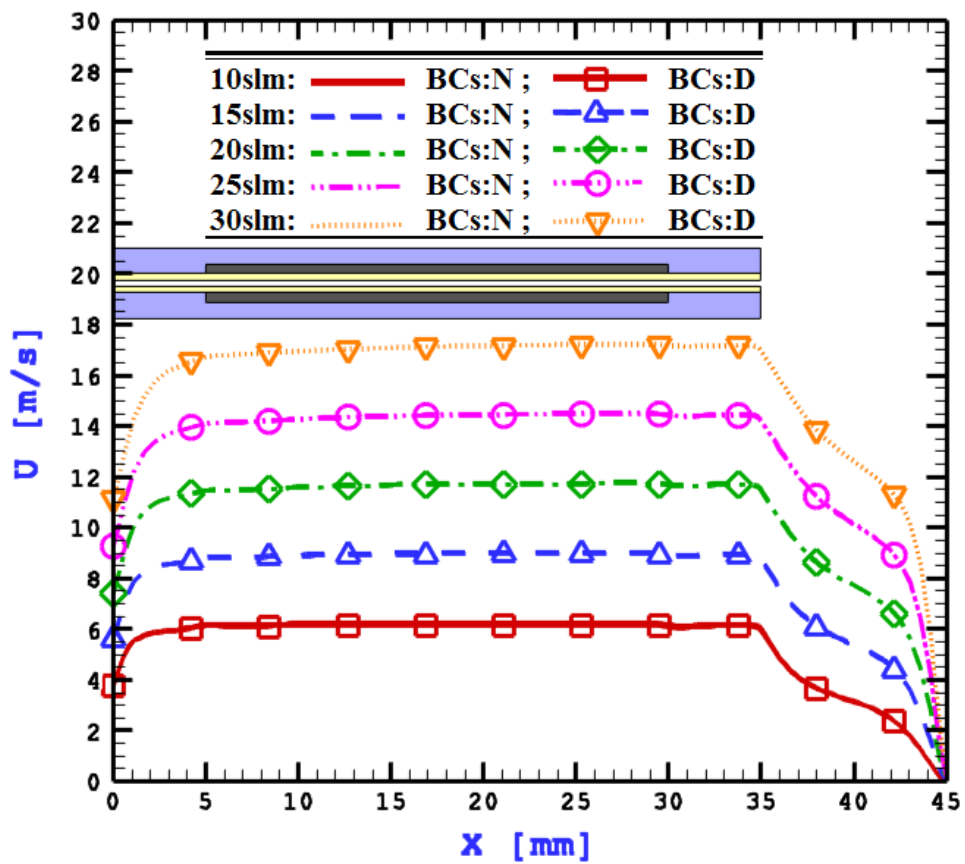


Figure 5-21. Horizontal velocity profiles along the center line of the helium DBD APPJ for various gas flow rates.

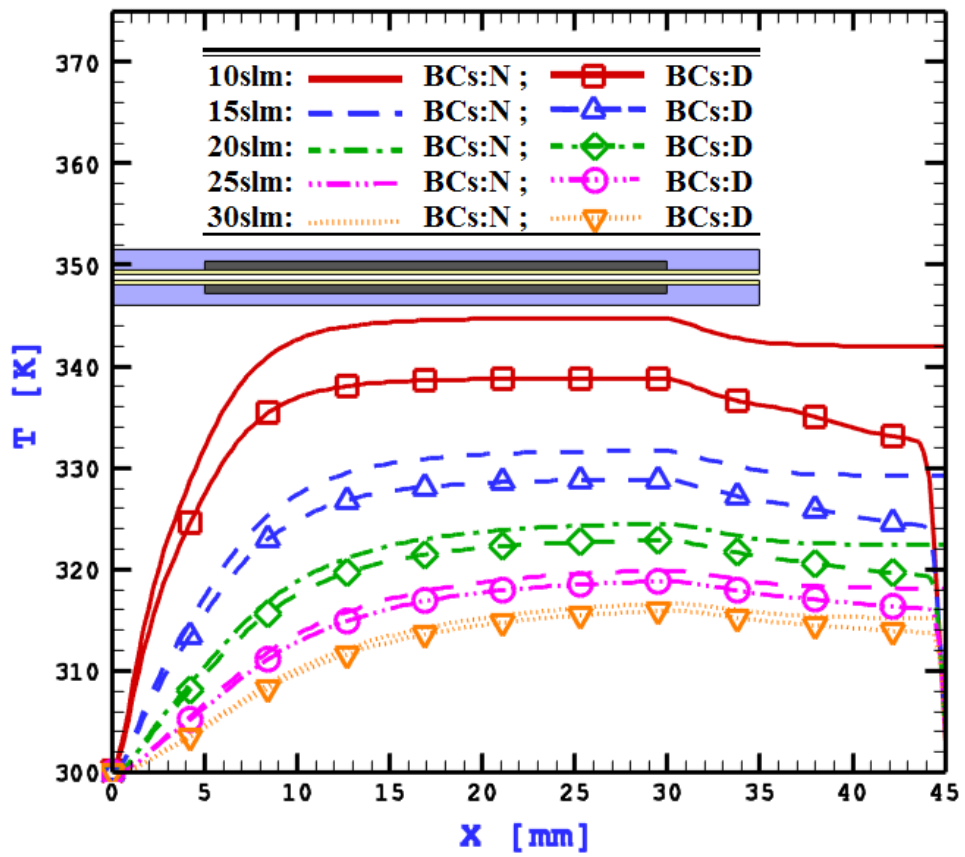


Figure 5-22. Temperature profiles along the center line of the helium DBD APPJ for various gas flow rates.

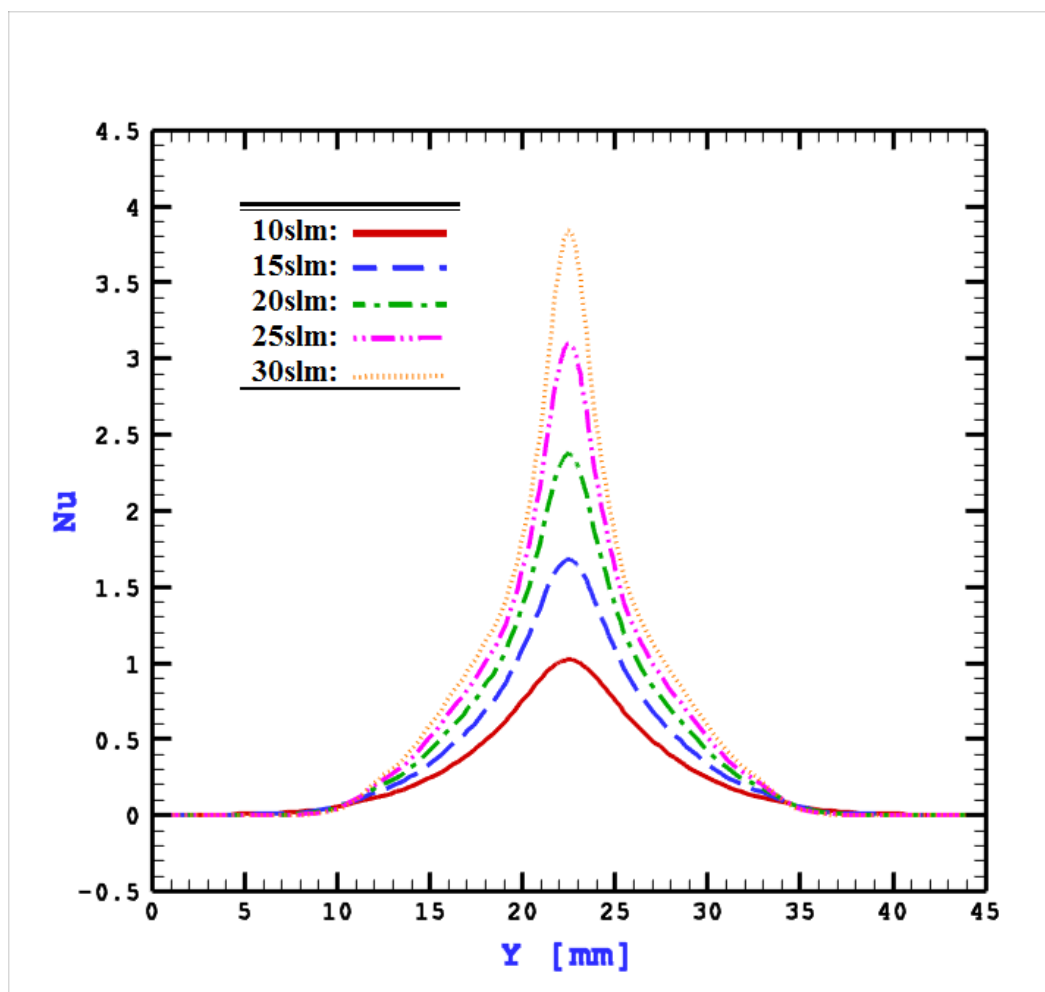


Figure 5-23. Local Nusselt number profiles along the substrate surface for various gas flow rates.

## Publication List of Meng-Hua Hu

### Journal Papers:

1. C.-T. Hung, **M.-H. Hu**, J.-S. Wu\* and F.-N. Hwang, "A New Paradigm for Solving Plasma Fluid Modeling Equations," Computer Physics Communications, Vol. 177, pp. 138-139, 2007.
2. **M.-H. Hu**, J.-S. Wu\* and Y.-S. Chen, "Development of a Parallelized 2D/2D-Axisymmetric Navier-Stokes Equation Solver for All-Speed Gas Flows," Computers & Fluids, Vol. 45, pp. 241-248, 2011.
3. K.-M. Lin, **M.-H. Hu**, C.-T. Hung and J.-S. Wu\*, "Development of a Parallel 2-D Hybrid Modeling Algorithm for Gas Flow and Discharge," Computer Physics Communications, 2012 (submitted).
4. **M.-H. Hu**, K.-M. Lin, J.-S. Wu\* and Y.-S. Chen, "Flow Simulation of a Cold Planar Atmospheric-Pressure Plasma Jet Considering Gas Heating," International Journal of Heat and Mass Transfer (preparing, 2012).

### International Conference Papers:

1. C.-T. Hung, **M.-H. Hu**, Y.-M. Chiu, J.-S. Wu and F.-N. Hwang, "Development of a Parallel 2D Fluid Modeling Code for Non-thermal Plasma Simulations," 26th International Symposium on Rarefied Gas Dynamics, July 21-25, 2008, Kyoto University, Kyoto, Japan.
2. C. T. Hung, **M. H. Hu**, Y. M. Chiu, K. M. Lin, Y. C. Wang, J. S. Wu\*, and F. N. Hwang, "Non-Thermal Plasma Simulation Using Parallel 2D Fluid Modeling

- Code,” Workshop on High Performance Simulation of Physical Systems, HSPSP’09, March 2-5 (2009), Kaohsiung, Taiwan.
3. Meng-Hua Hu, **J.-S. Wu\***, Y. -S. Chen, “Development of a Parallelized 2D/2D-Axisymmetric Navier-Stokes Solver for Conjugate Heat Transfer at All-Speed Gas Flows,” The 22<sup>nd</sup> International Conference on Parallel Computational Fluid Dynamics, Kaohsiung, Taiwan, May 17-21, 2010.
  4. J.-S. Wu\*, K.-M. Lin, **M.-H. Hu**, C.-T. Hung and Y.M. Chiu, “Progress in Developing Fluid Modeling and Gas Flow Simulation Codes for General Gas-Discharge Application,” American Vacuum Society International Plasma Workshop, Taipei, Taiwan, March 22-25, 2011.
  5. K.-M. Lin, **M.-H. Hu**, C.-T. Hung and J.-S. Wu\*, “Numerical Investigation of Atmospheric Pressure Plasma Jet Using Helium Discharge Driven a Radio-Frequency Power Source,” American Vacuum Society International Plasma Workshop, Taipei, Taiwan, March 22-25, 2011.
  6. K.-M. Lin, **M.-H. Hu**, C.-T. Hung and J.-S. Wu\*, “Development of Parallel Hybrid Simulation Tools for Modeling Atmospheric-Pressure Gas Discharges,” 8th EU-Japan Joint Symposium on Plasma Processing (JSPP2012), Nara, Japan, January 16-18, 2012.
  7. K.-M. Lin, **M.-H. Hu**, C.-T. Hung and J.-S. Wu\*, “Development of a Parallel 2-D Hybrid Gas Flow and Plasma Fluid Modeling Algorithm and Its Application in Simulating Atmospheric-Pressure Plasma Jet,” The 7<sup>th</sup> Asia-Pacific International Symposium on the Basics and Applications of Plasma Technology, Taipei, Taiwan, April 14-16, 2012.



## Domestic Conference Papers:

1. **M.-H. Hu**, J.-S. Wu\* and Y.-S. Chen, “Development of a Pressured-Based Finite Volume Compressible Flow Solver at All Speeds with Conjugate Heat Transfer,” 2010 CFD Conference Taiwan, Chungli, Taiwan, July 29-July 31, 2010.
2. A. Aliat, K.-M Lin, J.-S. Wu\*, and **M.-H. Hu**, “Numerical Investigation of an Anode Supported Intermediate Temperature Solid Oxide Button Fuel Cell by considering Feed Tubes Positioning,” 2010 CFD Conference Taiwan, Chungli, Taiwan, July 29-July 31, 2010.
3. **M.-H. Hu**, J.-S. Wu\*, Y.-S. Chen, and J.-P. Yu, “A Pressure-based All-speed Navier-Stokes Equation Solver and Its Parallel Implementation,” 18<sup>th</sup> Computational Fluid Dynamics Conference in Taiwan, Yilan, Taiwan, August 3-5, 2011

